Benchmarking indirect (n,γ) reaction rate measurements for s-process nucleosynthesis in the Re/Os region.

A study of $^{187-188}$*Re*

Marianne M. Bjørøen

Thesis submitted for the degree of
Master in Nuclear Physics
60 credits

Department of Physics
Faculty of mathematics and natural sciences

UNIVERSITY OF OSLO

Spring of 2021

Benchmarking indirect (n,γ) reaction rate measurements for s-process nucleosynthesis in the Re/Os region.

A study of $^{187-188}Re$

Marianne M. Bjørøen

Benchmarking indirect (n,γ) reaction rate measurements for s-process nucleosynthesis in the Re/Os region.

http://www.duo.uio.no/

Printed: Reprosentralen, University of Oslo

Abstract

This work provides measurements of the γSF and NLD of both ^{188}Re and ^{187}Re, which will enable the first experimental constraints on the ^{186}Re(n,γ) cross sections to better understand the s-process branching point of ^{186}W. This will also provide insight on resonances in the γSF.

Data for both isotopes were extracted from a single experiment done at the Oslo Cyclotron Laboratory in 2016, with a 30 MeV α-beam with SiRi for particle detection and CACTUS for γ-detection. The data was then analysed using the Oslo method.

Neither γSF showed signs of a low energy enhancement above 1 MeV, or a strong scissors resonance. A pygmy resonance could not be concluded from this work alone, but there are signs of additional strength above 4 MeV when comparing to previous measurements above S_n.

Acknowledgements

I want to thank everyone who has been supporting me through this work.

Thank you to my supervisor Ann-Cecilie for showing me great patience and support through this work. Your guidance has been essential and you have taugt me so much about everything both nuclear-physics and research wise. Your enthusiasm is contagious, though I am sometimes surprised by the hours of they day you answer my emails. Thank you my co-supervisor, Gry, for helping me whenever I have asked, even if it's on a seemingly random Saturday.

The nuclear physics group has truly been a wonderful group of colleagues, where there is always someone to ask for help. I would also like to thank everyone involved with experiments at the Oslo Cyclotron Laboratory, especially the engineers and everyone who attended shifts, for making experiments like these possible.

Furthermore, I would also like to extend my gratitude to the advisers at the physics department, for doing great work for student wellfare. This thesis would not have excisted without you, Grete. When all my subjects are a mess and I feel a little defeated, I know where to go.

Lastly, I would like to thank everyone who has made my time as a student a lot of fun. Everyone from my DnD-group, Fysikkforeningen, Lillefy, RF and strikkelunsj. I love you all.

Thank you, Alocias, for always believing in me, even when I have the worst of days. I look forward to painting our new apartment.

Contents

Chapter 1

Introduction

It's only physics if it's from the Physique region of France. Otherwise it's just sparkling math.

Unknown, Twitter.

1.1 Discovering our place in the cosmos

It was once believed that our universe was something unchanging and static that had always been. Even the idea of there being a universe as we know it today, was at one point new and unimaginable. From the old Mesopotamian societies beliefs in a vast, primordial sea, to the Egyptian sun god, daily pushing back the darkness of the abyss, and the Greek belief in Gaia herself, mother earth, arising from chaos, it is evident that humans always have been curious of our origin.

However, to find a more scientific approach, we must wander to ancient Greece. Amidst the first proposals of heliosentricity by Aristarchus of Samos[1], Archimedes estimated the size of cosmos to be the equivalent of about two light years in the 3rd century BC when he tried to estimate an upper bound of how many grains of sand that could possibly fit in the cosmos[2].

As early as the 12th century, islamic astronomers discussed the possibility of there being "thousands of thousands of worlds", and in the 13th century, another Persian scholar and the father of trigonometry, Nasīr al-Dīn al-Tūsī provides the first empirical evidence that the earth rotates around its axis.

In 1543, Copernicus published his heliocentric model, where Thomas Digge later modified this Copernican model by adding an unbound and star-filled space. It was not until 1584 Giordano Bruno finally proposed a universe in which our solar system is not the center. He filled the night sky with stars that were just like our sun, with their own planets that might foster life on their own. This, together with the belief that the cosmos was infinite, implied there was no centre.

This was not the leading view, however, and there was other problems with this model. If the universe was infinite with an infinite amount of stars, why is the night sky dark[3]? This would mean that the universe was finite, though if it was, Newton predicted it would collapse under the gravity he himself tried to explain. It was not until the 20th century and the rise of modern cosmology we began to find answers.

Einstein first modelled the universe from his newly discovered general relativity, and though he assumed it to be static, he added something remarkable to counter the collapsing gravity. A

[1] This idea of heliosentricity was promptly rejected by other contemporaries such as Ptolemy and Aristotle, and the seemingly lacking parallaxe of the stars was a significant problem as they severely underestimated how far away the stars really were.

[2] Published in his essay "The Sand Reckoner".

[3] This is also called Olbers' paradox. As it turns out, since the speed of light is finite and absolute, the universe is just not old enough for all the light to reach us.

cosmological constant, which he later called "his biggest blunder", but today is theorised to be what we call dark energy, which still, a hundred years later is one of the biggest mysteries in cosmology.

For the next discovery, Vesto Slipher and Edwin Hubble was looking at the spectra of other galaxies, and noticed an almost universal trend. The further away the galaxy, the more it was redshifted and therefore, the faster it moved away from us. Everything seemed to expand from one another and everything moved away from everything else as if everywhere was stretching out in an accelerated speed. This was proof of a universal expansion, and thus a beginning where everything and everywhere was closer than today, forming the idea of a big bang, or, as it has also been nicknamed, "The everywhere stretch".

Another observation fundamental to the evidence of this everywhere stretch, and thus the universe having a beginning, is the cosmic microwave background, denoted CMB. From thermodynamics, we know that if the universe used to be a lot smaller, it would also need to be a lot hotter and denser. This would be to the point of matter itself not sticking together, but boiling around in a primordial soup. It was so dense that, in fact, light could not travel freely, but would constantly be bounced around, and thus, the universe was opaque. When it then cooled down to the point of particles combining, the universe became see-through and all the light recently bouncing off in random directions could now travel freely. This light has travelled ever since, and as the universe has expanded it has cooled down this light.

In New Jersey in 1964, scientists were working on a highly sensitive horn antenna designed to detect radio waves bouncing of satellites, but there was a strange background signal they were not able to get rid of. They tried observing at different times of day, pointing the antenna at different parts of the sky, and even removed some pigeons nesting in the horn, but the signal persisted. This, as it turned out, was the massively redshifted signal of 3.5 kelvin from the recombination at our universes infancy.

Thus, it is widely accepted that our universe is not, in fact, static, but began a long time ago from a subatomic, primordial soup which recombined to hydrogen and helium.

1.2 Nuclear astrophysics - the origin of elements

Since our universe, in fact had a beginning, and the initial composition of our universe was nothing but hydrogen and some helium, everything else in it must come from somewhere. As our universe was young, even after the cooling and recombining of particles, there were no heavy elements. The rest of the elements must have been produced somewhere, as we live in a universe containing carbon, iron and gold. The very foundation of our modern ideas of where the elements came from stems from two simultaneous papers independently discovered and published in 1957. One is the paper often called B2FH by Margaret Burbidge, Geoffrey Burbidge, William A. Fowler, and Fred Hoyle [1], and the other is by Alastair G. W. Cameron [2]. This has been further developed into the field of nuclear astrophysics, which aims to explore and explain the origin of the elements in our universe.

To understand the nuclear physics behind all of this, some terminology is needed. Since nuclei contain neutrons and protons, these are notated N and Z respectively. The total mass number is denoted A, which is the sum of N and Z. By plotting the neutron and proton number on a grid, we find the nuclear physics equivalent of the periodic table, the nuclear chart as in fig. 1.1, which shows all nuclei measured so far.

There are two distinct regions of element synthesis; the elements lighter than iron, and the elements heavier than iron. The lighter elements fusing together is what keeps the stars, our sun included, shining. Hydrogen gets fused into helium through the proton-proton-chains (pp-chains), later fusing to carbon through the triple-α-process, and then into heavier elements if the star is sufficiently massive. At the end of a stars' lifetime, different deaths will come dependent on its mass, but most will explode in some manner, ejecting large amounts of matter into space, to reform into new stars, planets and other celestial objects.

The creation of the heavier-than-iron elements was a big mystery for a long time. One of the main differences of these elements compared to the lighter ones, is the average nuclear

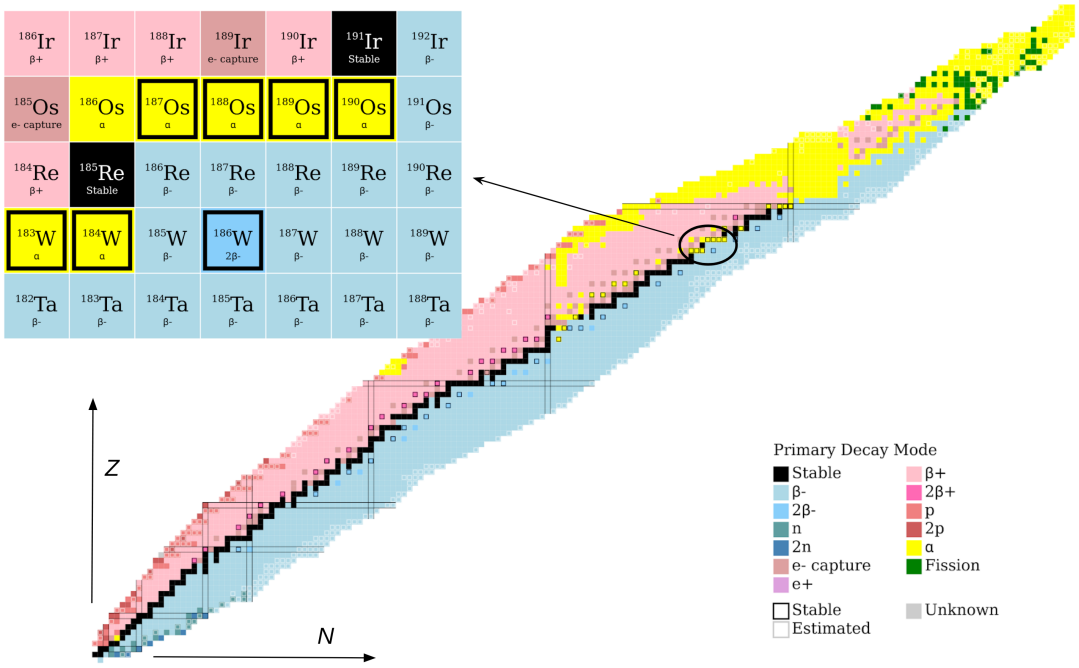

Figure 1.1: The nuclear chart of all known nuclei, where the number of neutrons is plotted in the x-axis and the proton number on the y-axis. The color coding shows the main decay mode, and the black squares are the stable nuclei, making up "the valley of stability". Generally, the further away a nucleus is from the stable ones, the more unstable it is and the shorter the lifetime. The zoomed area is of Z from 73 to 77, which is the tungsten (W), rhenium (Re) and osmium(Os) mass area. Figure adapted from [3].

binding energy, which peaks at iron. This means that fusing elements lighter than iron will produce excessive energy, but fusing trans-iron nuclei into heavier elements needs an energy input. Therefore, neutron capture reactions must be responsible for the formation of (most of) the heavy elements. However, free neutrons are not stable, and have a half-life of about 15 minutes, which means no synthesis relying on neutron capture can occur unless there is a production of neutrons.

Elements heavier than iron are made in a few different processes as outlined in B2FB[1] and Cameron [2]. One of them is the s-process[4], which is short hand for the slow neutron capture. This process relies on heavy, stable nuclei capturing neutrons in a low neutron-flux environment. If the new nucleus is unstable, it will β-decay, turning one of its neutrons into a proton. Then the process continues, forming ever more massive elements.

The counterpart to the s-process is the rapid neutron capture, nicknamed the r-process. This process takes place under extremely high neutron fluxes, forming nuclei close to the neutron drip line, i.e. the limit of where nuclei can even be bound. This process happens in some of the most extreme events in the universe, and evidence of the process was observed in a neutron star merger in 2017 [5].

The s-process and r-process are thought to be responsible of roughly half of the heavy elements each. These processes are only capable of producing nuclei on the neutron-rich side of the valley of stability, as well as nuclei that can decay from these. The whole proton-rich part of the nuclear chart is simply inaccessible. We do, however, have some proton-rich nuclei in our galaxy, totalling around 0.1-1 percent of the total abundance. These are thought to be made in the p-process, which is a distinctly different process than the latter ones. The p-process is not exclusive proton capture, but involves other reactions, in particular photodisintegration, of already formed heavy nuclei, such as, for example (γ, n), (γ, p) and (γ, α).

In this thesis, I am working specifically on the s-process, but by understanding more about the s-process, the better we can constrain the r-process contributions. The s-process might be a perceivable simple process, however, it is complicated by external factors from the astrophysical perspective of which these processes take place, as well as the branching points contributing to otherwise r-process exclusive isotopes. There are several branching points in the tungsten(W) and rhenium (Re) region, where the s-process nuclei which would normally β-decay might be long-lived enough to capture another neutron and become a stable nucleus again.

The final isotopic ratios of the s-process branching points is dependent on (n, γ) cross sections of unstable nuclei. Direct study with neutron beams are very challenging as neutron are both unstable and carries no charge for acceleration. Unstable targets also adds to the challenge and introduces the need for very specialised experimental setups for radioactive beams or on-site isotope production. Indirect study is therefore essential to work as replacements, and may use more available equipment such as the cyclotron used in this thesis. By understanding the s-process contribution to the branching point isotopes better, the relative contributions from the r-process and s-process may be understood better. This may in turn also help understanding the complex system of other synthesis, such as the r-process, by giving better estimates on these nuclei which, without an active branching point, may only be produced by the r-process.

To calculate the (n,γ) reaction rates and crosss sections, nuclear rection software such as TALYS[6] is important, where statistical properties of nuclei can be used to understand their interactions.

1.3 This work

This work focuses on the s-process branching point of ^{186}W, of which an illustration is given in fig. 1.2. The experiment discussed provides data on the reactions ^{186}W(α,d)^{188}Re and ^{186}W(α,t)^{187}Re from a single experiment. By applying the Oslo method, the nuclear level densities and γ strength functions are extracted from both ^{187}Re and ^{188}Re. This work also explores structural features of the γSFs which together with the NLDs enables the first experimental constrains on ^{186}Re(n,γ) in future work.

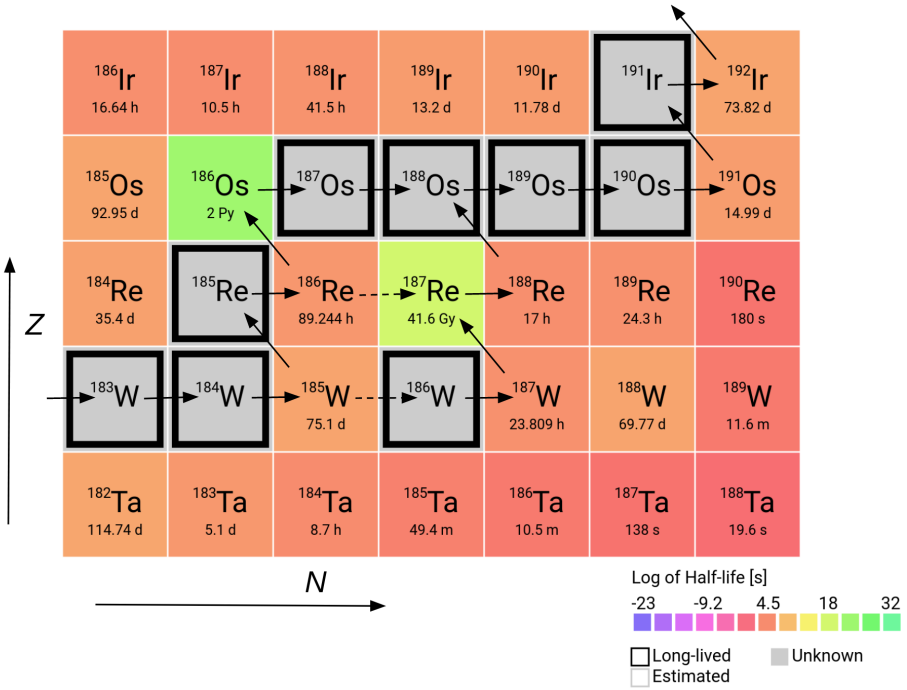

Figure 1.2: The s-process of the ^{186}W branching point. The horizontal lines are the neutron capture of stable nuclei, and the diagonal are β-decay, where a neutron is turned into to a proton. The dotted lines are the branching point neutron captures, which can lead to s-process producing stable ^{186}W and ^{187}Re. Note the lifetime of ^{187}Re on the scale of 40 Gy, i.e. $4 \cdot 10^{10}$ years. Figure adapted from [3].

Chapter 2

Nuclear theory of the quasi-continuum

> ***§15*** *Kongen kan bestemme at det skal innføres rett til ferietid i inntil 5 virkedager ut over ferietiden etter §5.*
>
> Utdrag fra Ferieloven §15, kapittel IV

To characterise nuclear excitation states above the discrete levels, we must use statistical methods and measurements to be able to quantify the nuclear behaviour. The most important we focus on in this thesis in the nuclear level densities, NLD, and the γ strength function, γSF, which can both be extracted with the Oslo method as explained in later chapters. This Oslo method also relies on the Brink hypothesis, which is a well discussed subject in nuclear physics. Both the NLD and γSF are important input parameters in Hauser-Feshback theory[7] of nuclear reaction codes, such as TALYS [6].

2.1 Defining the quasi-continuum

Before discussing characteristics of the quasi-continuum, it's beneficial to clearly define this concept. When looking at excitation levels of excited nuclei, the lowest excitations are discrete and well separated in energy. When exciting nuclei to these lower energies, specific states of spin and parity may be identified and we can make level schemes. Statistical properties become more prominent when there are many levels very close to one another. We therefore distinguish between the discrete, quasi-continuum and continuum region.

To help identify these regions, we make use of two parameters, D and Γ. The parameter D is the average distance between two levels in a given energy bin, $D = \frac{\Delta E}{\Delta N} = \rho$, i.e. energy of the bin per level in the given bin. This is also, per definition, the inverse of the level density $\rho = \frac{\Delta N}{\Delta E}$ of levels per energy. The Γ is the average width of the states which is dependent on the lifetime τ of the state as $\Gamma = \frac{\hbar}{\tau}$.

In the discrete energy region at low excitation energy, $\Gamma << D$, which means that the width of each state is significantly less than the distance between the levels, i.e. they are clearly distinct. As the energy increases the average distance between levels will decrease and the discrete levels will be harder to distinguish, which is the quasi-continuum region where $\Gamma \leq D$. In the continuum where $\Gamma \geq D$, levels are overlapping and statistical properties are the most appropriate to use.

2.2 Hauser-Feshbach and TALYS

The Hauser-Feshbach formalism is a statistical model of nuclear decay and reactions first developed by Hauser and Feshbach[7] in 1952. It is focused on the inelastic scattering of

neutrons, as the title of the original paper suggests, though it can be expanded for other reactions as well. This model is based on the assumption that the compound nucleus is sufficiently excited such that the angular distribution of the inelastically scattered neutrons is isotropic, as described in the original paper. The paper describes how, if the neutron energy is "moderate", only a few levels will be excited, and thus the total cross section, as well as the energy- and angular distribution of the scattered neutron will be dependent on quantities such as the angular momentum and parity of the populated levels. However, if the excitation energy is significantly higher, in what we now call the quasi-continuum and continuum, the inelastically scattered neutron will no longer have a strong dependence on these detailed properties but can be calculated from statistical properties, such as the nuclear level density and γ strength function.

The formalism is central in nuclear reaction codes, such as TALYS[6]. The code is available at `https://tendl.web.psi.ch/tendl_2019/talys.html` under a GNU General Public Licence.

Using TALYS is how further work can be done on the γSF and NLD of this thesis, to extract (n,γ) reaction rates. In the TALYS library there are many models available for use, and it contains large amounts of the available experimental data as well as theoretical estimates for nuclei of which we have little to no experimental data. For example are there several different theoretical mass models which also have theoretical estimations of deformation in ground state nuclei, which will be used later in this chapter.

2.3 Nuclear level density

One of the central statistical properties of nuclei is the nuclear level density, NLD, which is a measure of the number of levels per energy bin. As soon as we excite nuclei into the quasi-continuum, distinct levels become hard to distinguish, and the nuclear level density is a much more useful concept.

When the NLD is plotted as a function of excitation energy, $\rho(E_x)$ is an exponential function, often appearing roughly linear in a logarithmic plot. It's an important input into calculating cross sections in nuclear reaction networks, (as mentioned in section 2.2) and directly influence reaction rates which depend on available levels. Formally, we can define the total level density over all spins J and parities Π as a function of excitation energy E_x as

$$\rho^{tot}(E_x) = \sum_{J} \sum_{\Pi} \rho(E_x, J, \Pi). \tag{2.1}$$

When comparing level densities of different nuclei, there are some very significant patterns worth noting. In general, the further away from a shell closure you are, the more valence particles you have and the more levels you have, even at low excitation energy. There is also a strong reliance on whether the number of protons and neutrons are odd or even. As nuclei with even N, even Z have all their nucleons in pairs, the NLD is generally lower. The odd N, even Z or even N, odd Z nuclei have a single nucleon which is not bound in a pair, and will therefore have more levels on average. The odd N, odd Z nuclei, however, have two unpaired nucleons and will have an even higher level density compared to their neighbours.

These odd/even effect are generally very predictable and are only a constant factor off of their NLDs, appearing largely parallel when plotted together. This odd/even phenomena is also explored in M. Guttormsen et al. [8] where it is connected to entropy. In this paper they discuss the case of $^{160-162}$Dy showing a strong similarity between the even N, even Z ^{160}Dy and ^{162}Dy NLDs, and a larger NLD of the odd N, even Z ^{161}Dy. They observed that the single valence neutron contribute to the NLD with a constant factor of around $e^2 \approx 7.40$ compared to the nuclei without the extra valence neutron. If this is also valid for the odd N, odd Z ^{188}Re compared to the even N, odd Z ^{187}Re, then we should expect the level densities to be very similar in shape and related by a constant factor of around e^2 as $\rho_{188Re}(E) \approx 7.4 \cdot \rho_{187Re}(E)$.

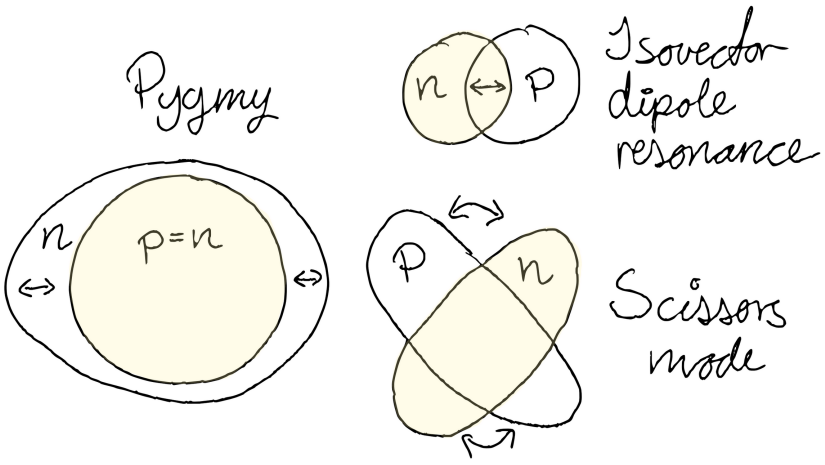

Figure 2.1: An illustration of the main different types of macroscopic resonances discussed. These are not to scale in any way, but can serve as a simplified main idea of these collective excitation modes.

2.4 The γ strength function

The γ-strength function (γSF) reveals the average γ decay behaviour of a nucleus, and is a measure of the average reduced partial radiation width. This is a very important property and together with the NLD can be used to calculate cross sections.

Defined as

$$f_{XL}(E_\gamma, E_x, I, \Pi) = \frac{< \Gamma_\gamma^{XL}(E_\gamma, E_x, I, \Pi) >}{D(E_\gamma, E_x, I, \Pi) E_\gamma^{2L+1}} \tag{2.2}$$

in [9], as a function of E_γ, spin I, parity Π, and excitation energy E_x where XL denotes the electromagnetic character and multipole type, such as $M1$ or $E2$. Assuming the spin and parity distributions of the initial and final states are statistically distributed and that we populate a wide variety in our experiments, we measure the average γSF of a wide spin and parity range. The γSF is assumed in the Oslo method to be dominated by E1-contributions with smaller contributions of M1 in the quasi-continuum.

The γSF is closely related to radiative decay and (n,γ) cross sections. Assuming the statistical γ-rays are dominated by dipole transitions, the γSF can be compared to previously measured photo absorption cross section, $\sigma(E_\gamma)$ by eq.

$$f(E_\gamma) = \frac{1}{3(\pi\hbar c)^2}\frac{\sigma(E_\gamma)}{E_\gamma} = 8.674 \cdot 10^{-8}\ \frac{\sigma(E_\gamma)}{E_\gamma}. \tag{2.3}$$

from [10]. Calculating with σ given in [mb] and using E_γ in [MeV], the total factor $\frac{1}{3(\pi\hbar c)^2} = 8.674 \cdot 10^{-8}\frac{1}{\text{mb}\cdot\text{MeV}}$ will give an output of the γSF in [MeV^{-3}].

The γSF displays resonance-like structures, such as the Giant Dipole-, the Pygmy- and Scissors Resonance, as well as a low energy enhancement. As illustrated in fig 2.1, the excitation modes discussed are largely isovector, i.e. the neutrons and protons are moving against one another in a simplified macroscopic picture.

2.4.1 Giant dipole resonance

The giant resonances are highly collective excitations, dominated by the isovector giant dipole resonance, (IV)GDR and they are usually very broad with a maximum value at higher E_γ. To be considered an actual giant resonance, the excitation has to be highly collective, meaning that

a high number of particles in the nucleus is involved in the excitation in contrast to for example single-particle excitations. Isovector means that the neutrons and protons are moving against each other, as illustrated in fig. 2.1 where they oscillate around a common center-of-mass.

The GDR can provide bulk properties of nuclei such as deformation and in ^{187}Re the GDR is double-humped, as will be seen later in the results-chapter, ch.6 in fig. 6.3. This was observed in a previous experiment from [11], and may be caused by K-splitting implicating that the nucleus is deformed[12].

2.4.2 Pygmy resonance

The pygmy resonance, of which a thorough review is given in [13], is located at the lower energy tail of the GDR at around $E_\gamma \approx 6 - 9$ MeV. It's been observed in many neutron rich nuclei, and is traditionally considered to be the effect of a $N \approx Z$ core with a neutron skin containing the excess neutrons oscillating against the common center-of-mass as in fig. 2.1.

It's a dipole E1 resonance and has previously been identified by using the Oslo method, for example in several of the $^{116-122}$Sn isotopes[14]. The centroid of the resonance has been observed both below, close to or above the neutron separation energy, as exampled by fig. 8 in the same paper, showing the centroid of the pygmy resonance in several Sn isotopes compared to their neutron separation energy. As it's a significant enhancement of the γSF and it might be close to the S_n, its presence may have important implications for the reaction rates and cross sections, especially in the r-process.

2.4.3 The scissors resonance

The scissors resonance is typically found around $E_\gamma \approx 2 - 4$ MeV and is generally dependent on deformation of the nuclei. It is only present in some nuclei, and can be understood both as a micro- and macroscopical phenomena.

Macroscopically, this resonance revolves around the idea of a common core of $N \approx Z$, but with the distribution of the neutron and protons oscillating against each other and have an orbital/spin-flip and rotational generation, resulting in the "scissors"-motion. A two-dimensional representation is drawn in fig. 2.1, but it is more of a three-dimensional motion than the illustration suggests.

Microscopically, as explained in [15], the SR are connected transitions described in the Nilsson model, which describes deformed shell model with additional splitting of levels compared to the spherical shell model. The resonance stems from $\Delta\Omega = \pm 1$ where Ω is a new quantum number describing the projection of the total angular momentum onto the symmetry axis of the nucleus. The bigger the deformation, the bigger the split of $\Delta\Omega$ and therefore the larger gap and higher E_γ directly dependent on the deformation.

The centroid of the scissors resonance is dependent on deformation, and according to [16] it should be following

$$E_x \approx 66 \cdot \delta A^{-1/3} MeV \tag{2.4}$$

where δ is the quadrupole deformation parameter and A is the mass number. Referencing TALYS's mass models there are theoretical estimates of the deformations on rhenium. Using these to give theoretical estimates of the centroid, we find values $E_x \approx 2.29 - 2.51$ MeV, as seen in table 2.1.

Systematics of experimental results of the scissors resonance has also been done, for example in J. Enders et al. [17], where results of approximately mass $140 \leq A \leq 200$ in the $N = 82 - 126$ major shell. Though they only considered even N, even Z, the systematics are still interesting for comparing to rhenium. Looking at their results in fig. 2.2a, the observed mean excitation energy E_x denoted ω_{M1} is consistently fluctuating around 3 MeV.

The observed summed strengths $\sum B(M1)$ shows a clear correlation to deformation in fig. 2.2c, and if we are to compare this to the strengths of $185 < A < 190$ in fig. 2.2a(b), we do not expect a strong M1 scissors strength in ^{187,188}Re, though it can be present. This assumes

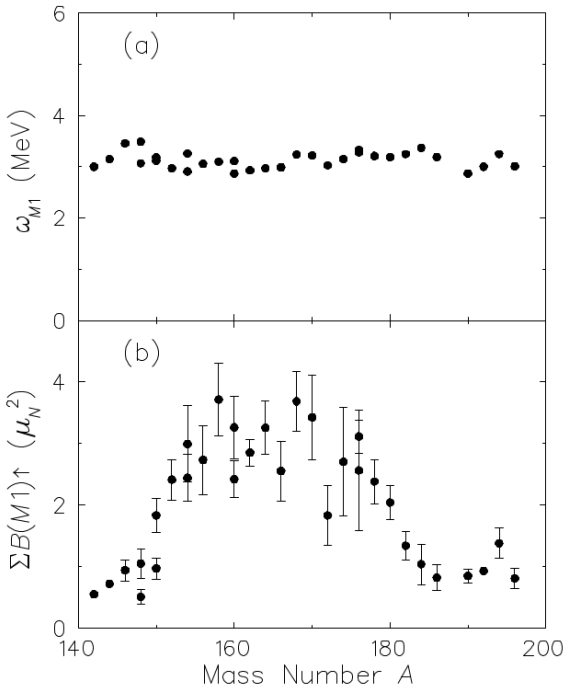

(a) Figure 1 from J. Enders et al. [17], comparing experimental results of the M1 strength that **might be related to** the scissors resonance. a) is the estimated centroids of the M1 strengths, and b) is the summed strengths of the M1 γs. Where the strength is significantly high, there is probably a scissors resonance.

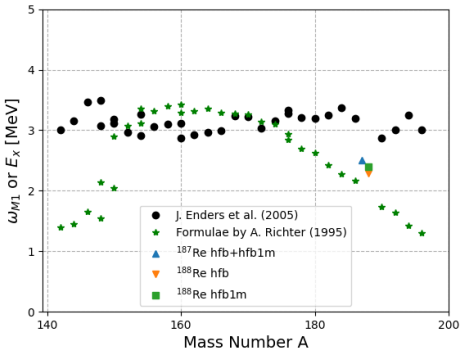

(b) Experimental scissors resonance energies reviewed in [17] in plot 2.2a(a) compared to the predicted mean excitation energies given by eq. 2.4 on the deformations and masses given in the same paper. The discrepancy of the data points below $A \approx 50$ and above $A \approx 180$ might be a consequence of the formula not being valid due to a lack of significant M1 scissors strength.

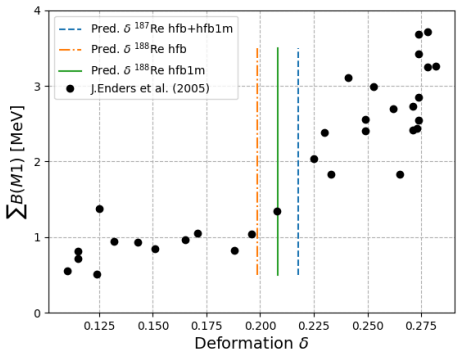

(c) Using the reviewed nuclei in [17] and plotting the strength of the scissors resonance as a function of deformation. The lines show the theoretical x-axis deformations of $^{187-188}$Re given in the TALYS mass model.

Figure 2.2: Systematic predictions of the presence of the scissors resonance in $^{187-188}$Re, based on eq. 2.4 from [16] and the systematic experimental review in [17]. Comparing the strengths of 2.2a(b) to the predicted centroids of fig. 2.2b, the centroid estimates of the nuclei with a significant M1 strengths are generally consistent between $150 < A < 180$.

Theoretical mass model	*Nuclei*	β_2	*Predicted* E_x [MeV]
Hartree-Fock-Bogolyubov	^{187}Re	0.23	2.51
with Skyrme force (hfb)	^{188}Re	0.21	2.29
Hartree-Fock-Bogolyubov	^{187}Re	0.23	2.51
with Gogny force (hfb1m)	^{188}Re	0.22	2.40

Table 2.1: The predicted centroid of the scissors resonance based on eq. 2.4 and $\delta = \beta_2 * \sqrt{0.8952}$, using the theoretical deformation from the hfb and hfb1m mass tables in TALYS.

that the odd/even N, odd Z nature of rhenium does not make it deviate strongly from their neighbouring even/even N, Z nuclei.

The scissors resonance has also been found to present stronger in Oslo method type experiments compared to photo induced type reactions[18]. This is widely discussed, but believed/hypothesised to be a result due to the different moment of inertia of the quasi-continuum compared to the ground state.

2.4.4 Low energy enhancement

There is also a low energy mode[19] that has been observed with the Oslo method previously[20], often called the low energy enhancement. This enhancement has been observed in the low energy γ up to around $E_\gamma \approx 3.5$ MeV. It has been observed in nuclei such as ^{95}Mo[21] and ^{56}Fe[20].

2.5 The Brink hypothesis

The Brink hypothesis was first proposed in the doctoral thesis of Brink in 1955 [22] and was further used and popularised by Axel in 1962 [10]. Brink originally wrote:

> "(Earlier) we have considered the nuclear photo effect from the ground state of the nucleus. Now we assume that the energy dependence of the photo effect is independent of the detailed structure of the initial state so that, if it were possible to perform the photo effect on an excited state, the cross section for absorption of a photon of energy would still have an energy dependence given by (15)"

It states the assumption that the general shape of the gamma strength is independent on the specific state on which it is built upon.

The assumption in the Oslo method, as discussed in chapter 4, is regarding the primary γ spectra, i.e. the first γ-rays emitted from a nuclei excited to an energy E_x. The method relies on the primary gamma ray matrix being factorised into independent functions, which can be done by using the Brink hypothesis, simplifying as

$$P(E_i, E_\gamma) \propto \tau_{i \to f} \rho_f \rightarrow P(E_i, E_\gamma) \propto \tau(E_\gamma) \rho_f. \tag{2.5}$$

Here, $P(E_i, E_\gamma)$ is the first generation matrix of initial state i, τ is the transmission coefficient and ρ_f is the level density at the final level f. This means that it is assumed the transmission coefficient/function is not specifically dependent on the initial and final spin, but in the γ energy only. This relies on a statistical compound nuclei and is not valid in low excitation energy with distinguishable levels. This means that the overall shape and distribution of the first generation γs are the same, independent of excitation energy.

By showing the general shape of the primary γ rays are preserved for different E_x, it does support the use of the assumption on the specific cases. As the nuclei studied in this thesis, ^{187,188}Re display very statistical characteristics due to their odd numbers of nucleons and being far away from any shell closures. It is therefore also reasonable to think a statistical approximation should be valid.

Chapter 3

Experimental methods and calibration

-"What are you doing?"
-"Spinning counterclockwise.
Each turn robs the planet of angular momentum,
slowing it's spin the tiniest bit
lengthening the night,
pushing back the dawn
giving me a little more time here
with you."

- xkcd.com/162

In this thesis, the reactions ^{186}W$(\alpha, d)^{188}$Re and ^{186}W$(\alpha, t)^{187}$Re have been used to extract the nuclear level density and γ strength functions of ^{188}Re and ^{187}Re. The experiment was done at the Oslo Cyclotron Laboratory (OCL) in March and April of 2016, with SiRi for particle detection and CACTUS for γ-detection. In this chapter I will describe how the experiment was performed and how to obtain the raw, calibrated matrices to use in the Oslo method.

For the calibration and data sorting, I used several software packages, such as ROOT, OCL usersort and peaks2D. Here, complemented by appendix A and https://github.com/Loopdiloop/master_thesis, a complete guide will be given of the steps of the sorting and main data analysis.

3.1 The Oslo Cyclotron Laboratory.

Located at the physics department of the University of Oslo, OCL currently has a unique experimental setup of $LaBr_3$ detectors and light ion detection. Serving mainly the nuclear physics-, biophysics-, and nucelar chemistry group, as well as collaborators, it is used for medical and fundamental nuclear research. It also provides hands-on training for educating master and PhD students. OCL is also a backup for local medical isotope production and there is flexibility on proposal of experiments. New collaborators are encouraged and welcome.

The Scanditronix MC35 cyclotron was originally built in Uppsala, Sweden, in 1978, and was producing it's first beam the year after, in 1979. It is capable of accelerating protons, deuterons, ^{3}He and ^{4}He in energies between $2 - 47$ MeV dependent on particle type, usually at an intensity of a few nA.

The brand new system of Lanthanum-Bromide ($LaBr_3$:Ce) detectors named the Oslo SCintillator ARray (OSCAR) was commissioned in January 2019. It consists of 30 detectors in a spherical array, with a significant improvement in both timing and energy resolution compared to previous setups, opening possibilities of new experiments. This will, for example, be used for prompt fission energy research where it is predicted to be able to discriminate between

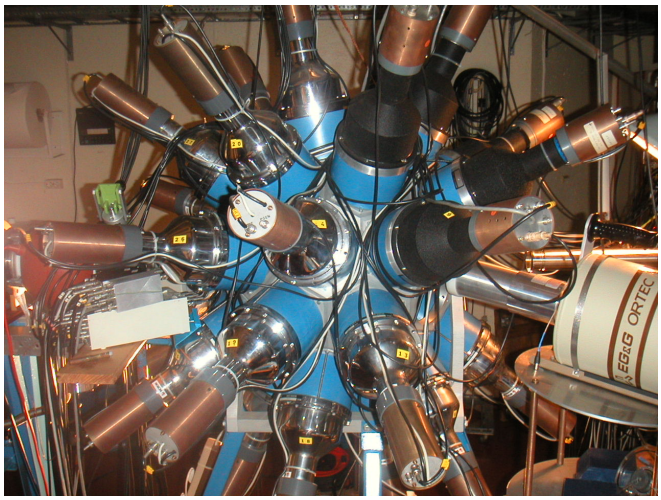

Figure 3.1: The CACTUS detector array.

γ-radiation and delayed neutrons. This thesis uses data from the previous NaI setup, CACTUS[1], as described in later sections.

3.2 CACTUS for γ detection

CACTUS, pictured in fig. 3.1, is an array of up to 28 NaI:Tl 5in.×5in. γ-ray detectors [23], whereas 26 of them were used in this experiment due to geometrical constraints of the cylindrical target chamber used. The detectors were placed at six different angles relative to the beam direction, as shown in fig.3.2, spherically enclosing the target chamber with the particle detector array SiRi within. This also enables angular correlation analysis if the amount of data is sufficient.

The detectors have 10cm thick conical lead collimators to suppress Compton scattering with front openings of 70mm, and absorbers of 2mm thick Cu in front of the opening to reduce incoming X-rays. Each detector covers a solid angle of 0.53% of 4π, and the array has a total efficiency of 14.1(1)% at 1332keV for 26 detectors, measured with a ^{60}Co source.

The high energy γ entering the crystal will produce photons in the visible range, which hit a photocathode and releasing electrons which are further amplified by the photomultiplier tubes attached to each detector. The signal is then collected and sent as analogue electric signal to a shaper which produces a well behaved signal to be read in an analog-to-digital converter (ADC) which gives the photon energy, and a time-to-digital converter (TDC) giving a coincidence time signal from a leading-edge discriminator. When an event in SiRi is triggered, a gate is opened in the ADC for 2μs and the TDC for 1.2μs.

3.3 SiRi for particle detection

SiRi[24] is a silicon ring detector for charged ion particle detection, made to measure the incident energies and discriminate between charged particles. The detector consists of two layers, one thin front counter, dE, with a thickness of $\approx 130\mu$m, and a back counter E which is $\approx 1550\mu$m thick. There are eight main sections of SiRi. Every thin dE-layer has eight individual strips each, totalling 64 individual detector combinations as can be seen in fig. 3.3. The back counter is not segmented into strips and is then correlated with dE to discriminate different outgoing particles of different energies.

[1] Named so as it looks kind of spikey like a cactus.

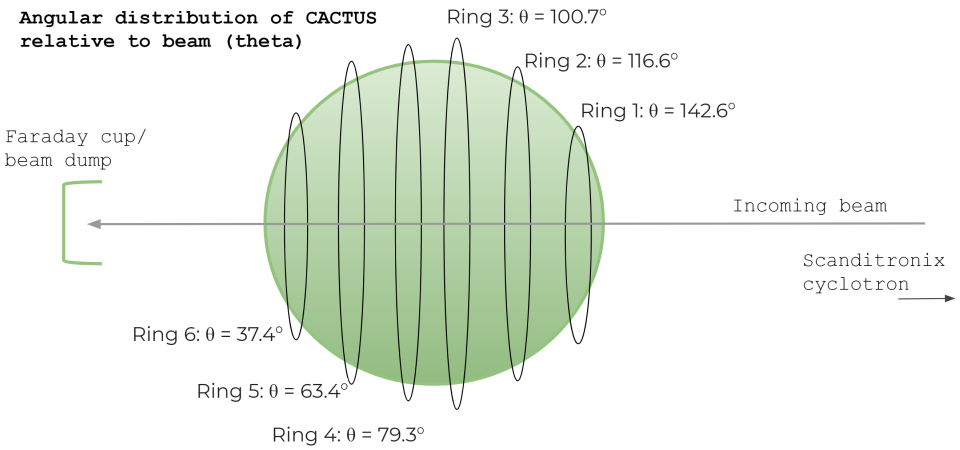

Figure 3.2: Angular distribution relative to the beam direction of the NaI detectors in the CACTUS array.

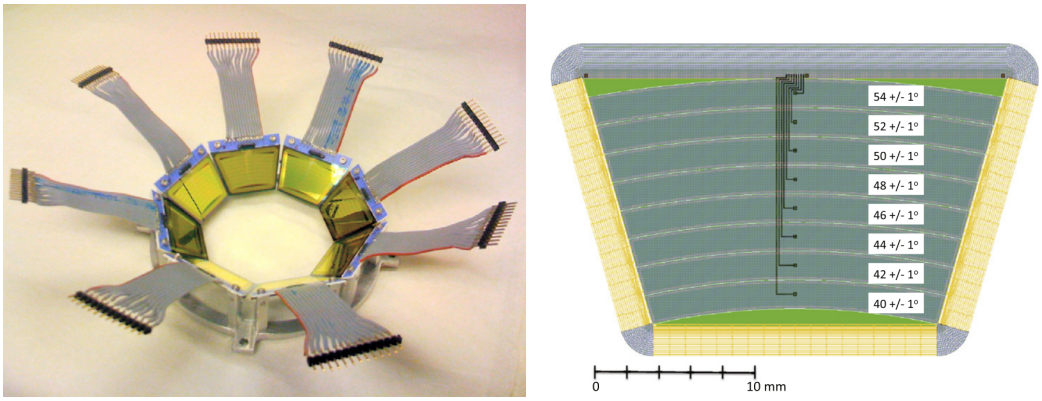

Figure 3.3: The SiRi-detector (left) and the dE angles relative to the beam in forward angles (right). In the experiment discussed in this thesis, SiRi was placed in a backwards angle corresponding to angle $\theta_{backwards} = 180° - \theta_{forwards}$. Figures from Guttormsen et. al. [24].

Target			
	^{186}W thickness	Carbon backing	
	0.31 $\frac{\text{mg}}{\text{cm}^2}$	24 $\frac{\mu\text{g}}{\text{cm}^2}$	
α-Beam			
	Energy	Intensity	RF frequency
	30 MeV	$1.5 - 2.2$ nA	23.76 MHz
Target chamber			
	Length of cylinder	Inner diameter	
	48.0 cm	11.7 cm	

Table 3.1: Specifications of target and beam of the experiment.

The particles will deposit some energy in the thin front counter before depositing the rest in the thick back counter. This will form the characteristic "bananas", as in fig. 3.4. Here, the $Z = 1$ particles , i.e. the protons, deuterons and tritons, are clearly distinguishable. If the particles are not stopped in the thick E-counter then we have punch-through, and this will render the signal in these areas ambiguous and therefore not usable. This is therefore a limiting factor to the beam energy used in a given experiment.

SiRi is located within the cylindrical target chamber and centered around the beam, mounted such that the centres of each section is 5cm from the target center. At backward angles, which was used in this experiment, the detector spans 140° to 126° relative to the beam direction.

The detectors also require a bias voltage on the back detectors of 360V to be fully depleted, and due to this high voltage, the detectors also have guard rings. It also has a thin $\approx 10.5\mu$m cover of aluminium foil to suppress δ-electrons.

The signals detected in SiRi are sent directly to five pre-amplifiers, one responsible for all eight E-counters, and the other four are connected to 16 strips in the dEs each. The signals are then sent to a shaper and a leading-edge discriminator with an energy threshold. It is then finally to an ADC. When one E-detector is triggered above the set threshold, it opens a master gate for the TDC for 1.2μs and all ADCs for 2μs sending the data from both the NaI γ detectors and SiRi to an event builder. This creates a single event with a time, γ-energy and particle information, which is saved for later analysis.

3.4 The experiment and raw data

The experiment discussed in this thesis was done at OCL with a 30 MeV α-beam on a ^{186}W target with carbon backing, see table 3.1. The master gate trigger set at a threshold of 200mV in the thick E back counter of SiRi. This experiment was originally optimised for a scattering experiment of (α, α') on ^{186}W, meaning that there is punch-through in the protons due to them not being stopped in the back counter of SiRi.

To be able to do the Oslo method analysis, we need to know the excitation energy of the nuclei calculated from the outgoing particle, as well as the γ-rays measured in coincidence. We are also interested in all energy bins from low energy (g.s.) up to the neutron separation energy S_n, as the Oslo method can not be used above the neutron separation energy since γ-decay will compete with neutron decay. Some fundamental information on the relevant nuclei such as the neutron separation energies, half lives and ground states are shown in table 3.2.

There is also a README.md in the github at `https://github.com/Loopdiloop/master_thesis` with instructions on running. This project used Qkinz version 1.3.0[2] to do kinematic

[2]Qkinz can be found on the github of OCL at `https://github.com/oslocyclotronlab/Qkinz`

		^{186}Re	^{187}Re	^{188}Re
Ground state				
	Spin and parity	1^-	$5/2^+$	1^-
	Lifetime	≈ 3.72 d	$\approx 4.33 \cdot 10^{10}$ y	≈ 17.0 h
	Main decay	β^-	β^-	β^-
Binding energy				
	S_n [keV]	6179.38 ± 0.17	7360.71 ± 0.87	5871.65 ± 0.04
	S_p [keV]	5828.26 ± 0.68	5996.92 ± 1.12	6401.81 ± 1.12

Table 3.2: Details of the experiment and propertiesof $^{186-188}$Re, from the National Nuclear Data Center (NNDC)[25]

calculations and ROOT build v6.22[3] for calibration. I also used Python 3.8[4], but the python scripts I've used are simple enough to not be very version dependent.

The raw output files need to be sorted into ROOT-files for analysis using sorting code based on the usersort-code from OCL, https://github.com/oslocyclotronlab/usersort. Here, there is also some flexibility on what data to sort, changing gain and shift, and adding gates on particle peaks and species. My software version used for this thesis can be found at https://github.com/Loopdiloop/master_thesis within the folder "usersort" and contains several specific files for this analysis. For clarity, sorting in this context means taking the raw data files and filter, then add calibrations and make raw arrays and matrices into .root files that can be handled and opened in ROOT. The initial sorting was run with a constant shift of 0 and gain of 5 for E and 2.5 for dE, which is taken into account when calculating the correct gain and shift.

3.5 Particle energy calibration and peak identification

To calibrate the energy of the outgoing particles in the banana plots of SiRi, we need at least two reference peaks to do a linear fit. Firstly, we had to identify as many peaks as possible in the spectra, both to understand the data better and find peaks that are known. We then did kinematic calculations with Qkinz, and then did a linear calibration in comparison to this.

To find peaks to use in the calibration, a good candidate is the triton ground state, see fig. 3.4. This is supported by Lu et. al [26], who performed the same ^{186}W(α, t) at 60° in 1971, see fig. 3.5. The triton ground state peak should be a pure ground state, as the next significant peaks in the spectra are located at around 400keV.

We also found peaks from ^{16}O$(\alpha, p)^{19}$F, due to oxygen in the target and carbon backing. The excited level at 2779.8 keV $(9/2^+)$ in ^{19}F was strongly populated and well isolated from other peaks so we were able to use it.

For both peaks I used two dimensional Gaussian fits for all 64 combinations of the eight dE- and eight E-counters of SiRi[5]. This script zooms in visually on the peak you want to fit and then does Gaussian fits parallel to the x- and y- axis, and diagonal fits 45° relative to the axes. This gives two very close estimates of the centroid, of which I used an average.

These fits were compared to kinematic calculations in Qkinz. These calculations assume angular symmetry around the beam and give separate values for each of the eight strips, i.e.

[3]ROOT v6.22 was run on Ubuntu 20.04. It can be found on ROOTS official website here: https://root.cern/releases/release-62202/

[4]Python is used with additional packages such as numpy, matplotlib and others. They are specified in each plot.

[5]This was done using the automated script peaks2D.cpp by Alexander Bürger in ROOT as described in the github[27]

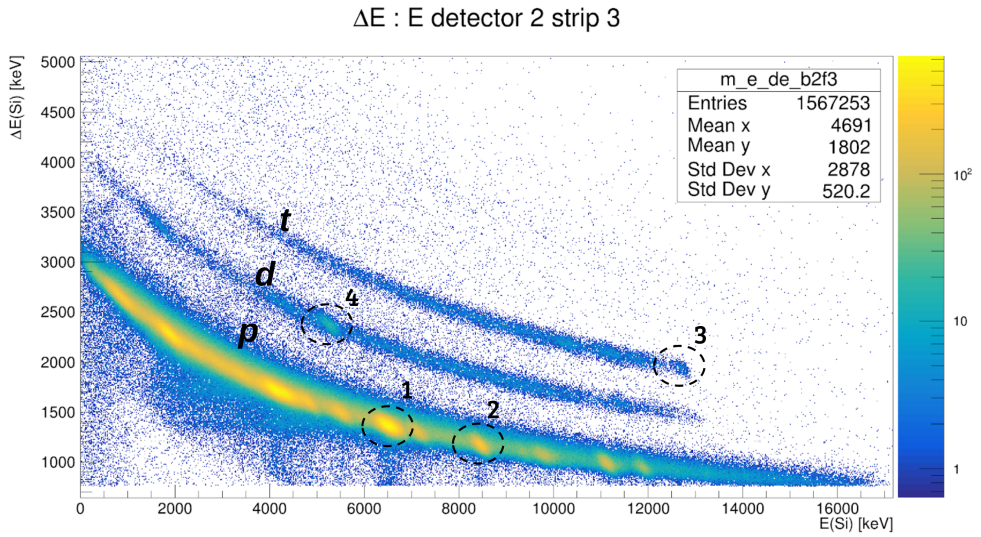

Figure 3.4: Data from one of the 64 detector/strip combinations of SiRi. Proton-, deuteron- and triton bananas are plotted as E-dE of energy deposited from the particles in the front and back detectors of SiRi. Peak 1 is ^{15}N excited to 5270.2keV, peak 2 is the 2779.8keV excitation level in ^{19}F, and peak 3 is the ground state of ^{187}Re. Peak 2 and 3 is used for the particle calibration of the banana plots in section 3.5, and peak 1 and 2 is gated on to calibrate the γ energies in section 3.6. Peak 4 is a contamination from ^{16}O which is later visible in the matrices. These circles are not representative of the sizes of the gates used in the analysis.

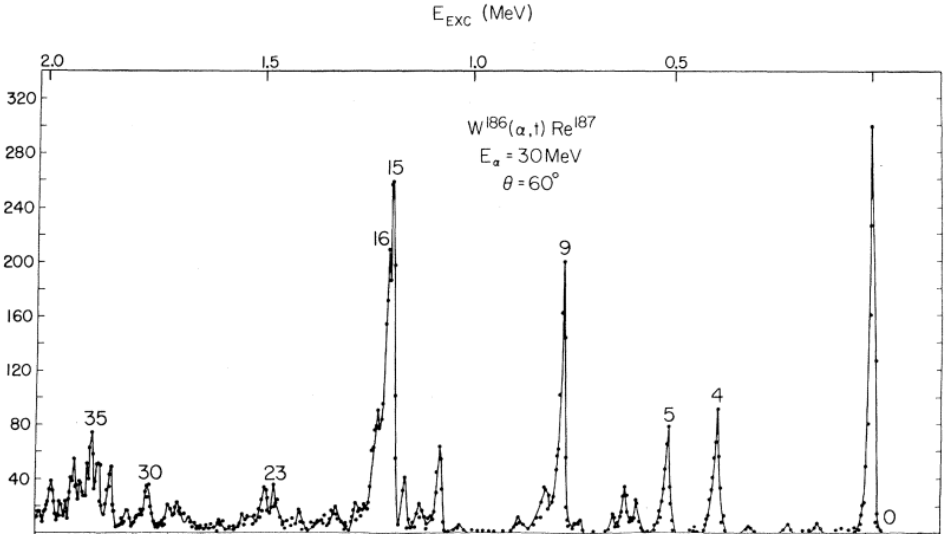

Figure 3.5: Figure from Lu et. al. [26] showing their measured populated levels from the reaction ^{186}W$(\alpha, t)^{187}$Re. The ground state, peak 0, is well separated from other lower lying states, confirming that the ground state in the triton dE-E "banana" in fig. 3.4 as being the isolated ground state. This experiment was done with the same target and beam, although this measurement is performed at 60° relative to the beam direction, compared to our $126 - 140°$.

angles, of SiRi. Then all 64 combinations of strips and sections are compared to the eight different angles, and calibration factors (gain and shift) are calculated as a linear calibration as:

$$calibrated = raw \cdot gain + shift \tag{3.1}$$

These values went back into the usersort program in the gainshift-file(see appendix A.3), together with corrections for the initial gain and shift used[6].

After adding this calibration, when looking at a plot of the E-dE of all the different strips, peak 4 in the deuterons of fig. 3.4 seem to be very angle dependent. This peak stems from ^{16}O of unknown origin. Several hypotheses were tested as to the origin of the oxygen. As it's located in the deutron "banana", ^{14}N(α,d)^{16}O seems like the most plausible candidate, though the prescence of large amounts of ^{14}N is not known, but it would have to be present on the target to produce such an amount of reactions, which means that imperfect vacuum could not account for this. It is still present in the final raw matrix, but as it is located above the neutron separation energy S_n of ^{188}Re, it does not interfere with the further analysis.

3.6 γ-calibration

To calibrate both the energy and timing of the γ-spectra, we used gates in the particle spectra, plotting all the γ coincidences of these events only. I used peak 1 and 2 from fig. 3.4, which is the 5270 and 5298 keV excitations of ^{15}N and the excitation level at 4648 keV from ^{19}F. These excitations result in the γ cascades in fig. 3.6. Finding and identifying these peaks included a lot of testing and cross-validation with correlating γ's, but the final identified cascades can be seen in the simplified decay schemes of fig. 3.6.

The gates on the residual particles are added as conditional statements in the usersort code, when filling events into the plot. The gate is added such that events of E $\in [7930, 9030]$ keV and dE $\in [1040, 1300]$ keV, or if E $\in [6050, 7200]$ keV and dE $\in [1200, 1520]$ keV which looks like:

```
#if defined(MAKE_CACTUS_TIME_ENERGY_PLOTS) && (MAKE_CACTUS_TIME_ENERGY_PLOTS>0)
    if((e_int>7930 && e_int<9030 && de_int>1040 && de_int<1300) || (e_int>6050
    && e_int<7200 && de_int>1200 && de_int<1520))
    {
        m_nai_e_t[id] ->Fill( na_e_int,  na_t_int );
        }
        ...
#endif
```

and if this is true, add the event to a γ-t plot[7]. This γ-t plot shows the γ energy of the detected γ's as a function of the time relative to the event trigger.

The ^{15}N, produced by reactions on the carbon backing by ^{12}C $(\alpha, p)^{15}$N, was strongly excited up to the $5/2^+$ state at 5270.2 keV and the $1/2^+$ at 5298.8 keV. Due to the energy resolution, these can not be separated. Both are therefore used, and as they differ no more than 28.6 keV or 0.5% of the absolute value, it should not introduce significant error. They both decay straight to the ground state with γs of 5269.2 keV and 5297.8 keV. There is also a cascade from ^{19}F's excitation level $13/2^+$ at 4648 keV with a 100% branching to $9/2^+$ 2779.8 keV producing a γ at 1868 keV, and from $9/2^+$ to 197 keV with a γ of 2582 keV. Choosing the most distinct peaks and the best energy span of the peaks, we used the 5270 keV from ^{15}N and the 1868 keV from ^{19}F to do a fit.

Plotting the time correlated γ peaks in all 26 NaI detector spectra, we had to manually set the correct interval of the y-axis to enclose the prompt events in the time spectra as seen in fig. 3.7. The other lines of coincidences above and below the prompt events is a result of the frequency of the beam pulses from the cyclotron.

To do the fit, the data in the set range is then projected down onto the x-axis to do a Gaussian fit of both peaks in each detector[8]. The centroid from each peak was saved to file

[6] i.e. the gain and shifts mentioned in section 3.4. This is very simple, but important to remember.
[7] Please refer to the github[27] for details.
[8] This was also done with a script , see the github[27]

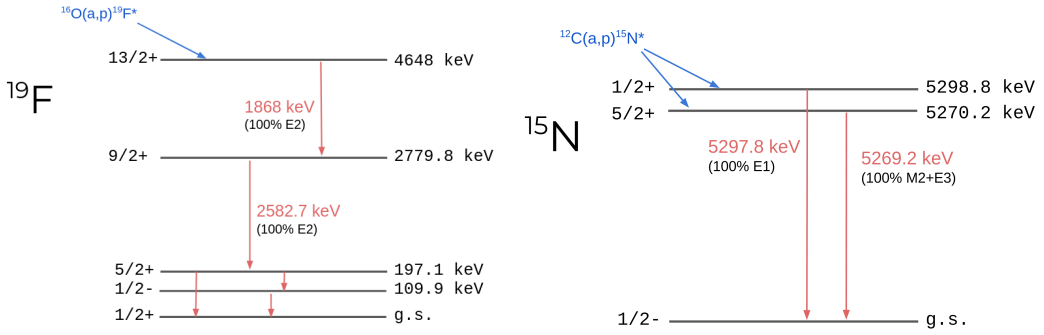

Figure 3.6: The γ cascades and decay from the first $13/2^+$ state in ^{19}F and the first excited $5/2^+$ and first $1/2^+$ in ^{15}N. These correlating γ cascades were used in the γ energy calibration. Both schemes based on γ- and excitation information from NNDC[25]. This level scheme is simplified to only contain the information relevant for this analysis.

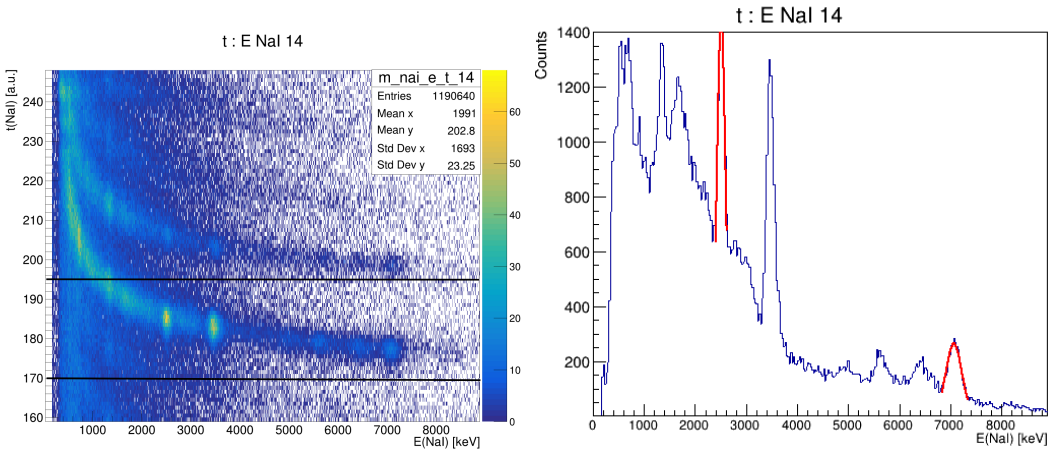

Figure 3.7: One of the 26 NaI detectors γ-t plots of γ-rays relative to the internal time of the event. This is the energy calibration of γ peaks supposed to be at 1868 keV from ^{19}F and 5269 keV from ^{15}N. The 2582 keV peak from ^{19}F can also be seen between 3 and 4 MeV as well. By projecting everything between the cuts of the left plot down onto the x-axis, we obtain the right hand plot. A Gaussian fit is done to both peaks and the centroids are used for the linear calibration.

and used to make another linear fit of gain and shift for all individual detectors. These were then added to the gainshift file as well.

The second stage after calibrating the energy, i.e. the x-axis, the prompt events needed to be lined up in time. The exact value we line it up to is not important, but for practical reasons they are lined up at channel = 200. Since the x-axis is already calibrated, the same gate on the x-axis around the 5269 keV peak was used for all the detectors from bin 715 to bin 787 and projected onto the y-axis, as seen in fig. 3.8. A Gaussian fit is then also done and shifts are calculated and added as well. This initial line up is needed both to align the time spectra, but are also important for the leading edge-correction later, as that is only done once for the whole data set.

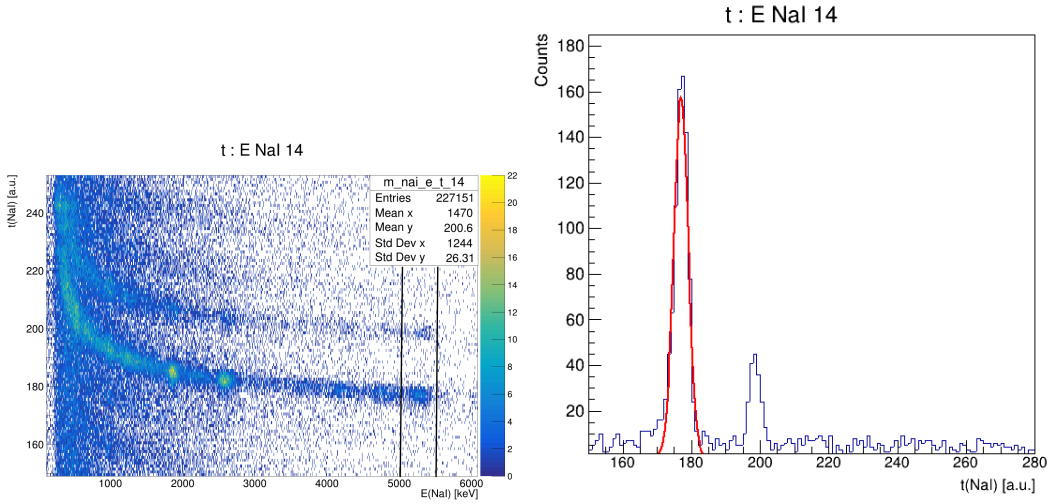

Figure 3.8: Time lineup of the γ spectra, centering the 5 MeV peak around relative time $t =$ channel 200 on the y axis. A gate is set in the same fashion as in fig 3.7, though here on the x-axis since the energy here is already calibrated. This peak is then used to calculate shifts to align the time of all detectors.

3.7 Leading edge corrections

The electronics was set to trigger at a fixed threshold, i.e. a leading-edge discrimination. This means that lower-energy signals trigger in the detector at a later time than higher-energy signals, since it takes longer for a low energy signal to reach the set threshold compared to a higher-energy signal. This is what is causing the low energy upturn in e.g. fig. 3.7. This will need to be corrected for both in the NaI γ detectors and in SiRi. To make the trend in the data more visible, the particle gate previously used is removed, and for the γ correction, all coincidences in the whole proton banana is plotted. The protons are used purely due to the statistics being better than deuterons and tritons, but the fit is then confirmed to be applicable for deuterons and tritons as well.

The leading edge needs to be corrected and it has been found in [24] that the function

$$t(E) = t_0 + \frac{\alpha}{E+\beta} + \gamma E = 200 + \delta t_0 + \frac{\alpha}{E+\beta} + \gamma E, \tag{3.2}$$

where $t_0 = 200 + \delta t_0$ to line up at channel 200, and this is a generally good fit that is used and has already been implemented in the usersort input. Essentially how it can be done in ROOT[9] is to draw a manual function "on top" of the data in the energy-time plot and fitted with least squares to the equation above. This produces the four parameters δt_0, α, β and γ, of eq. 3.2 which is also added in the input file of usersort. This will ideally "straighten" out the prompt event "banana". It also centers the peak around channel 200 to make it easier to set a gate around these prompt coincidences later.

To ensure minimal loss of low-energy data points, we need a leading edge correction in the particle-time spectra as well. This was done by plotting all the deuteron-data and manually drawing over the data, as in fig. 3.10, approximating the effect. The imposed graph is then also fitted to the same equation as for the γs and the parameters are also added to the batchfile. Without this correction, we would lose a lot more low-energy particles inside the time gate, and would lose more data in the higher E_x region, making a visible lack of data close to S_n.

[9] For how to do this with ROOT, there is a guide in the calibration folder of the github[27]

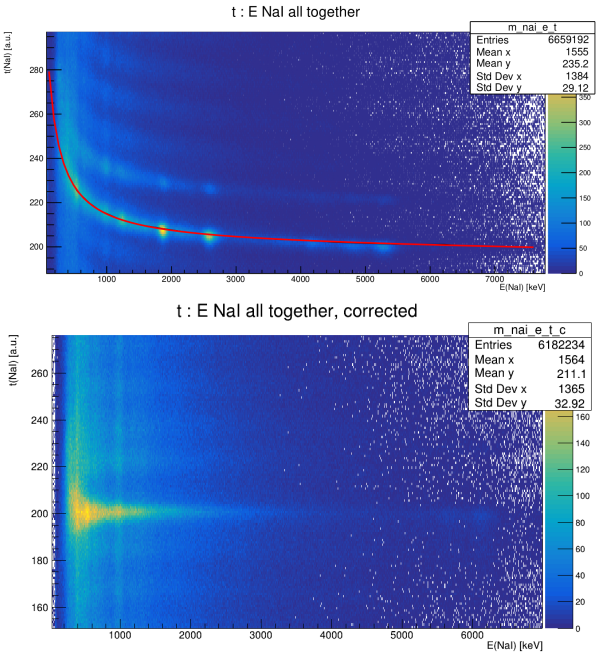

Figure 3.9: The correction of leading edge effects for the γs in CACTUS. Here, a gate on all protons are used for the coincidences. The second plot shows how the correction looks for (α, d) after the leading edge correction of SiRi as well, as this can affect the result.

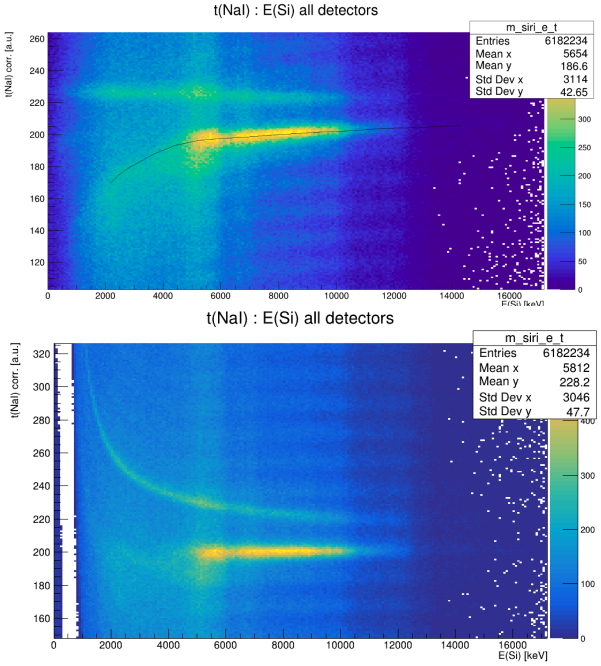

Figure 3.10: The correction of leading edge effects for the protons in the E detectors of SiRi.

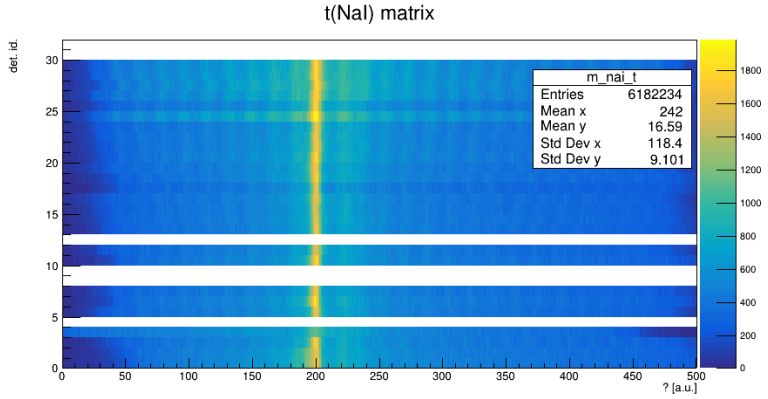

Figure 3.11: The final time lineup of $(\alpha, d\gamma)$ for all NaI detectors after a manual correction.

3.8 Final data adjustments before analysis.

A final time-lineup is done after the leading-edge correction to line up the final, straightened spectra of the γ spectra properly. This was done manually and corresponds to the final shift in the NaI timing in the final calibration. The result can be seen in fig. 3.11.

The first generation matrices, as in fig. 3.14, are the ones we will be using in the further analysis and Oslo method, and it is plotted as a scatter plot of $E_\gamma - E_x$. The diagnoal at $E_x = E_\gamma$ is when the nuclei are being excited to E_x and decaying directly to the ground state with a γ of corresponding energy. A small, additional correction of E_x in (α,tγ) is needed, as the data in the uncorreted matrix in fig. 3.13 doesn't hit $E_x = E_\gamma$ quite as well as expected.

Looking at the $E + dE$ spectra of both $(\alpha, d\gamma)$ and $(\alpha, t\gamma)$, they both look good other than a small change of the particle energies in $(\alpha, t\gamma)$. The ground state is not centered properly on $E_x = 0$, so a final shift was needed, as seen in fig. 3.12. There is also a peak around ≈ 800 keV after the calibration, which, compared to the plot in fig 3.5 in this thesis from Lu. et al [26], should be what they named peak no. 9 at 775 keV[10]. There is also a large peak at $\approx 1200 - 1300$ keV, which seems to correspond to the double peak no. 15 and 16 at 1202 keV and 1208 kev respectively. The data for Lu et al stops at 2.0 MeV, so the peak above that in our data could not be used for comparison.

We know, however, that Lu et al. has their data from a 60° angle, so there might be changes compared to our data. Using the groud state and double peak would, in theory, give a better span for calculating the shift and gain, but doing so is not possible for both peaks.

We then, choose to instead do a shift to line up the ground states, and a moderate reduction of 5%. I used Gaussian fits on the ground state peak of each of the eight rings of the different angles to shift the spectra to center the ground state at $E_x = 0$. We then evaluated the peak in the matrix in fig. 3.13, at around 800 keV in both the x- and y- axis and lining this up such that $E_x \approx E_\gamma$ by lowering the the E_x values by 5% by adding a gain of 0.95. The final result is the shifts and gains for each ring in rising order for the (α,t)[11]:

```
# empirical excitation energy correction for the above, e.g. from known peaks
parameter ex_corr_exp    = 43 0.95 \
    63 0.95 \
    48 0.95 \
    45 0.95 \
    58 0.95 \
    54 0.95 \
    51 0.95 \
    51 0.95
```

From this we end up with two $E_x - E_\gamma$ coincidence matrices with corresponding d or t gates, one for ^{187}Re and one for ^{188}Re as shown in fig. 3.14.

[10] Which, if you search in modern databases has been updated to a peak at $E_x \approx 773$ keV

[11] This was added in the batch(input) file of usersort for (α,t) only, see `batch_W186_a_t.batch` in the github[27]

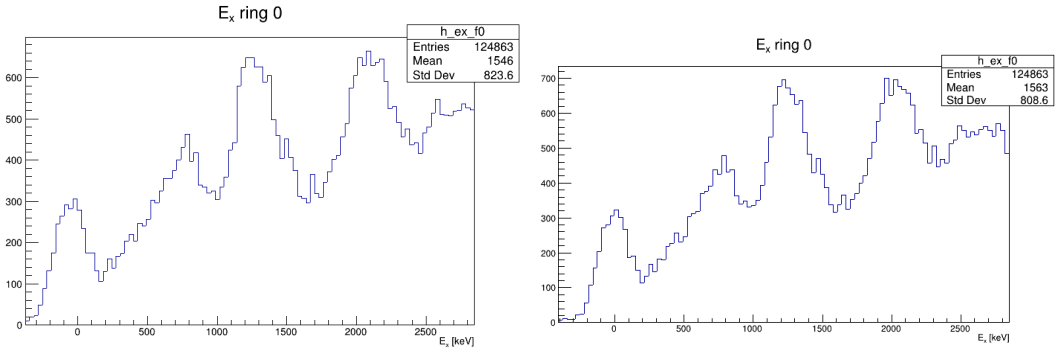

Figure 3.12: The E_x from one of the angles relative to the beam in SiRi for the final, manual correction of the $\mathrm{E}_x in(\alpha, t)$.

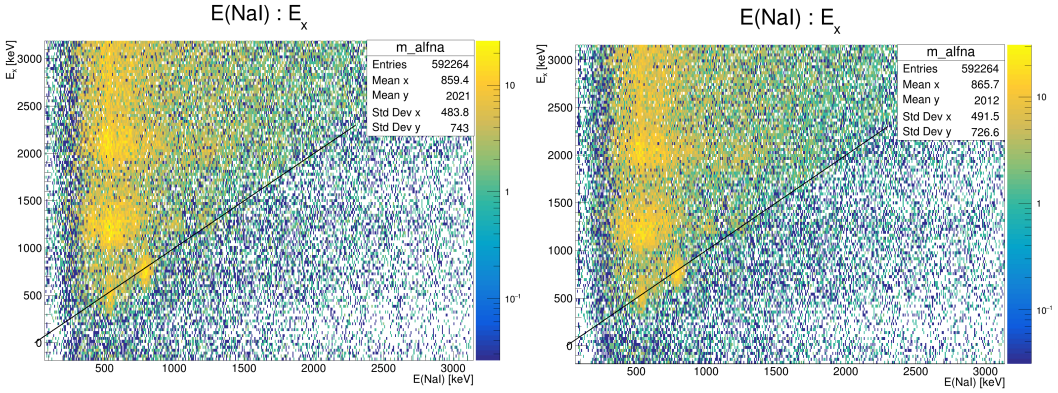

Figure 3.13: Comparison of the (α,tγ) E_x vs. E_γ plot before the final corrections on the left hand side and after the corrections on the right. The shifts were found by evaluating the ground state of the E_x plots for each ring as in fig 3.12. The 5% reduction in gain enabled the line up of the peak around $700 - 800$ keV, as well as the general trend at higher energies where the E_x generally was a little high compared to the E_γ. The black diagonal line shows $E_x = E_\gamma$.

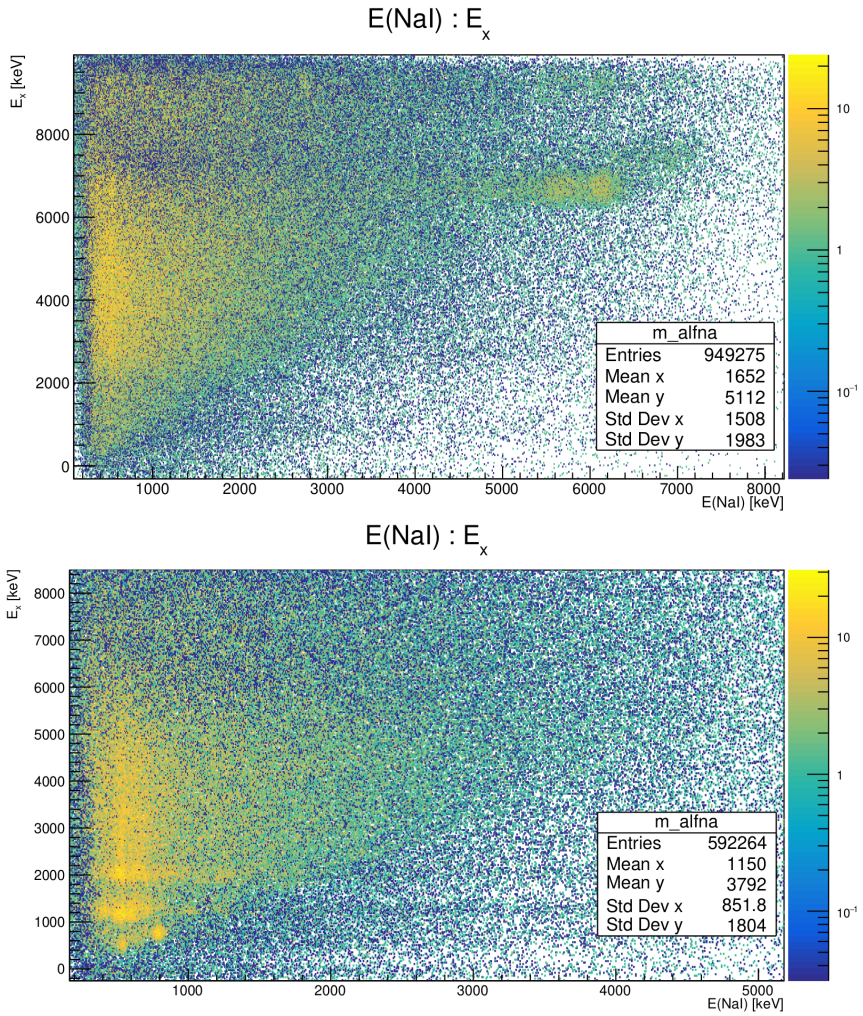

Figure 3.14: The $E_x - E_\gamma$ matrices, not rebinned, of both $(\alpha, d\gamma)$ (top), and $(\alpha, t\gamma)$ (bottom). The raw bin sizes for both matrices are 7.0 keV/channel on the x-axis, and 31.0 keV/channel on the y-axis. The peak in the upper panel at around $E_x = 6 - 7$ MeV, is from ^{16}O.

Chapter 4

The Oslo method

> Today, we consider the previous methods as premature, and we will now present in the following a completely new, exact and convergent technique...
> It is of course discouraging that an infinite number of equally good solutions exists...
>
> A. Schiller et al. [28]

The Oslo method is a collection of methods to extract both the γ strength function (γSF), and the nuclear level density (NLD) from a single data set of particle-γ coincidences. The first generation γs are extracted from an unfolded spectra and used to find the γSF and NLD. The NLD must then be normalized to known excitation levels and calculated level density for the neutron binding energy. The γSF is then normalized as a result of the NLD normalization parameters and $< \Gamma_0 >$ from literature.

4.1 Development, use and input.

The method was developed by the nuclear physics group at the University of Oslo and was first described in 1983 [29]. It has been continuously improved, refined and expanded ever since, for example with a thorough analysis of the method in [30]. The Oslo method with inverse kinematics has also been developed and was first used by Ingeberg et al. [31], whereas another version based on β-decay has also been developed, firstly by Spyrou et al. [32].

One of the limitations of this method is that the γSF and NLD may only be extracted up to the neutron separation energy threshold where γ emission will then begin to compete with particle (neutron) emission. The analysis is also dependent on the validity of the Brink hypothesis as outlined in chapter 2.5 and external data to normalize the results.

The input to the Oslo method software must be a matrix of calibrated data from one single reaction channel. The y-axis is the excitation energy calculated from the outgoing, charged particle and the x-axis is the corresponding γs.

4.2 The iterative unfolding

The raw γ-ray spectra must be unfolded, i.e. the γ-ray spectrum for every excitation energy bin must be unfolded according to the detector response of the specific experimental setup. This must be done as the signals recorded in the γ-ray detector does not only show the full-energy peak. A mono-energetic input signal would produce a peak of its original energy, but also single- and double escape peaks, the 511-keV peak (from back scattering of electron - positron annihilation), Compton scattering and so forth. The response functions are unique to each detector setup and must be known to be able to unfold the detected γ-ray spectra. It is therefore essential to use the correct response matrix when running this analysis.

To unfold such a collection of signals can be done by several different methods, such as a matrix inversion[33], by neural networks [34] or by iterative unfolding. Some solutions may be computationally taxing and might be unstable and introduce artificial fluctuations. The currently used iterative method described in [35] has proven to be very stable and focuses on reproducing the raw spectra. The Compton subtraction method is a unique feature of this technique. Using this method preserves and propagates the statistical uncertainties and does not introduce significant artificial fluctuations. Unfolding is a non-trivial problem, and a stable solution is especially important in data sets with poorer statistics, such as the one used in this thesis.

Assuming a good response function is known for all γ-ray energies, the different peaks are identified as; The full energy (f), single escape (s), double escape (d), and the annihilation (a). The full Compton contribution is added in (c). The probabilities are normalised, so that

$$p_f + p_c + p_s + p_d + p_a = 1. \tag{4.1}$$

The unfolding itself uses the response in the detector, R_{ij}, which is the response in channel i from a γ-ray with an initial energy of j. With every response function normalised to $\sum_i R_{ij}$ = 1, the folded(f) spectra can then be described as

$$f = \mathbf{R}u \tag{4.2}$$

where $\mathbf{R}$ is the response matrix and u is the true, incoming spectrum. Here, f and u are vectors of length i, and $\mathbf{R}$ the full response matrix of size i x j. The iteration begins with a trial function $u^0 = r$, where r is the observed spectrum as an arbitrary, and obviously wrong, guess of the unfolded spectrum.

$$u^0 = r. \tag{4.3}$$

Then, the folded version of this spectra is calculated:

$$f^0 = \mathbf{R}u^0, \tag{4.4}$$

and the next trial function found by adding the difference of the spectrum from the first trial

$$u^1 = u^0 + (r - f^0) \tag{4.5}$$

By another folding we get another new f^1 which is again used to find a new trial function

$$u^2 = u^1 + (r - f^1). \tag{4.6}$$

Whenever $f^k \approx r$ in iteration k, the first estimate of the unfolded spectrum u^k is obtained.

This spectrum is now the input for the Compton subtraction. The full description can be found in [35]. The main idea is to define a new spectrum of all the full energy contributions as well as the single-, double escape and annihilation. This spectrum uses the normalized probabilities of eq. 4.1 and the unfolded spectrum u^k to generate a new spectrum v:

$$v = u_f(i) + u_s(i - i_{511}) + u_d(i - i_{1022}) + u_a(i_{511keV}) \tag{4.7}$$

with appropriate smoothing relative to the FWHM of the experiment. The Compton background is then the only contribution not accounted for in v and the Compton spectrum can be calculated as

$$c(i) = r(i) - v(i) \tag{4.8}$$

which is then smoothed, and the final unfolded U can be calculated after correcting for the energy dependent detector efficiency.

4.3 Extracting the first generation γ spectra

As decay from an excitation level E_x may feature cascades of many γ-rays, we need a way of isolating the γs that are uniquely from this excitation energy, and therefore the first decays in the cascades. Due to the Brink hypothesis and assuming the levels that decay are of compound nature, this means that an exited nucleus of excitation energy E_x will have the same properties independent on whether it's a result of a de-excitation from a higher E_x or if it's been directly excited via the reaction. This means that in any excitation energy bin E_x the γs from the lower bins can be subtracted to obtain the first γ-rays emitted from E_x. These first γs from any E_x are called the first generation γs and is the foundation for the further analysis.

For any excitation energy bin i, the unfolded spectrum f_i is therefore the sum of the primary γ-ray spectra h_i and all further γs in the cascades g_i. If we can then find g_i, we can find the primary γ-ray spectra by:

$$h_i = f_i - g_i. \tag{4.9}$$

Here, g_i contains all γ-rays from lower energy bins, $f_{j<i}$, and therefore all γ rays except the primary γs from bin i. g_i is calculated using a weighted sum of all lower spectra

$$g_i = n_{i1}w_{i1}f_1 + n_{i2}w_{i2}f_2 + ... + n_{ij}w_{ij}f_j = \sum_j n_{ij}w_{ij}f_j \tag{4.10}$$

where all weights w are normalised to

$$\sum_j w_{ij} = 1.$$

This weight works as a branching ratio, denoting the probability of decay from state i to j, which means the weighting function will directly correspond to the first generation spectrum. n is defined so that the number of cascades is preserved in each f_i. To find this a normalisation needs to be done, which can be done either using singles spectra or γ-ray multiplicities, of which we use the latter. First, the average γ-ray multiplicity can be defined as the total energy carried by the γ-rays divided by the average γ energy

$$< M >= \frac{E}{< E_\gamma >} \tag{4.11}$$

and can then be calulated for each excitation energy bin i. Defining the total amount of counts in f_i as $A(f_i)$, the singles particle cross section should be proportional to $A(f_i)/ < M_i >$, i.e. the total number divided by the average multiplicity in excitation energy bin i. n is then calculated as the relation between energy bin i and j as

$$n_{ij} = \frac{A(f_i)/ < M_i >}{A(f_i)/ < M_i >} = \frac{< M_j > A(f_i)}{< M_i > A(f_i)} \tag{4.12}$$

To obtain the first generation (primary) γ-rays, an iterative subtraction method is used. By normalizing all γ spectra to unity and then subtracting all underlying weighted spectra from the lower E_x bins, the γ-rays are extracted for all excitation energy bins.

4.4 Extracting the γSF and NLD from the first generation γ matrix

A new method of extracting the γSF and the NLD from the first generation γ spectra presented by A. Schiller et al. [28] is the basis for the rhosigchi program of the Oslo method.

As the probability for a level in an initial excitation energy bin E_i to decay to a final excitation energy bin E_f is dependent upon the number of available levels in E_f, the first generation γs decaying to E_f will give information on $\rho(E_f)$. The transition energy is given by

$$E_\gamma = E_i - E_f. \tag{4.13}$$

Normalize each first generation spectrum for all excitation energy bins E_x to unity as

$$\sum_{E_\gamma=E_\gamma^{min}}^{E_\gamma=E_x} P(E_x, E_\gamma) = 1. \tag{4.14}$$

Then, the decay probability of a γ-ray from energy E_i to E_f is proportional to the level density $\rho(E_f)$ and the γ-energy dependent transmission coefficient $\tau(E_\gamma)$. Note how the transmission coefficient is only dependent on the γ energy E_γ, which assumes the Brink hypothesis, and enables the factorisation of the first generation (primary) γ-ray matrix as

$$P(E_i, E\gamma) \propto \rho(E_i - E_\gamma)\tau(E_\gamma) = \rho(E_f)\tau(E_\gamma). \tag{4.15}$$

There is also an assumption that the decay is from compound states. This mean that the probabilities of the decay of any state is independent on its creation, which is believed to be a good assumption for sufficienty high E_x.

The functions ρ and τ are found by an iterative procedure which adjusts the points of these two functions until an optimal χ^2 is found with respect to the experimental P(E_i,E_γ). This solution is uniquely determined from data, save for some normalization constants for which there is an infinite number of solutions. Neither the absolute values, nor the slope of the solutions are known, but this is solved by normalizing the result to external data.

In [28] it has been shown that any solution on the form

$$\tilde{\rho}(E_i - E_\gamma) = A \exp\Big(\alpha(E_i - E_\gamma)\Big)\rho(E_i - E\gamma), \tag{4.16}$$

and

$$\tilde{\tau}(E_\gamma) = B \exp(\alpha E_\gamma)\tau(E_\gamma) \tag{4.17}$$

are valid and give identical fits to the first generation matrix $P(E_i - E_\gamma)$. The parameters α, A and B should therefore be found by normalizing to auxiliary data.

By assuming every data point of ρ and τ as N_{free} number of independent variables, the main idea is to minimize a χ^2 as:

$$\chi^2 = \frac{1}{N_{free}} \sum_{E_i=E_i^{min}}^{E_i^{max}} \sum_{E_\gamma=E_\gamma^{max}}^{E_i} \left(\frac{P_{th}(E_i, E_\gamma) - P(E_i, E_\gamma)}{\Delta P(E_i, E_\gamma)} \right), \tag{4.18}$$

where $\Delta P(E_i, E_\gamma)$ is the uncertainty in the primary γ matrix.

4.5 Normalizing the NLD

The NLD is normalized to the semi-experimental $\rho(S_n)$ and the experimentally known levels at low excitation energy. To calculate $\rho(S_n)$, we use the ground state spin I_t of the target nucleus in a neutron resonance experiment, i.e. the N-1 nucleus compared to the one we are studying. The average neutron spacing for s-wave neutrons, which will have all levels with spin $J = I_t \pm 1/2$ available as

$$\frac{1}{D_0} = \frac{1}{2}\Big(\rho(S_n, J = I_t + 1/2) + \rho(S_n, J = I_t - 1/2\Big) \tag{4.19}$$

if we assume both parities contribute equally at the high excitation energy $E_x = S_n$. Using eq. (4) and (5) from [36], we find

$$\rho(U, J) = \frac{\sqrt{\pi}}{12} \frac{\exp(2\sqrt{aU})}{a^{1/4}U^{5/4}} \frac{(2J+1)\exp[-(J+1/2)^2/2\sigma]}{2\sqrt{2\pi}\sigma} \tag{4.20}$$

and

$$\rho(U) = \frac{\sqrt{\pi}}{12} \frac{\exp[2\sqrt{aU}]}{a^{1/4}U^{5/4}} \frac{1}{\sqrt{2\pi}\sigma}, \tag{4.21}$$

together with eq. 4.19, we can calculate $\rho(S_n)$. The parameter input is fetched from [37] to calculate and find the level-density parameter a and the spin cutoff parameter σ, as well as the intrinsic excitation energy U The upper normalisation point is calculated by:

$$\rho(S_n) = \frac{2\sigma^2}{D_0} \cdot \frac{1}{(I_t)\exp[-(I_t+1)^2/2\sigma^2] + I_t \exp[-I_t^2/2\sigma^2]} \tag{4.22}$$

The normalization of the NLD is done to this estimated $\rho(S_n)$ and the known levels. The low-lying levels are obtained from NNDC[25] and binned to fit the data binning size. This fit determines the parameters A and α of eq. 4.16.

4.6 Normalizing the γSF

Since the transmission coefficient τ and the γSF is connected as

$$f_{XL}(E_\gamma) = \frac{1}{2\pi}\frac{\tau_{XL}(E_\gamma)}{E_\gamma^{(2L+1)}}, \tag{4.23}$$

where X is the electromagnetic character and L the multipolarity.

The normalization of the γSF is partially described by the α which decribes the slope and was found from normalizing the NLD. The last parameter B, from eq. 4.16 is not yet determined. This is determined from the average total radiative width $< \Gamma_\gamma >$ at the neutron binding energy B_n, as described in [38].

We assume dominance of dipole transitions, so that the experimental γ-ray transmission coefficient reads

$$\tau_{exp} \approx \tau_{E1} + \tau_{M1}. \tag{4.24}$$

If I_t and Π are the spin and parity of the target nuclceus t, i.e. N-1, and ρ is the level density, the normalization parameter can be calculated by

$$\begin{aligned} < \Gamma_{\gamma 0}(B_n, I_t \pm 1/2, \Pi_t) > = \frac{1}{2\rho(B_n, I_t \pm 1/2, \Pi_t)} \int_{E_\gamma=0}^{B_n} dE\gamma \; B \; f(E_\gamma)\, \rho(B_n - E_\gamma) \\ \times \sum_{J=-1}^{1} g(B_n - E_\gamma, I_t \pm 1/2 + J). \end{aligned} \tag{4.25}$$

where g is the spin distribution of the level density, defined as

$$g(E, I) = \frac{2I+1}{2\sigma^2}\exp[-\frac{(I+1/2)^2}{2\sigma^2}, \tag{4.26}$$

where σ is the spin cut-off parameter, and the spin distribution is normalized to 1 by $\sum_I g \approx 1$.

Chapter 5

Data analysis

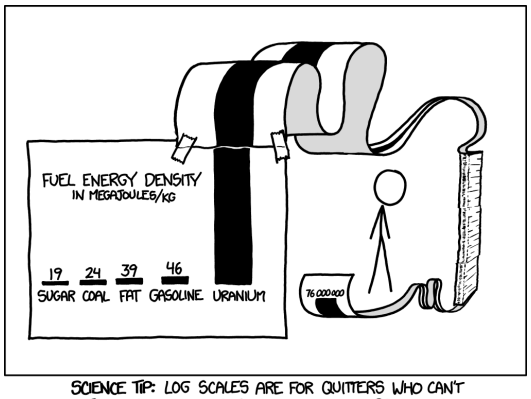

-xkcd, https://xkcd.com/1162/

In this section I will describe and go through the analysis of the raw matrices obtained from the experiment. By using the Oslo method software[1] and analysis, we can obtain the gSF and NLD of both ^{187}Re and ^{188}Re. I will also give a brief overview of the Oslo method software and focus on how to run to reproduce the analysis. All input files and parameters are documented on the github[27] under the folders `mama_d` and `mama_t`.

5.1 Oslo method software structure

The Oslo method software was developed in a period from the late 80s to around year 2000 and has been continuously updated ever since. It is is a collection of smaller software pieces which are run with a command line interface. When run for the first time in a folder, all values will be a default which will need to be changed, but they will save your input in text files for your next run. It does require ROOT to be available for plotting. This is a short introduction to the components of the Oslo method software, and the version used in the analysis is the [39].

For more recent, thorough analysis of the method, please see [30]. This paper by Larsen et. al. also contains a well-written synthetic example of the first-generation method in a clear and precise way, friendly both to people without a lot of prior familiarity to the analysis and seasoned individuals who wants further understanding.

The whole Oslo method analysis has recently also been completely redesigned to run in python 3.8+ as ompy [40] with an improved, rigorous statistical uncertainty propagation.

[1] https://github.com/oslocyclotronlab/oslo-method-software

Nucleus	D_0 [eV]	$< \Gamma_0 > [meV]$
^{187}Re	2.26 ± 0.23	$92.5^* \pm 10$
^{188}Re	3.61 ± 0.13	57 ± 3

Table 5.1: Input values for the Oslo method analysis. D_0 and $< \Gamma_0 >$ are both from Mughabghab[41] for the N-1 nuclei, which is already accounted for. $\sigma(S_n)$ is calculated from Robins rigid body model(RMI). *This is the value given in Mughabghab. From systematics and evaluating the results (see the text), the value for ^{188}Re was used instead, but the original value is evaluated later in the results chapter.

Please note that some inputs in the routine are non-essential. They are simply for calculating the initial condition of an iteration and will contribute to the iteration converging easier. Tests have been done where these inputs were arbitrary, still arriving at the same final answer.

The Oslo method software includes the following:

mama, short hand for MAtrix MAnipulation, is the first program to run which takes the raw matrix as input. With this code, the unfolding in performed and has different response matrices for different experimental setups. This changes the spectra back to the actual spectra of γ-rays to then extract the first generation γ rays. This is also a way to easily plot the matrices, compress the axes and inspect bins to do sensible cuts in the data later.

rhosigchi is designed to extract the level density (ρ) and γSF (σ) from the first generation γ spectra made in mama. This is done by assuming $FG_{norm}(E_x, E_\gamma) = \rho(E_x - E_\gamma) * \tau(E_\gamma)$ which follows from the compound nuclear decay and equations outlined in chapter 4 and the Brink hypothesis outlined in chapter 2.5

robin is software to calculate level densities and the spin cut-off parameters at $\rho(B_n)$ for a given nucleus. This is a program mainly to find appropriate parameters from different models and generate input files to add into the analysis itself. It has four spin cut-off formulas built in, whereas the rigid moment of inertia, constant temperature and Fermi gas formula are used in this analysis. This uses models by Egidy and Bucurescu[2].

d2rho calculates level density from the level spacing, D, at a specific binding energy, here the neutron binding B_n, formed by $l = 0$ neutrons. This is based on neutron.f by Andreas Schiller, and is needed to do the normalization of the nuclear level density, as it is normalized to $\rho(B_n)$ later.

counting normalizes and generates, among other files, counting.cpp (level density), spincut.cpp (spin cutoff σ) and sigext.cpp (γ ray transmission coefficient). The level density is normalized to known levels, given in a file called counting.dat which must be manually made, and resonance spacing data at B_n. Intervals of data points to use in these normalizations must also be chosen here, so it's a good idea to manually evaluate the final plots and datapoints properly.

normalization does what the name might suggest, and normalizes the γSF ($f(E)$) to the total average radiation width measured at B_n. This is based on normalization.f by Andreas Schiller, and needs several files as input from the other programs. It produces strength.cpp which is used for plotting the γSF.

Both counting and normalization generates .cpp files that can be run with ROOT as, for example,

```
$ root strength.cpp
```

plotting the results. The .cpp files can then be altered with fitting titles and other explanations at a later stage.

[2]E&B2009 from PRC 80, 054310 (2009) and E&B2006 from PRC 72, 044311 (2005) and PRC 73, 049901 (E) (2006). See the oslomethod software documentation for a further elaboration.

Nucleus	$\sigma(S_n)_{100\%}$	$\sigma(S_n)_{90\%}$	$\sigma(S_n)_{80\%}$	$\sigma(S_n)_{70\%}$	$\sigma(S_n)_{60\%}$
^{187}Re	7.685	7.291	6.874	6.430	5.953
^{188}Re	7.519	7.133	6.725	6.291	5.824

Table 5.2: Input values for $\sigma(S_n)$ calculated from Robins rigid body model(RMI). The uncertainty of this $\sigma(S_n)$ value is not calculated directly, but to estimate parameter uncertainty, the reduction factor is varied from 100% to 60% of the full RMI.

5.2 Finding initial values before running.

As an initial input, we need the raw matrices. There are also other important input parameters, such as the neutron and proton numbers, as well as the neutron binding energy and spin/parity of the ground states. For counting, we also need a file with all known experimental levels for the normalization of the NLD which needs to be named counting.dat. All values are fetched from the NNDC database[25] and are saved in the folders where the analysis is performed.

For the spin-cutoff we use a model further described in [42] nick named "Alex" which requires an average of experimental spins and energies of low energy states. For ^{188}Re we average the levels from the g.s. up to, and including, the level at 353 keV. Averaging energies and spin (ignoring parity) gives us $\bar{E} = 233$ keV and average spin cutoff $\bar{\sigma} = 2.78$. For ^{187}Re we used the states from 303 keV to 647 keV. Some of the states does not have confirmed spin/parity, but using the suggested values in parenthesis should be sufficient. This gives us $\bar{E} = 538$keV and $\bar{\sigma} = 3.1$.

From Mughabghab[41] we obtain the neutron resonance spacing parameter D_0 as well as the average total radiative resonance width $< \Gamma_0 >$ for the final normalizations of the results. These values must be for the $Z = Z, N - 1$ nuclei compared to the one we are analyzing for, since in a neutron capture reaction, the $N - 1$ would be the target nucleus. I.e. for the (α,d) producing ^{188}Re, I must use the values from ^{187}Re, and the values for ^{187}Re we use the values from ^{186}Re. The applied values are given in table 5.1.

For the $< \Gamma_0 >$-value of ^{187}Re from ^{186}Re(n,γ), the value given in Mughabghab seem higher than expected from systematics from the neighbouring nuclei. In Kullman et al. [43], a thorough review is done of the values given in the 2006 edition of Mughabghab[44] and RIPL-3[45] for the same mass area as this thesis. In fig. 6 of [43], both ^{186}Re and ^{188}Re have given values, from both sources, at around $< \Gamma_0 > \approx 60$ meV. For A= 187, no value is given for Re, but the estimate from Mughabghab for W is close to 50 and estimates for ^{187}Os is given with three different values from 50 to 75 meV. From this systematics, we have chosen to use the $< \Gamma_0 > = 57$ meV for both nuclei, though the original suggested value from Mughabghab of 92.5 meV is commented on in the discussion later.

The values of $\sigma(S_n)$ is calculated with the code Robin with the rigid body of inertia (RMI) model in table 5.2. As reduction factor 1.0 of RMI would give the full RMI and a theoretical maximum. A factor 0.6 of RMI can be viewed as the ground-state estimate. I used 0.8 in the results and 0.8 ± 0.1 and 0.8 ± 0.2 in the systematic uncertainties later in the results.

5.3 Running the Oslo method software for $^{186}\mathbf{W}(\alpha, d)$

I will focus on the (α,d) analysis, as the analysis for (α,t) is very similar, and I will outline the differences in the next section. I will go through the different steps of the analysis, and all the input files and results are located in the github[27]-folder `mama_d`. Note that this is specifically for this dataset. Firstly, we need the raw matrix in the correct format, which can be obtained

by saving it directly from the sorting batchfile by the command “save alfna”. This will produce the raw input matrix of the correct format to read into mama.

5.3.1 MAMA: unfolding the raw matrix

First, we must run mama (MAtrix MAnipulation), read the matrix and plot it. Triple dots represent removed text. Where nothing else is stated, assume no change in input. The command ds2 is used for plotting in the interactive window and wr is used to save the matrix whenever you need to.

```
1  $ mama
2  ...
3  mama>re
4  Destination spectrum <1>:
5  Filename          <TEST>:alfna
6   FILE=Disk
7   KIND=Matrix
8   LABORATORY=Oslo Cyclotron Laboratory (OCL)
9   EXPERIMENT=Sirius
10  COMMENT=E(NaI) : E_{x}
11  TIME=16-Oct-20 10:51:56
12  CALIBRATION EkeV=6, 0.000000E+00, 7.000000E+00, 0.000000E+00,-5.000000E+02,
       3.100000E+01, 0.000000E+00
13  PRECISION=16
14  DIMENSION=2,0:1999,0: 499
15  CHANNEL=(0:1999,0: 499)
16 ..........
```

The command re is used to read the matrix alfna. There is also information here on the calibration, so out of the six values (not counting the first which gives the number of values) given in line 12 above, the bin widths are 7 keV and 31 keV.

We then want to fill in the negative counts. This is not essential, but the first step of fn adds a slight smoothing to all negative counts, replacing them with surrounding values. This is useful as we do not expect big changes in neighbouring bins. The rn command used afterwards forces the remaining negative values to zero. This also ensure that the unfolding doesn't suddenly introduce very large negative numbers where they have no physical reason to be so.

```
1  mama>fn
2  ...
3  Dimension along x-axis <2000>:
4  Dimension along y-axis < 500>:
5  ...
6  Before number of neg. ch. was:  57994, with total counts:    -91263
7  After  number of neg. ch. is:    1436, with total counts:     -1492
8  mama>rn
9  ...
10 Give new value for the counts to be replaced <  0.00>:
11 Delete counts with value lower than          <  0.00>:
12
13 Number of channels replaced:          1436
14 Number of counts before:          212745.0
15 Number of counts after:           214237.0
16 Increase of counts:                 1492.0
17 mama>ds2
```

The raw matrix can be seen in fig. 5.1. After this you must specify the response matrix, rm. This is to do the unfolding as different setups and different geometries will respond differently to the same signals. For this dataset, response function (3) of NaI_2012 is the correct one.

```
1  mama>rm
2  ...
3   List of response functions. The ones marked old, are not recommended
4    (0) Gaussian
5    (1) NaI_old         CACTUS 5x5 inch before 2012
6    (2) LaBr_2012       Campaign 4x8 inch LaBr from Milano in CACTUS frame
7    (3) NaI_2012        CACTUS 5x5 inch after 2012
```

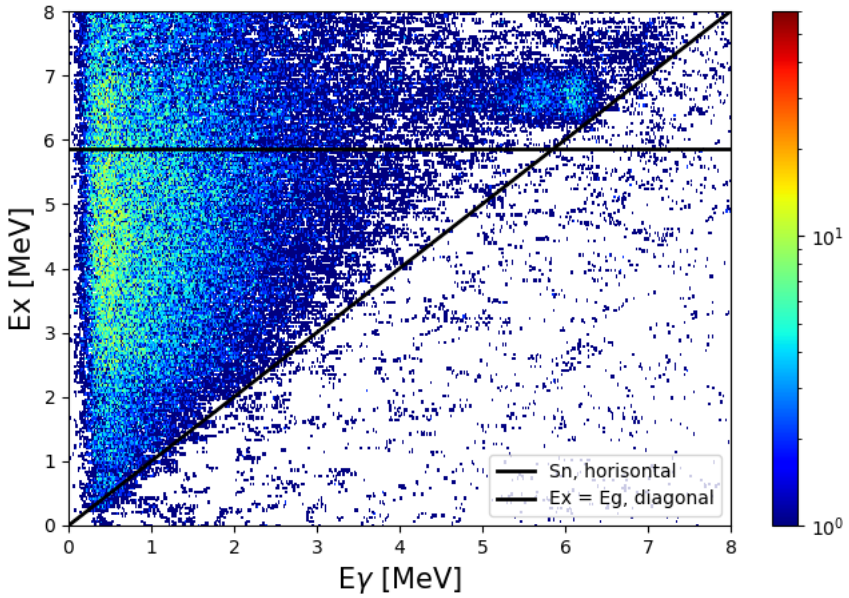

Figure 5.1: The raw alfna (α,d) matrix after removal of negative counts. Bin sizes are 7.0 keV/channel on the x-axis, and 31.0 keV/channel on the y-axis.

```
  (4) Seg2             SuN at MSU 2014, with target inside  (2 cm?), GEANT4
  (5) Seg3             SuN at MSU 2014, with target outside (2 cm?), GEANT4
  (6) Clover_old       Notre Dame 2015, GEANT4
  (7) Clover           Notre Dame 2015, GEANT4
  (8) Seg23            SuN at MSU 2015 with target in center, GEANT4
  (9) Oscar2017        [For comparison] "Old" OSCAR at OCL 2017 with 15 LaBr,
    GEANT4
 (10) Afrodite_Clover  iThemba 2015, 8 Clover, GEANT4 (2018)
 (11) Afrodite_LaBr    iThemba 2015, 2 LaBr, GEANT4 (2018)
 (12) Gretina2018      MSU, GEANT4 one quad, Remco and Lew
  or:
 (13) Read from disk: # OSCAR 2017 LaBr; SCALED compton by 1.15

Choose your response function <13>:3
...
Give relative energy resolution at Egam=1.33 MeV (FWHM/Egam) (%) < 6.770>:
...
 Parameters for response function written to respout.dat
mama>cr
Type X or click on green button to exit
x=   96, energy =    672.000 keV
y=   22, energy =    182.000 keV
...
x=  966, energy =   6762.000 keV
y=  220, energy =   6320.000 keV
...
```

After selecting the correct response matrix and loading that, I needed to make a cut to unfold only where there is data. The actual channels I chose to cut are $x \in [96, 966]$ and $y \in [22, 220]$. This is added in the unfolding itself.

The next step is the actual unfolding. It is important that this unfolding is able to converge. The folding routine will choose the iteration with the best resulting spectrum. Then, setting the number of iterations to the maximum 499 and adding the limits for the interpolations:

```
mama>un
Destination spectrum <2>:
```

```
Source spectrum      <1>:

New (0) or old (1) unfolding procedure <0>:

Dimension along x-axis <2000>:
Dimension along y-axis < 500>:
...
First point x1  < 1999>:96
First point y1  <    0>:22
Second point x2 < 1999>:966
Second point y2 <  499>:220
  Give limits for the chisquare-test:
  Opt. 1: Recommended for LaBr- and NaI-spectra. For full-
          energy gammas above 2 MeV, we set lower limit at 500 keV.
           Below, the limit is 1/4 of the full-energy. Remember,
          full-energy is taken from the upper unfolding limit
  Opt. 2: A fixed lower limit for the chi-test is applied
  Opt. 3: Return and set proper upper limits for unfolding


Option (1/2/3)                  <1>:

Include total detector efficiency (y/n) <y>:
...
Do you want to change the discriminator threshold <n>:

Number of iterations ( <500 )  <100>:499
...
Weight on fluctuations <0.2>:
...
 Row: 498  Mode: n  Area:        0(        0)  Chi:   0.00  Fluct:  1.00
 Row: 499  Mode: n  Area:        0(        0)  Chi:   0.00  Fluct:  1.00
Calibration is a0=   0.0keV, a1=   7.00keV/ch
```

The weight on experimental fluctuations serves as a regularisation on the unfolding. Then, remove the negative counts again and save the unfolded matrix with wr.

```
mama>fn
...
Before number of neg. ch. was: 160519, with total counts:   -198523
After  number of neg. ch. is:   17246, with total counts:     -9204
mama>rn
...
Number of channels replaced:         17246
Number of counts before:           224020.8
Number of counts after:            233212.8
Increase of counts:                  9192.1
mama>ds2
mama>wr
...
Filename                        <TEST>:alfna_un_fnrn
```

The unfolded matrix is shown in fig. 5.2.

5.3.2 MAMA: extracting first generation γs

Extracting the first generation γs from the unfolded spectra is done with the command fg in mama. This part of the routine is also an iterative method.

```
mama>fg
...
Calibration for gamma-energies:
Cal. coeff. a0 (keV) on x-axis   <     0.0>:
Cal. coeff. a1 (keV/ch) on x-axis<     7.0>:

Calibration for excitation energies:
Cal. coeff. a0 (keV) on y-axis   <  -500.0>:
Cal. coeff. a1 (keV/ch) on y-axis<    31.0>:

```

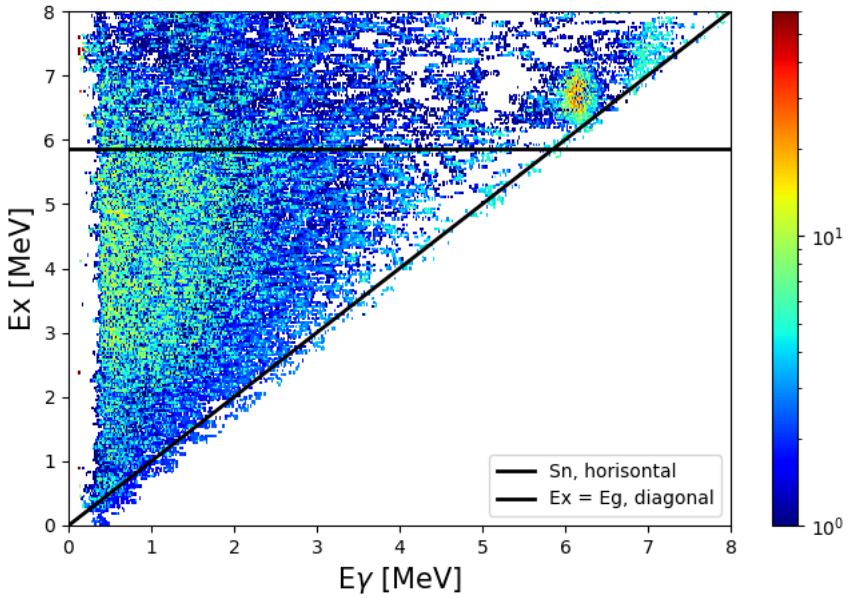

Figure 5.2: The (α,d) unfolded spectra after subtracting the negative counts. Bin sizes are 7.0 keV/channel on the x-axis, and 31.0 keV/channel on the y-axis.

```
Excitation energy of highest gate (keV)  <  9048.0>:
```

These values are picked up from the unfolded matrix itself.

```
Normalization: singles(1) or multiplicity(2)     <2>:
Multiplicity:  statistical(1) or total(2)        <1>:
Area correction for 1. gen. spectra (y/n)        <y>:
Experimental lower gamma thresholds (keV)  <  300.>:
Upper threshold for nonstat. gammas (keV)  <  300.>:
Average entry point in ground band (keV)   <    0.>:
```

We choose the multiplicity normalization, as we do not have information to pick out singles, and using the statistical is simpler. The experimental lower γ threshold was chosen both from limitations of the electronics, but also from looking at the unfolded spectra in fig. 5.2, where the γ spectra look more complete from 300keV and above. Since there are no isomers present and there are many excited states at low E_x, decaying to g.s. should be no problem.

```
...
Give ratio R           (no sliding = 100.) <  0.30>:
...
Assumes Fermi gas distribution
Level density parameter a (1/MeV)           <17.44>:
Exponent n for Eg**n                        < 4.20>:
```

The Fermi gas distribution parameters a and n are found from Robin. Then, use the multiplicity suggested for all the channels and press enter through. After this, the first generation iteration can be looped. I looped around 20 times,

```
 Multiplicity in each gate:
 ----------------------------------
 Y-ch=  38 Ex=  9032.5 keV < 3.143>:
...
Y-ch=  22  Ex=    182.  Area=        15.0  Alpha=   1.00  dA/A(%)=     0.00
Y-ch=  21  Ex=    151.  Area=         3.4  Alpha=   1.00  dA/A(%)=     0.00
Y-ch=  20  Ex=    120.  Area=         5.7  Alpha=   1.00  dA/A(%)=     0.00
Y-ch=  19  Ex=     89.  Area=        28.2  Alpha=   1.00  dA/A(%)=     0.00
Y-ch=  18  Ex=     58.  Area=        27.7  Alpha=   1.00  dA/A(%)=     0.00
```

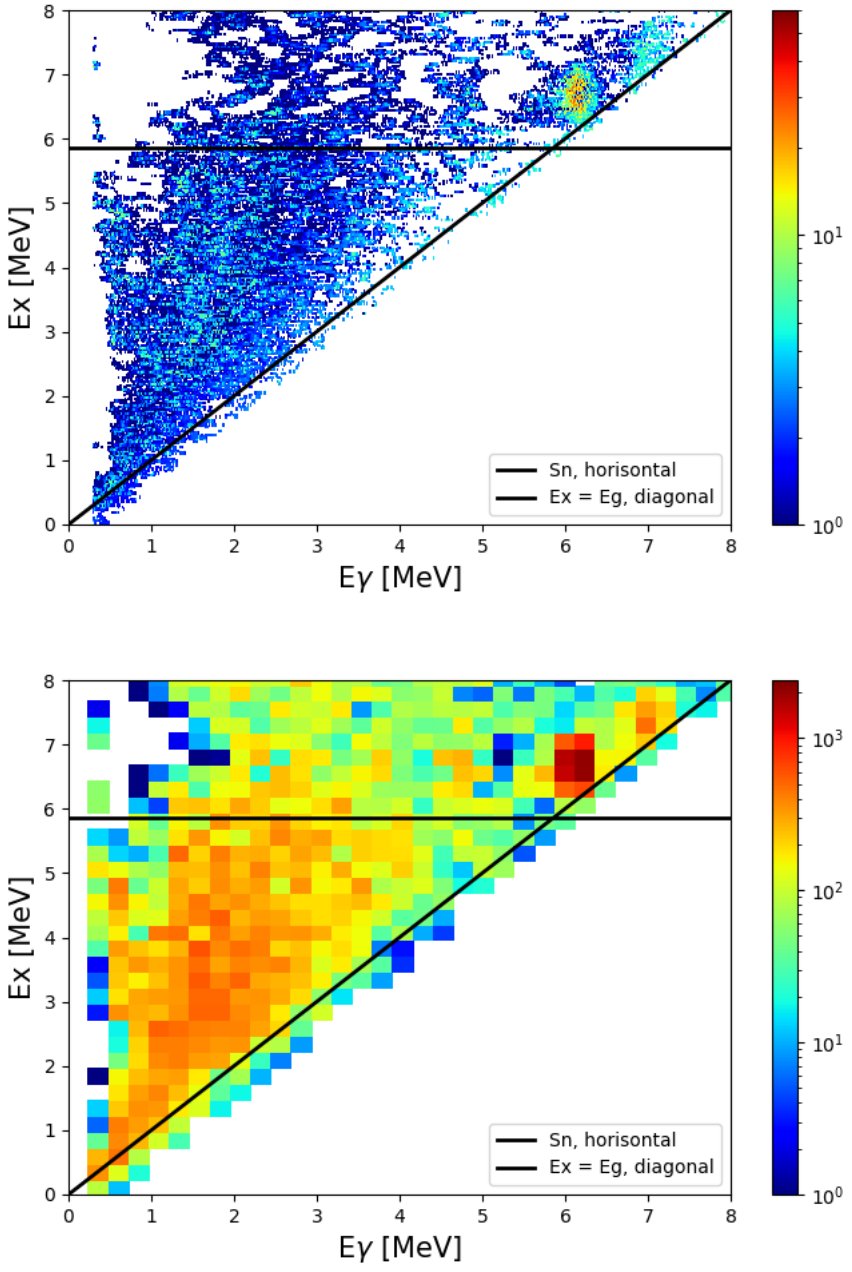

Figure 5.3: The first generation matrix of (α,d) both with the original bin size of 7.0keV/channel and 31.0keV/channel, as well as the matrix compressed by a factor of 35 on the x-axis and 8 on the y-axis to 245.0keV/channel and 248.0keV/channel, ready for further use in the analysis. The bins are plotted centered on their values. Here, we can also see how the oxygen peak above 6 MeV is also above the neutron separation energy, and does not interfere with the γ spectra of ^{188}Re.

```
Y-ch=  17  Ex=     27.  Area=        19.6  Alpha=   1.00  dA/A(%)=     0.00
Y-ch=  16  Ex=     -4.  Area=         0.0  Alpha=   1.00  dA/A(%)=  9999.99
-----------------------------------------------

Iteration loop = 20, stop(0), activate/modify direct decay(1) or continue(2)
    <2>:0
Last iteration 20 stored in matrix 1
Additional results written to figegaout.dat
```

The dA/A is the change in area of the first generation from one iteration to the next. Having it converge to 0 shows that the first generation iteration has converged, which is a good sign. The large values of dA/A > 9000 is a divide-by-zero kind of result, and is expected. Then, as before removing the negative counts with fn and rn.

```
mama>fn
...
Before number of neg. ch. was: 110698, with total counts:    -74576
After  number of neg. ch. is:   15894, with total counts:    -13096
mama>rn
...
Number of channels replaced:         15894
Number of counts before:           87586.7
Number of counts after:           100682.9
Increase of counts:                13096.2
mama>ds2
.
mama>wr
...
Cal. coeff. a0 (keV) on x-axis     <        0.0>:
Cal. coeff. a1 (keV/ch) on x-axis  <      7.000>:
...
Cal. coeff. a0 (keV) on y-axis     <     -500.0>:
Cal. coeff. a1 (keV/ch) on y-axis  <     31.000>:
...
Filename                        <TEST>:alfna_fg
```

The first generation matrix after removing negative counts in fig. 5.3 is the final result so far. To show how the spectra changes from the raw to unfolded and finally the first generation, a projected comparison of $E_x \in [4, 5]$ MeV is plotted in fig 5.4.

After saving this matrix with wr, it is now important to have dimensions of maximum 500×500 since that is the most the code extracting the NLD and γSF can handle. As the statistics is low, we compress the bin widths to ≈ 250 keV to get more counts in each pixel.

```
mama>co
...
Compression along x-axis <  1>:35
Compression along y-axis <  1>:8
...
New dimension (0:  56,0:  61)
mama>wr
Cal. coeff. a0 (keV) on x-axis     <      119.0>:
Cal. coeff. a1 (keV/ch) on x-axis  <    245.000>:
...
Cal. coeff. a0 (keV) on y-axis     <     -391.5>:
Cal. coeff. a1 (keV/ch) on y-axis  <    248.000>:
...
Dimension on x-axis (max=4096) <  57>:
Dimension on y-axis (max=2048)  <  62>:
Filename                        <TEST>:alfna_fg_cofinal
```

5.3.3 Robin and spin-cutoff parameters.

Robin is a code for calculating parameters for a given nucleus based on different models. No matter which model you want to use, the initial part is always similar. You are asked for the proton and mass number, and presented with the different model options.

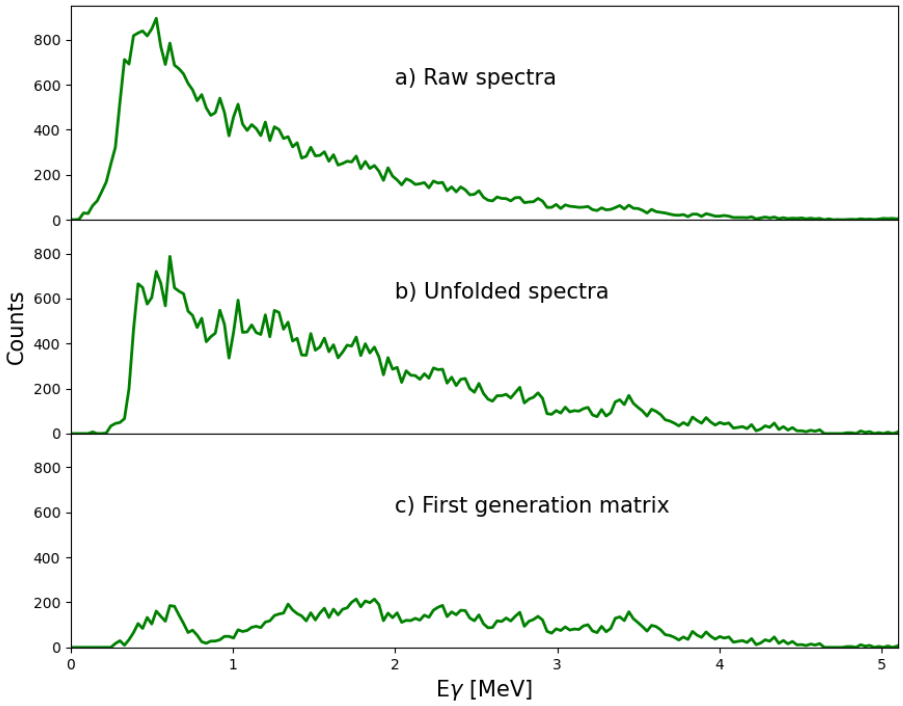

Figure 5.4: Projections of the γ count of $E_x \in [4, 5]$ MeV from the $(\alpha, d\gamma)$ matrices, a) fig. 5.1, b) fig. 5.2 and c) fig. 5.3a). The projections are rebinned with a factor 4 compared to the initial matrices on the x-axis to suppress random fluctuations, so the x-axis bin sizes are 28keV/channel.

```
$ robin
...
Give proton number of the nucleus < 75>:
Give mass number of the nucleus   <188>:
...
You may choose between 4 spin cut-off formulas:
 1 The rigid moment of inertia formula (RMI)(E&B2006)
 2 The Gilbert and Cameron formula (G&C) Can. J. Phys 43(1965) 1446
 3 The constant temperature (CT) formula (E&B2009) and NPA 481 (1988) 189
 4 The Fermi gas formula with appropriate cut-off parameter (E&B2009)
 Type 1 for RMI: sig**2=0.0146*(A**(5/3))*T for FG (E&B2006)
 Type 2 for G&C: sig**2=0.0888*(A**(2/3))*a*T for FG
 Type 3 for E&B: sig**2=(0.98*(A**(0.29)))**2 for CT
 Type 4 for E&B: sig**2=0.391*A**0.675*(E-0.5*Pa_prime)**0.312 for FG
Choose RMI(FG) (1), G&C(FG) (2), E&B(CT) (3) or E&B(FG) (4)  <4>:
```

Choosing number 1, the rigid moment of inertia will give you another choice between the "common fermigas formula" and the "somewhat more advanced fermigas formula", of which we choose the latter.

```
You may choose between 2 temperature formulas:
 1 The common fermigas formula (CFG)
 2 The somewhat more advanced fermigas formula (AFG) (E&B2006)
 Type 1 for CFG: T = SQRT(U/a) (G&C)
 Type 2 for AFG: T = (1+SQRT(1+4*a*U))/(2*a)(E&B2006)
Choose CFG (1) or AFG (2)           <2>:

 You may choose a reduction factor of RMI at Sn
```

```
 Typically, 0.8-1.0 is an appropriate reduction factor
Give reduction factor of RMI <1.00>:0.8
 You may choose another a and/or E1 than proposed by E&B2009:
Level density parameter a    < 19.271>:
Total backshift parameter E1 < -1.093>:
```

This reduction factor of the RMI is what gives the different values of $\sigma(S_n)$ (called sig_n) of table 5.2. All the output values are then given, where the Fermi gas parameter a, and the level densities at S_n is given as rho_n.

```
Results for 188Re with sig**2=0.0146*(A**(5/3))*(1+SQRT(1+4*a*U))/(2*a):
Shell values            : S=     -0.744 MeV,   dS/dA= -0.196 MeV
Pairing energies        : P_n=    0.662 MeV,   P_p=    0.761 MeV, P_d=  -1.592
    MeV, Pa_prime=  -1.592 MeV
Binding energies        : B_n=    5.872 MeV,   B_p=    6.400 MeV
Fermi gas parameters    : a=     19.271 1/MeV, E1=    -1.093 MeV
Spin cut-off parameters : sig_n=  6.725        sig_p=  6.844
Level densities         : rho_n= 0.42699E+07 1/MeV, rho_p= 0.90781E+07 1/MeV
Temperature (FG)        : T(Bn)= 0.62766E+00 MeV,   T(Bp)= 0.65003E+00 MeV
Calculate rho and sigma at Ex (MeV)  <  5.872>:
For Ex =  5.872 MeV     : rho  = 0.42699E+07 1/MeV, sig =  6.725
Write file with spin distribution for spin cut-off sig = <  4.474>:

File spindis.rbn written with <I> = 5.10, Pmax @ I = sigma-0.5 = 4.0 and sum_P
    =1.002
```

All output is then written to file.

The second formula of Gilbert and Cameron is not used in this analysis, but if you choose the third of constant temperature formula, you see a suggested T and $E0$. Here I specified $T = 0.545$ MeV.

```
 You may choose another T and/or E0 than proposed by CT(E&B):
Constant temperature T(MeV)  <  0.538>:0.545
Total backshift parameter E0 < -1.800>:
```

This then calculates new values for this nuclear temperature.

```
Results for 188Re with sig**2=(0.98*(A**(0.29)))**2.:
Shell values            : S=     -0.744 MeV,   dS/dA= -0.196 MeV
Pairing energies        : P_n=    0.662 MeV,   P_p=    0.761 MeV, P_d=  -1.592
    MeV, Pa_prime=  -1.592 MeV
Binding energies        : B_n=    5.872 MeV,   B_p=    6.400 MeV
Constant temp. param.   : T=      0.545 MeV,   E0=    -1.800 MeV
Spin cut-off parameters : sig_n=  4.474        sig_p=  4.474
Level densities         : rho_n= 0.23818E+07 1/MeV, rho_p= 0.62825E+07 1/MeV
Calculate rho and sigma at Ex (MeV)  <  5.872>:
For Ex =  5.872 MeV     : rho  = 0.23818E+07 1/MeV, sig =  4.474
Write file with spin distribution for spin cut-off sig = <  4.474>:

File spindis.rbn written with <I> = 5.10, Pmax @ I = sigma-0.5 = 4.0 and sum_P
    =1.002
```

The last and fourth model, the Fermi gas formula with cut-off parameter will again give you two initial options of parameters. The value of a and $E1$ and thus calculating other values.

```
You may choose another a and/or E1 than proposed by E&B2009:
Level density parameter a    < 17.442>:
Total backshift parameter E1 < -1.177>:

Shell values            : S=     -0.744 MeV,   dS/dA= -0.196 MeV
Pairing energies        : P_n=    0.662 MeV,   P_p=    0.761 MeV, P_d=  -1.592
    MeV, Pa_prime=  -1.592 MeV
Binding energies        : B_n=    5.872 MeV,   B_p=    6.400 MeV
Fermi gas parameters    : a=     17.442 1/MeV, E1=    -1.177 MeV
Spin cut-off parameters : sig_n=  4.922        sig_p=  4.981
Level densities         : rho_n= 0.21794E+07 1/MeV, rho_p= 0.44515E+07 1/MeV
Temperature (FG)        : T(Bn)= 0.66503E+00 MeV,   T(Bp)= 0.68841E+00 MeV
Calculate rho and sigma at Ex (MeV)  <  5.872>:
For Ex =  5.872 MeV     : rho  = 0.21794E+07 1/MeV, sig =  4.922
```

```
Write file with spin distribution for spin cut-off sig = <  4.474>:

File spindis.rbn written with <I> = 5.10, Pmax @ I = sigma-0.5 = 4.0 and sum_P
    =1.002
```

5.3.4 d2rho - level density and spacing.

This program needs no input files, but will load its previous input. This program calculates the level density, $\rho(Sn)$ at the neutron separation energy to normalize the level density.

These values come from s-wave neutron resonance capture, l=0. The g.s. spin of ^{187}Re is 5/2+, so the target spin is 2.5. From table 5.1 we find that the average resonance spacing $D_0 = 3.61 \pm 0.13$ eV and from table 5.2 we use the spin cut-off parameter of 80% of RMI at $\sigma(S_n)_{80\%}$. This is chosen as a reasonable estimate, and as we evaluate standard deviations later, this value is set to zero. The systematic uncertainties arising from these values are considered in the final results. This program then calculates the nuclear level density at the neutron separation energy and the uncertainty associated with it.

```
$ d2rho
...
s- (l=0) or p- (l=1) wave neutron/proton capture                    <0>:
Target spin in (n,g) or (p,g) reaction (for the A-1 nucleus)     < 2.5>:
Neutron or proton resonance spacing parameter D (eV)        <     3.61>:
Standard deviation for resonance spacing parameter dD (eV)  <     0.13>:
Spin cut-off parameter sigma                                <     6.72>:
Standard deviation of spin cut-off parameter sigma          <     0.00>:

Spin populated in nucleus A:  2,  3. Parity = parity of gs of nucleus A-1
Level density is rho = 4.649E+06 +/- 1.674E+05 1/MeV
...
```

5.3.5 Rhosigchi - extracting the NLD and γSF

This is the code reading the first generation matrix from mama. Rhosigchi will only read a maximum of 511 channels on each axis, which means we send in the compressed matrix. Using mama to plot out and look at the compressed first generation matrix, we need to choose areas to use which have good statistics. As a lower limit of γ energy (x-axis), we choose the first area where it looks like a complete dataset and its not oversubracted or "empty" in fig. 5.3. We therefore chose to set the lower γ energy limit to the bin close to $\approx$ 850 keV, and the limit of the exitation energy between $\approx$ 2000 keV and around the neutron separation energy at $\approx$ 5800 keV.

```
$ rhosigchi
...
Filename          <TEST>:alfna_fg_cofinal
...
Lower limit of gamma energy (keV)      <  848.5>:
Lower limit of excitation energy (keV) < 2088.5>:
Upper limit of excitation energy (keV) < 5808.5>:
 Number of data points             216
 DOF, data points-rho-sig          178
Common calibration is a0=-887.50keV and a1= 248.00keV/ch
Dimension is  57 x  28
excitation energy region is  2088.keV to   5808.keV
rho extracted from  -888.keV to   5064.keV
sig extracted from   848.keV to  13000.keV
...
 ------------------------------------------------------
        Convergence test using various indicators
Indicator Iteration = 0    10    20    30    40    50
Rho/Rho0 at  U= 600.  1.00  1.37  1.38  1.39  1.40  1.41
Rho/Rho0 at  U=2336.  1.00  1.15  1.15  1.14  1.14  1.13
Rho/Rho0 at  U=4072.  1.00  0.82  0.81  0.80  0.78  0.77
Sig/Sig0 at Eg=2336.  1.00  1.12  1.11  1.11  1.11  1.10
```

```
Sig/Sig0 at Eg=4072.  1.00  1.52  1.49  1.47  1.45  1.43
Chi^2 for 1.gen.sp.   4.13  1.16  1.16  1.16  1.16  1.16
 ------------------------------------------------------
...
Observed first generation matrix written to file:     fg.rsg
Estimated first gen. err. matrix written to file:  fgerr.rsg
Theoret. first generation matrix written to file:  fgteo.rsg
Unnormalized Rho and dRho written to array file:  rhopaw.rsg
Unnormalized T and dT     written to array file:  sigpaw.rsg
Unnormalized Rho and dRho written to mama file:    rhosp.rsg
Unnormalized T and dT     written to mama file:    sigsp.rsg
...
```

The iteration very quickly converges after only 10 iterations with a χ^2 of 1.16.

5.3.6 Counting - normalizes the NLD

Finally, the NLD and the γSF must be normalized to external data. Counting is where we add the final parameters and choose in which areas to do the fits for the NLD. A run with a "wide fit" of a large range of data points was done to determine the optimal nuclear temperature T, by looking at the χ^2 result. The best fit ended up being $T = 0.545$ MeV. The data point ranges entered in this given run is the same ones as the final result shown. These are chosen both after evaluating comparisons with earlier data presented in the results in chapter 6.

When running counting, the first thing it does is to load datafiles from several of the previous programs, as well as the previously mentioned counting.dat with the experimentally known levels for normalisation of the low energy NLD.

```
$ counting
...
Reading calibration and dimensions from: rhosp.rsg
rhosp.rsg has dimension (0 : 27, 0 : 1) and calibration (a0, a1) = (-887.500000,
     248.000000)
Reading calibration and dimensions from: sigsp.rsg
sigsp.rsg has dimension (0 : 56, 0 : 1) and calibration (a0, a1) = (-887.500000,
     248.000000)

Reading data and errors of experimental nuclear level density: rhopaw.rsg
...
Reading data and errors of experimental transmision coefficient: sigpaw.rsg
...
Reading excitation energies of known levels: counting.dat
...
You may want to smooth the discrete level density with the
resolution of the experimental level density (FWHM = 100-500 keV).
If no smoothing, set FWHM = 0.
Excitation energy FWHM (keV) <150.000>:
...
```

After this, some basic information is needed and then spin cut model to use. We have chosen the nicknamed "Alex" model [42].

```
Mass number A              <188>:
Neutron or proton binding energy (Bn or Bp) (MeV)  < 5.871>:
Choose constant temperature CT (1) or Fermi gas FG (2) formula <1>:
...
Choose RMI(FG+CT) (1), G&C(FG+CT) (2), E&B(CT) (3), E&B(FG+CT) (4), or Alex (5)
    <5>:
...
```

Then, the excitation energy for Ex1 is the average E_x calculated for Alex, and the spin cutoff is the one calculated from this and the average spin. Excitation energy of upper point is, of course, the neutron binding energy, and the spin cutoff here is calculated from Robin and can be found as the $\rho(S_n)$ at 80% of RMI in table 5.2. The level density and uncertainty at B_n is the one given from d2rho.

```
Give excitation energy Ex1 for lower point <  0.233>:
```

```
Give spin cutoff sig1 for lower point      <  2.650>:
Give excitation energy Ex2 for upper point <  5.871>:
Give spin cutoff sig2 for upper point      <  6.725>:
Constants for sig**2 = A + B * Ex: A = 5.443691 and B = 6.776007 MeV**(-1)

Be sure to use the correct Rho(Bn or Bp) according
to type 1, 2, 3, 4 or 5. Run the d2rho program to find Rho
or use the systematic value found by running Robin
Level density at Bn or Bp (1/MeV)                < 4649000>:
Uncertainty of level density at Bn or Bp (1/MeV) <  167400>:

You need to run the program Robin to get the constant temperature parameters T:
Temperature parameter T (MeV) <  0.545>:

The level density goes through Rho(Bn), thus determining the
const. temp. shift parameter to be E0 =  -2.165 MeV
```

We then choose which ranges of data points to use in the fits specifically. This is something that does require some testing, just adding the data points with reasonable statistics and testing how the resulting plot "looks".

```
  No   Ex(keV)   RhoLeV(1/MeV)
...
  3   -143.50       1.946e+00
------------------------------
  4    104.50       3.081e+01
  5    352.50       7.699e+01
  6    600.50       1.160e+02
  7    848.50       1.943e+02
------------------------------
  8   1096.50       2.000e+02
...
Lower fit limit L1 for known levels  <  4>:
Higher fit limit L2 for known levels <  7>:

 No   Ex(keV)      Rho(1/MeV)     dRho(1/MeV)
...
 17   3328.50       7.733e-01       9.992e-02
---------------------------------------------
 18   3576.50       6.679e-01       1.009e-01
 19   3824.50       5.018e-01       8.629e-02
 20   4072.50       7.705e-01       1.087e-01
 21   4320.50       2.622e-01       9.611e-02
 22   4568.50       2.748e-01       1.221e-01
 23   4816.50       2.036e-01       1.526e-01
 24   5064.50       4.759e-01       3.234e-01
---------------------------------------------
 25   5312.50       0.000e+00       0.000e+00
...
Lower fit limit H1 for Rho around Bn or Bp  < 18>:
Higher fit limit H2 for Rho around Bn or Bp < 24>:

 No   Eg(keV)         Trans           dTrans
...
  6    600.50       0.000e+00       0.000e+00
-----------------------------------------------
  7    848.50       1.277e+00       1.471e-01
  8   1096.50       1.879e+00       1.382e-01
  9   1344.50       2.150e+00       1.191e-01
-----------------------------------------------
 10   1592.50       2.122e+00       1.101e-01
...
Lower fit limit L1 for low energy region of T(Eg)  <  7>:
Higher fit limit L2 for low energy region of T(Eg) <  9>:

 No   Eg(keV)         Trans           dTrans
...
 19   3824.50       4.307e-01       6.238e-02
-----------------------------------------------
```

```
 20   4072.50       4.475e-01       6.101e-02
 21   4320.50       2.738e-01       4.313e-02
 22   4568.50       1.799e-01       3.974e-02
 23   4816.50       2.086e-01       4.266e-02
-------------------------------------------
 24   5064.50       2.392e-01       6.816e-02
...
Lower fit limit H1 for high energy region of T(Eg)  < 20>:
Higher fit limit H2 for high energy region of T(Eg) < 23>:
```

After adding those data points for the normalization of the plot, the code will then give the fitted nuclear temperatures T with a reduced χ^2, which in this example does not look like a good fit, but as previously mentioned, this is because the optimisation of T is done with a wider choice of data points in a different run.

```
 Fermi-gas level density has been multiplied with eta =  1.000
in order to match Rho(Bn or Bp) = 4649000.0 (1/MeV)

Spin cutoff parameter used at Bn or Bp =  6.725

 Fitting T to chosen data in the higher region
     T                E0          Chi2          Chi2/free
...
   0.535      -2.008    13.114     2.623
   0.540      -2.086    12.819     2.564
   0.545      -2.165    12.551     2.510
   0.550      -2.244    12.309     2.462
   0.555      -2.323    12.092     2.418
...
Number of free parameter in upper region: 5
...
File sigpawext.cnt (0:80) written to disk, (a0,a1)=( -887.50, 248.000)
File extendLH.cnt (0:80) (0:80) written to disk, (a0,a1)=( -887.50, 248.000)
File rholev.cnt (0:28) written to disk, (a0,a1)=( -887.50, 248.000)
File spincut.cnt (0:84) written to disk, (a0,a1)=( -887.50, 248.000)
File talys_nld_cnt.txt written to disk. The table has 43 rows and 35 columns.
File counting.cpp written to disk. Run root to plot normalized NLD.
File spincut.cpp written to disk. Run root to plot the spincut.
File sigext.cpp written to disk. Run root to plot sigextpaw.cnt.
```

This produces, most importantly, counting.cpp, which plots the NLD as well as sigext.cpp, which is the transmission coefficients. The .cnt-files are the datafiles containing the data, and the .cpp files are the ones plotting the data. The Spincut.cnt-file is also input of normalization of the γSF in the next step.

5.3.7 Normalization - normalizes the γSF

The program normalization does a normalization of the γSF, and produces the last .cpp plotting programs and .nrm data files with the γSF data. We choose the s-waves for neutron capture, as well as the neutron binding energy and ground state spin of target nucleus $(A-1, N-1)$ (i.e. ^{187}Re for this ^{186}W(α,d)^{188}Re-reaction)

The neutron resonance spacing parameter and average radiative width are both from table 5.1.

```
$ normalization
...
Reading calibration and dimensions from: rhosp.rsg
Dimension (0 : 27, 0 : 1) and calibration (a0, a1) = ( -887.50, 248.000)
s- (l=0) or p- (l=1) wave neutron/proton capture              <0>:
Neutron or proton binding energy (Bn or Bp) (MeV)         < 5.871>:
Target spin in (n,g) or (p,g) reaction (for the A-1 nucleus). Use
values 0.0, 1.0,... for even and 0.5, 1.5,... for odd spins < 2.5>:
Neutron resonance spacing parameter D (eV)                <   3.6>:
Average total radiative resonance width G (meV)           <  57.0>:
...
Normalization integral =  5.6766398e+11
```

```
Normalization factor =    3.5952050e+10
File strength.nrm (0:57) written to disk, (a0,a1)=( -887.50, 248.000)
File trans.nrm (0:57) written to disk, (a0,a1)=( -887.50, 248.000)
File transext.nrm (0:289) written to disk, (a0,a1)=( -887.50, 248.000)
File strength.cpp written to disk. Run root to plot strength.nrm
```

5.4 Running the Oslo method software for $^{186}\mathrm{W}(\alpha, t)$

Since the explanation of the ^{186}W(α,d) is relatively thorough and (α,t) has a lot in common with it, I will focus on highlighting the differences and main points. After retrieving the raw matrix, a very similar procedure is applied, mostly with some different parameters. As before, final input files with all constants can be found on the github[27].

5.4.1 MAMA: Unfolding and extracting the first generation γs

Extracting the first generation matrix is very similar to the (a,d) and consists of mainly reading the raw matrix, remove negatives, unfolding the matrix (then remove negatives again), and then extracting the first generation γs before removing negative counts one final time and compressing the bins.

Loading the matrix and removing negative counts:

```
$ mama
...
mama>re
Destination spectrum <1>:
Filename          <TEST>:alfna
...
 CALIBRATION EkeV=6, 0.000000E+00, 7.000000E+00, 0.000000E+00,-5.000000E+02,
    3.100000E+01, 0.000000E+00
 PRECISION=16
 DIMENSION=2,0:1999,0: 499
...
mama>fn
...
Before number of neg. ch. was:  45706, with total counts:    -63476
After  number of neg. ch. is:    1513, with total counts:     -1580
mama>rn
...
Number of channels replaced:          1513
Number of counts before:          157028.0
Number of counts after:           158608.0
Increase of counts:                 1580.0
```

The loaded matrix can be seen in fig. 5.5. Then, loading the same response matrix as for (a,d), and choosing the cut off points to use in the unfolding:

```
mama>rm
...
mama>cr
x=   98, energy =    686.000 keV
y=   24, energy =    244.000 keV
...
x=  492, energy =   3444.000 keV
y=  115, energy =   3065.000 keV
...
```

The bins used are $x \in [98, 492]$ and $y \in [24, 115]$. Then, the unfolding itself also runs with the maximum amount of iterations with the same weight on fluctuations.

```
mama>un
...
First point x1  < 1999>:98
First point y1  <    0>:24
Second point x2 < 1999>:492
Second point y2 <  499>:115
```

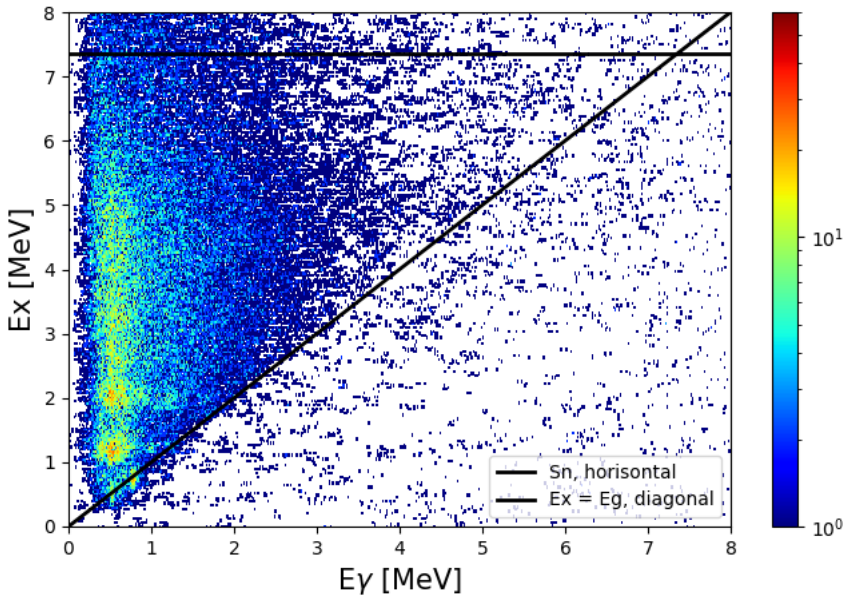

Figure 5.5: The $(\alpha, t\gamma)$ raw spectra after subtracting the negative counts. Bin sizes are 7.0 keV/channel on the x-axis, and 31.0 keV/channel on the y-axis.

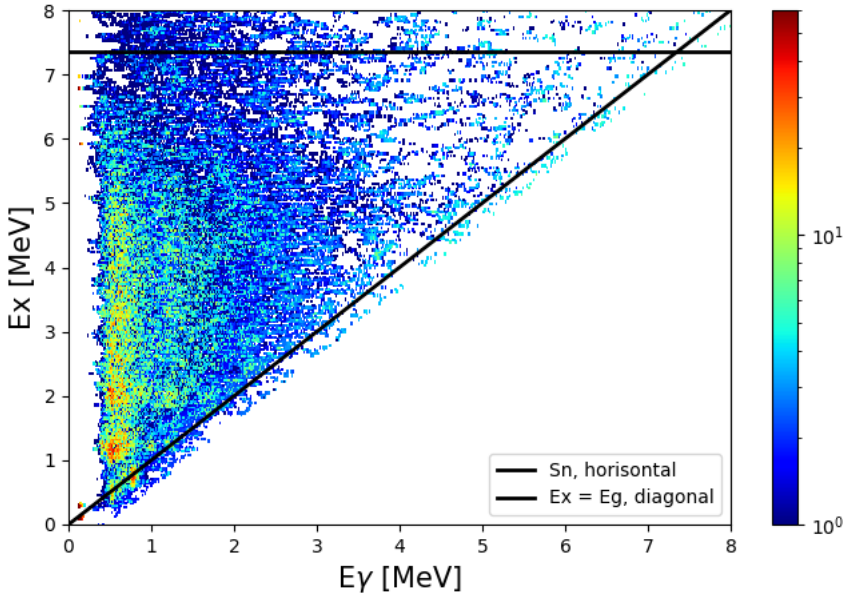

Figure 5.6: The $(\alpha, t\gamma)$ unfolded spectra after subtracting the negative counts. Bin sizes are 7.0 keV/channel on the x-axis, and 31.0 keV/channel on the y-axis.

```
...
Number of iterations ( <500 )  <100>:499
...
Weight on fluctuations <0.2>:
...
 Row: 497  Mode: n  Area:        0(        0)  Chi:   0.00  Fluct:  1.00
 Row: 498  Mode: n  Area:        0(        0)  Chi:   0.00  Fluct:  1.00
 Row: 499  Mode: n  Area:        0(        0)  Chi:   0.00  Fluct:  1.00
Calibration is a0=   0.0keV, a1=   7.00keV/ch
mama>fn
...
Before number of neg. ch. was: 133656, with total counts:    -97698
After  number of neg. ch. is:   20920, with total counts:     -7367
mama>rn
...
Number of channels replaced:         20920
Number of counts before:          175531.6
Number of counts after:           182885.4
Increase of counts:                 7353.9
```

The unfolded matrix can be seen in fig. 5.6. The next step is to obtain the first generation γs. The level density parameter and exponent n are not essential values and only aid the iteration.

```
mama>fg
...
Cal. coeff. a0 (keV) on x-axis   <     0.0>:
Cal. coeff. a1 (keV/ch) on x-axis<     7.0>:

Calibration for excitation energies:
Cal. coeff. a0 (keV) on y-axis   <  -500.0>:
Cal. coeff. a1 (keV/ch) on y-axis<    31.0>:

Excitation energy of highest gate (keV)  <  7994.0>:

Normalization: singles(1) or multiplicity(2)    <2>:
Multiplicity:  statistical(1) or total(2)       <1>:
Area correction for 1. gen. spectra (y/n)       <y>:
Experimental lower gamma thresholds (keV)  <  300.>:
Upper threshold for nonstat. gammas (keV)  <  300.>:
Average entry point in ground band (keV)   <    0.>:
...
Give ratio R           (no sliding = 100.) <  0.30>:
...
Weighting by exp. 1. gen. spectra (y/n)         <n>:

Assumes Fermi gas distribution
Level density parameter a (1/MeV)           <17.62>:
Exponent n for Eg**n                         < 3.00>:

 Multiplicity in each gate:
 -----------------------------------
 Y-ch= 274 Ex=  7994.0 keV < 3.818>:
...
Y-ch=  22  Ex=    182.  Area=         7.1  Alpha=   1.00  dA/A(%)=     0.00
Y-ch=  21  Ex=    151.  Area=         1.8  Alpha=   1.00  dA/A(%)=     0.00
Y-ch=  20  Ex=    120.  Area=         1.7  Alpha=   1.00  dA/A(%)=     0.00
Y-ch=  19  Ex=     89.  Area=         0.0  Alpha=   1.00  dA/A(%)=  9999.99
Y-ch=  18  Ex=     58.  Area=         0.0  Alpha=   1.00  dA/A(%)=  9999.99
Y-ch=  17  Ex=     27.  Area=         0.0  Alpha=   1.00  dA/A(%)=  9999.99
Y-ch=  16  Ex=     -4.  Area=         3.8  Alpha=   1.00  dA/A(%)=     0.00
-----------------------------------------------

Iteration loop = 20, stop(0), activate/modify direct decay(1) or continue(2)
    <2>:0
Last iteration 20 stored in matrix 1
Additional results written to figegaout.dat
mama>fn
...
Before number of neg. ch. was:  82147, with total counts:    -51543
```

```
After  number of neg. ch. is:   10898, with total counts:     -4329
mama>rn
...
Number of channels replaced:         10898
Number of counts before:           81984.9
Number of counts after:            86313.5
Increase of counts:                 4328.6
```

After 20 iteration loops, all values of dA/A have converged to 1.0, except the divide-by-zero values of 9999.99. The final first generation matrix as well as the same matrix compressed to 245.0keV/channel x-axis and 248.0 keV on the y-axis is plotted in fig. 5.7.

5.4.2 Robin, d2rho and rhosigchi

Robin was used in the same way as for (α, t), finding input parameters for the other parts of the program.

D2rho calculates the level density, $\rho(Sn)$ at the neutron separation energy to normalize the level density. The g.s. spin and parity of ^{186}Re is 1^-, so target spin is 1.0, and the average resonance spacing $D_0 = 2.26 \pm 0.23$ is from table 5.1. The spin cut-off parameter is again calculated from Robin in table 5.2.

```
$ d2rho
...
- (l=0) or p- (l=1) wave neutron/proton capture                    <0>:
Target spin in (n,g) or (p,g) reaction (for the A-1 nucleus)     < 1.0>:
Neutron or proton resonance spacing parameter D (eV)        <     2.26>:
Standard deviation for resonance spacing parameter dD (eV)  <     0.23>:
Spin cut-off parameter sigma                                <     6.87>:
Standard deviation of spin cut-off parameter sigma          <     0.00>:

Spin populated in nucleus A:  1/2,  3/2. Parity = parity of gs of nucleus A-1
Level density is rho = 1.439E+07 +/- 1.464E+06 1/MeV
...
```

Rhosigchi needs the input of limits of where the statistics is sufficient. The lower E_γ spectra is set to $\approx$ 850keV, and the limits of E_x is set from $\approx$ 1600keV up to around $\approx$ 5300keV where the data in the matrix is quickly diminishing, and we do not have a sufficient amount of coincidences to extract any meaningful results.

```
$ rhosigchi
...
Filename          <TEST>:alfna_fg_cofinal
...
Lower limit of gamma energy (keV)      <  848.5>:
Lower limit of excitation energy (keV) < 1592.5>:
Upper limit of excitation energy (keV) < 5312.5>:
...
 ---------------------------------------------------------
        Convergence test using various indicators
Indicator Iteration = 0    10    20    30    40    50
Rho/Rho0 at  U= 600.  1.00  1.68  1.71  1.71  1.71  1.72
Rho/Rho0 at  U=2088.  1.00  1.06  1.07  1.07  1.07  1.06
Rho/Rho0 at  U=3576.  1.00  0.47  0.46  0.46  0.46  0.46
Sig/Sig0 at Eg=2088.  1.00  1.33  1.34  1.34  1.34  1.34
Sig/Sig0 at Eg=3576.  1.00  1.54  1.53  1.52  1.52  1.51
Chi^2 for 1.gen.sp.   6.62  1.11  1.05  1.05  1.05  1.05
 ---------------------------------------------------------
...
```

Again, we see how the iteration very quickly converges, as the χ^2 falls to 1.05 after only 20 iterations, but already had a good result of $\chi^2 = 1.11$ after only 10 iterations.

5.4.3 Counting

Running counting for $(\alpha, t\gamma)$, the input parameters are found in the same way as for $(\alpha, d\gamma)$.

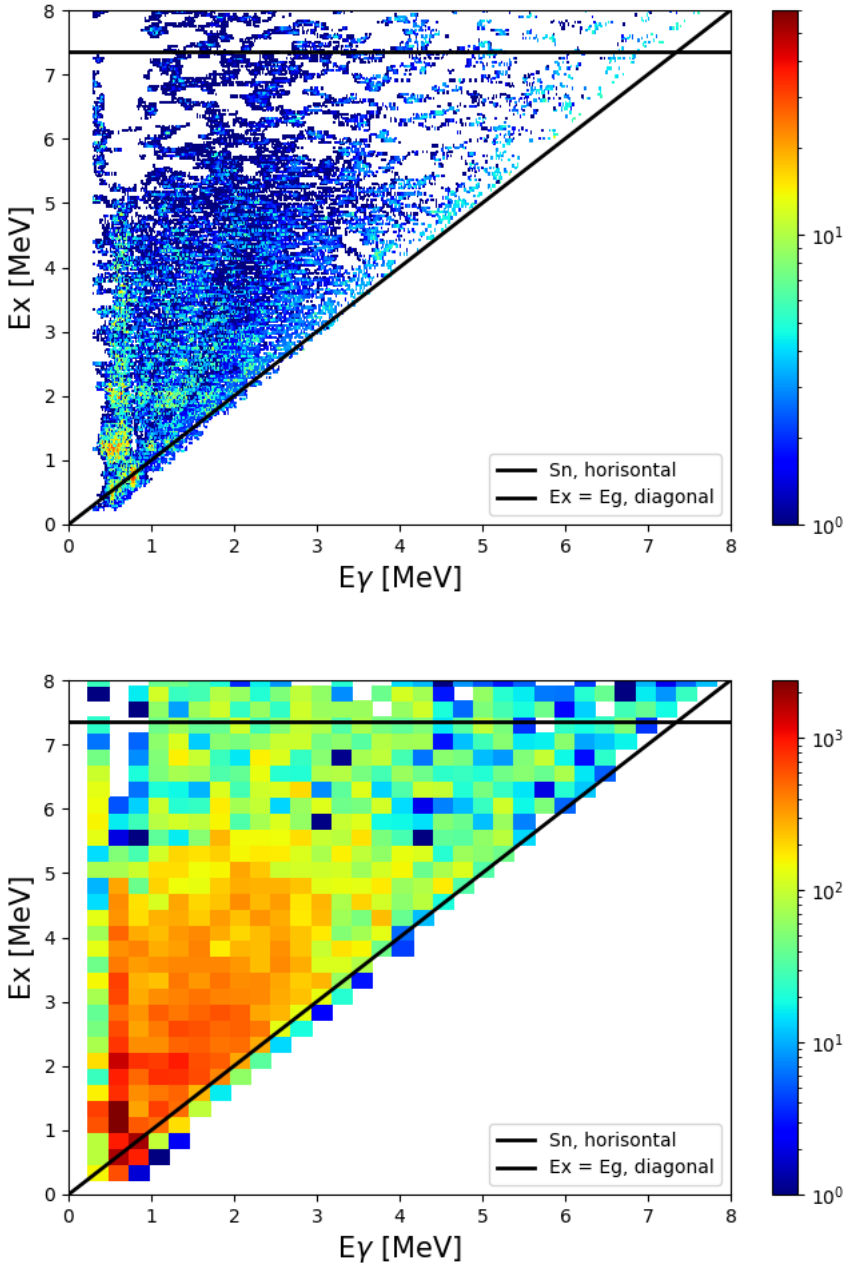

Figure 5.7: The $(\alpha, t\gamma)$ first generation spectra after subtracting the negative counts. The uppermost plot is before rebinning, where bin sizes are 7.0 keV/channel on the x-axis, and 31.0 keV/channel on the y-axis, and the lower is the final, compressed matrix of an x-axis with 245.0keV/channel and y-axis with 248.0keV/channel. The bins are plotted centered on their values.

```
$ counting
...
Excitation energy FWHM (keV) <150.000>:
...
Mass number A              <187>:
Neutron or proton binding energy (Bn or Bp) (MeV)  < 7.360>:
...
Choose constant temperature CT (1) or Fermi gas FG (2) formula <1>:
...
Please, choose your spin cutoff formula:
...
5 Interpolate between known cutoff parameters (Alex2017)
...
Choose RMI(FG+CT) (1), G&C(FG+CT) (2), E&B(CT) (3), E&B(FG+CT) (4), or Alex (5)
    <5>:
...
Give excitation energy Ex1 for lower point <  0.538>:
Give spin cutoff sig1 for lower point      <  2.850>:
Give excitation energy Ex2 for upper point <  7.360>:
Give spin cutoff sig2 for upper point      <  6.874>:
Constants for sig**2 = A + B * Ex: A = 5.037896 and B = 5.735595 MeV**(-1)
...
Level density at Bn or Bp (1/MeV)                <14390000>:
Uncertainty of level density at Bn or Bp (1/MeV) < 1464000>:

You need to run the program Robin to get the constant temperature parameters T:
Temperature parameter T (MeV) <  0.545>:
```

The temperature parameter T was also optimised for this matrix, but the temperature was found to be very close to the $T = 0.545$ MeV found for the $(\alpha, d\gamma)$ matrix, and as the statistics of that matrix is a lot better, we use this value for both matrices.

Next is the areas chosen for the normalizations:

```
 No   Ex(keV)   RhoLeV(1/MeV)
...
  4    104.50       9.294e+00
------------------------------
  5    352.50       1.191e+01
  6    600.50       3.890e+01
  7    848.50       6.332e+01
------------------------------
  8   1096.50       5.556e+01
...
Lower fit limit L1 for known levels  <  5>:
Higher fit limit L2 for known levels <  7>:

 No   Ex(keV)      Rho(1/MeV)     dRho(1/MeV)
...
 16   3080.50       8.162e-01       8.674e-02
---------------------------------------------
 17   3328.50       5.887e-01       8.591e-02
 18   3576.50       4.569e-01       8.201e-02
 19   3824.50       4.997e-01       8.276e-02
 20   4072.50       4.052e-01       1.053e-01
 21   4320.50       3.339e-01       1.367e-01
---------------------------------------------
 22   4568.50       1.409e-01       1.366e-01
...
Lower fit limit H1 for Rho around Bn or Bp  < 17>:
Higher fit limit H2 for Rho around Bn or Bp < 21>:

 No   Eg(keV)         Trans           dTrans
...
  7    848.50       2.548e+00       1.891e-01
---------------------------------------------
  8   1096.50       2.747e+00       1.633e-01
  9   1344.50       3.050e+00       1.678e-01
 10   1592.50       2.542e+00       1.290e-01
---------------------------------------------
```

```
 11   1840.50       2.221e+00       1.376e-01
...
Lower fit limit L1 for low energy region of T(Eg)  <  8>:
Higher fit limit L2 for low energy region of T(Eg) < 10>:

 No   Eg(keV)         Trans           dTrans
...
 17   3328.50       4.755e-01       7.556e-02
-------------------------------------------
 18   3576.50       4.647e-01       6.309e-02
 19   3824.50       5.219e-01       7.337e-02
 20   4072.50       2.685e-01       6.322e-02
 21   4320.50       2.557e-01       5.425e-02
-------------------------------------------
 22   4568.50       2.335e-01       6.044e-02
...
Lower fit limit H1 for high energy region of T(Eg)  < 18>:
Higher fit limit H2 for high energy region of T(Eg) < 21>:
```

After this, the final adjustments can be done and, from not using a large amount of data points in this run, the χ^2 does not represent a realistic value for optimization.

```
Fermi-gas level density has been multiplied with eta =  1.000
in order to match Rho(Bn or Bp) = 14390000.0 (1/MeV)

Spin cutoff parameter used at Bn or Bp =  6.874

 Fitting T to chosen data in the higher region
     T                E0          Chi2          Chi2/free
...
   0.530       -1.039     0.794     0.265
   0.535       -1.123     0.801     0.267
   0.540       -1.208     0.837     0.279
   0.545       -1.292     0.902     0.301
   0.550       -1.376     0.991     0.330
   0.555       -1.461     1.105     0.368
...
Number of free parameter in upper region: 3
...
```

The output is then written out to files and can be plotted.

5.4.4 Normalization

Finally, running normalization to get the γSF, the neutron binding energy, target spin of ^{186}Re g.s. and the neutron resonance spacing parameter D_0 from table 5.1. The radiative resonance width we used it the one given for ^{188}Re, experimentally found from the $N-1$ nuclei ^{187}Re. This is discussed in section 5.2.

```
$ normalization
...
s- (l=0) or p- (l=1) wave neutron/proton capture              <0>:
Neutron or proton binding energy (Bn or Bp) (MeV)         < 7.360>:
Target spin in (n,g) or (p,g) reaction (for the A-1 nucleus). Use
values 0.0, 1.0,... for even and 0.5, 1.5,... for odd spins < 1.0>:
Neutron resonance spacing parameter D (eV)                <   2.3>:
Average total radiative resonance width G (meV)           <  57.0>:
...
```

Chapter 6

Results and interpretation

Mangt skal vi møte og mangt skal vi mestre!
Dagen i dag - den kan bli vår beste dag.

Fra "Vår beste dag" av Erik Bye

After obtaining the final parameters and plots, the data must be compared and evaluated. Comparing our data to previous measurements and predictions, provides a clearer context of the results. I also evaluate the systematic errors from the input parameters of the normalization, for both the γSF and NLD. A fit of the γSF is important to add it to nuclear reaction codes in future work. There is a limited amount of γSF data available, and no previous measurement of the γ strength functions below the neutron separation energies.

6.1 The extracted nuclear level densities

The level densities, as seen in fig. 6.1, are normalized to known levels at low excitation energies and the calculated level density at S_n for each nuclei. Normalization is done with the constant temperature model (CT), using $T = 0.545$ MeV for both nuclei. The last data point of ^{187}Re that was extracted had very poor statistics and is therefore not included. Experimental levels are found at NNDC[25] for both nuclei, and are added in the Oslo method input files `counting.dat` in the corresponding mama-folders in the github[27].

The extracted NLD of ^{188}Re is generally higher than the one of ^{187}Re, and they are generally parallel in the logarithmic plot. Comparing the values of E_x which has a NLD for both nuclei and excluding $E_x \approx 0$, we define the relationship between the level densities as

$$\Delta\rho = \frac{\rho_{188Re}(E_x)}{\rho_{187Re}(E_x)}, \tag{6.1}$$

and the resulting values are largely constant and average out as

$$\mu = \sum \left(\frac{\Delta\rho}{N}\right) \approx 5.10 \tag{6.2}$$

with a standard deviation of $\sigma \approx 1.07$.

As detailed in chapter 2.3, a comparison was done of the NLD of $^{160-162}$Dy, and the level densities of even N, even Z nuclei were compared to the neighbouring ^{161}Dy of odd N in Guttormsen et al. [8]. They found that the additional, unpaired nucleon of ^{161}Dy carried an additional factor of $e^2 \approx 7.4$ to the NLD compared to the even N neighbour.

Even though ^{187,188}Re are odd/even N and odd Z, and different from $^{160-162}$Dy, the observed pattern we found is still very similar. The values are also very close, and we found a factor of ≈ 5.1 difference of the NLDs compared to ≈ 7.4 in [8], which is consistent with previous findings.

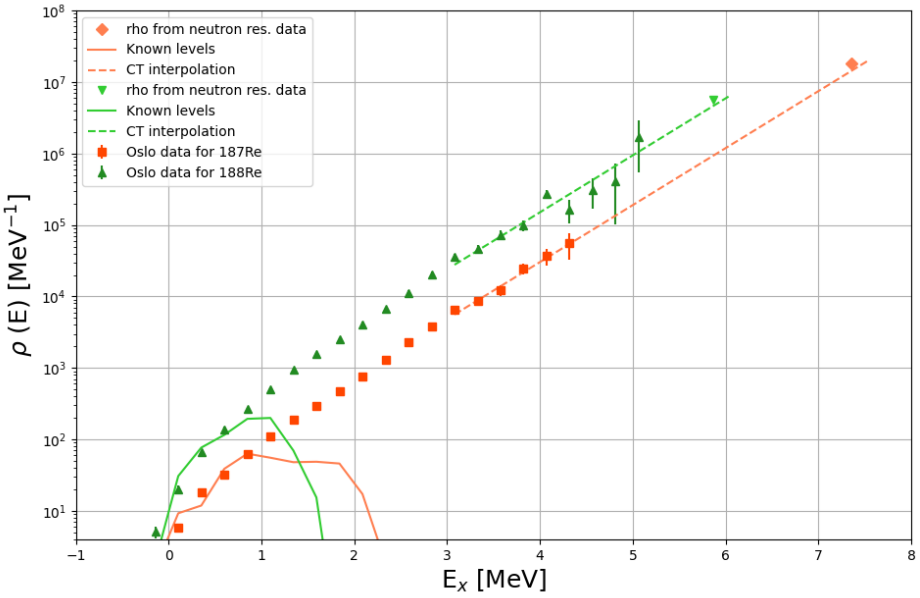

Figure 6.1: The normalized nuclear level densities of ^{187}Re (red squares) and ^{188}Re (green triangles) from this experiment. The level density is approximately a factor of five different from one another (see text for details).

6.2 The γ strength functions

The extracted γ strength functions are plotted in fig. 6.2, but before fully evaluating our results, some preparations and comparisons to external data are necessary.

There are no previous data sets with similar energies for the γSF of these nuclei, but there are supplementary data with a wide range of γ energies for ^{187}Re above S_n to compare with our results. We use the two γ cross section data sets measured by Goryachev et al. in 1973 [11] and Shizuma et al. [46] in 2005. Goryachev et al. did measurements with bremsstrahlung, and yields were then transformed to γ cross sections by an unfolding procedure. This carries some challenges of the uncertanties of the results, as discussed in the paper [11] and by Shizuma et al.[46] and references therein. The results are therefore a γ cross section of ^{187}Re. The data of Shizuma et al. were measures with quasimonochromatic photon beams to produce photodisintegration cross sections ^{187}Re(γ,n)^{186}Re from S_n to 11 MeV. Since the (γ,n) cross section diminished towards S_n as neutron decay competes with γ decay, the γSF calculated from the (γ,n) cross sections becomes artificially low when calculated close to S_n. Because of this, the lowest data point near S_n has been excluded. To calculate this external γ cross section data to a γSF, it's converted by eq. 2.3 as described in chapter 2.4. Our data together with the external data is plotted in fig. 6.3

There are also some additional values of $E1$ and $M1$ of similar mass nuclei in the PSF database of the Nuclear Data Services[47]. These data points have larger uncertainties and not a large range in E_γ. I have therefore not chosen to use these in the fit of Lorentzians later, but they do serve as a nice validation as a brief comparison in fig. 6.4

6.2.1 Fitting Lorenzian functions to the γSF

To use the γSF in reaction codes and to decode the components of the measurement, it is conventional to fit a sum of functions, here collectively called Lorentzians. The parameters are then simple to add into reaction codes, provides a smooth interpolation between data points

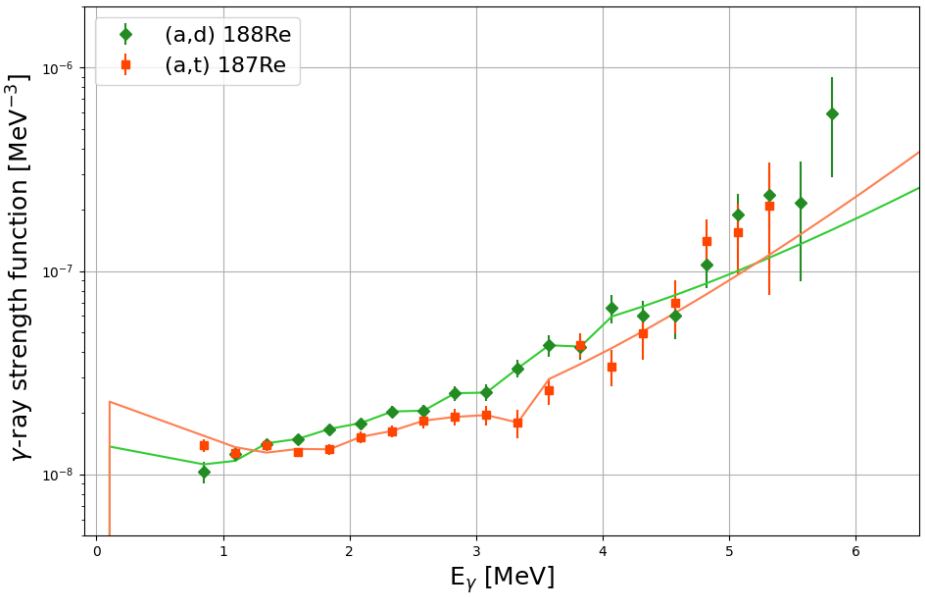

Figure 6.2: The γ strength functions of ^{187}Re and ^{188}Re from this experiment with inter- and extrapolations generated in the Oslo method software.

and if the contributions are assumed to be a collection of Lorentz-shaped resonances, they may provide some assistance in the physical interpretations.

The two functions used here, are the specialized Lorentzian (SLO) and the generalised Lorentzian (GLO) from [48], where ε_γ is the γ energy (i.e. x-axis of plot 6.3). The parameters T, Γ, E and σ_0 (denoted T, Gamma0, E0 and sigma0 in the corresponding code) are used as free parameters in the fit later. First, the SLO is defined from eq. 2.1 in [48]:

$$SLO: f_{E1}^{SLO}(\varepsilon_\gamma) = 8.68 \cdot 10^{-8} \left(\text{mb}^{-1}\text{MeV}^{-2}\right) \cdot \left[\frac{\sigma_0 \varepsilon_\gamma \Gamma^2}{(\varepsilon_\gamma^2 - E^2)^2 + \varepsilon_\gamma^2 \Gamma^2}\right] \tag{6.3}$$

and the GLO is from eq. 2.4 in the same paper as:

$$GLO: f_{E1}^{GLO}(\varepsilon_\gamma, T) = 8.68 \cdot 10^{-8} \left(\text{mb}^{-1}\text{MeV}^{-2}\right) \cdot \left[\frac{\varepsilon_\gamma \Gamma(\varepsilon_\gamma)}{(\varepsilon_\gamma^2 - E^2)^2 + \varepsilon_\gamma^2 \Gamma(\varepsilon_\gamma)^2} + \frac{0.7\Gamma 4\pi^2 T^2}{E^5}\right] \sigma_0 \Gamma, \tag{6.4}$$

where

$$\Gamma(\varepsilon_\gamma) = \Gamma \frac{\varepsilon_\gamma^2 + 4\pi^2 T^2}{E^2}. \tag{6.5}$$

Note how the SLO will have a very different behaviour than the GLO when $\varepsilon_\gamma \to 0$, going towards $f_{E1}^{SLO}(\varepsilon_\gamma = 0, T) = 0$, i.e. steeply towards zero when $E_\gamma \approx 0$ since it is multiplied with ε_γ, where the GLO is not. This is also why the seemingly arbitrary choice was done of when to use either, to better reflect the data close to $\varepsilon \to 0$.

To make a fit of the γ strength function, I used our data as well as the data from Shizuma et al.[46] and Goryachev et al.[11] for both results. The giant resonances at higher γ energies are fitted with Generalised Lorentzians (GLO) and the smaller peaks at around 5MeV and 8MeV are fitted with Specialized Lorentzians (SLO).

The number of functions to fit was decided by starting with two fits to describe the GDR, then adding one more at a time until the total fit seem appropriate. The fitting algorithm

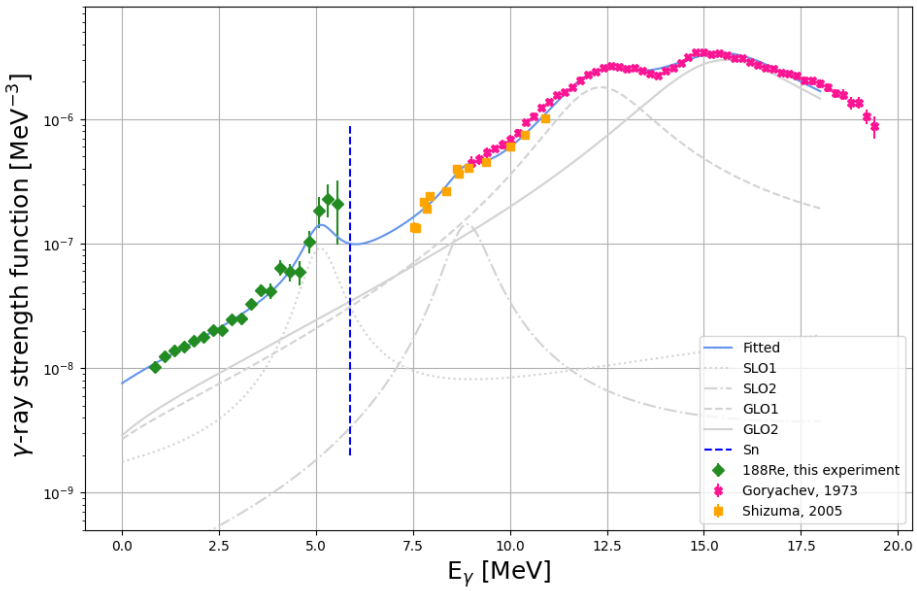

(a) ^{188}Re

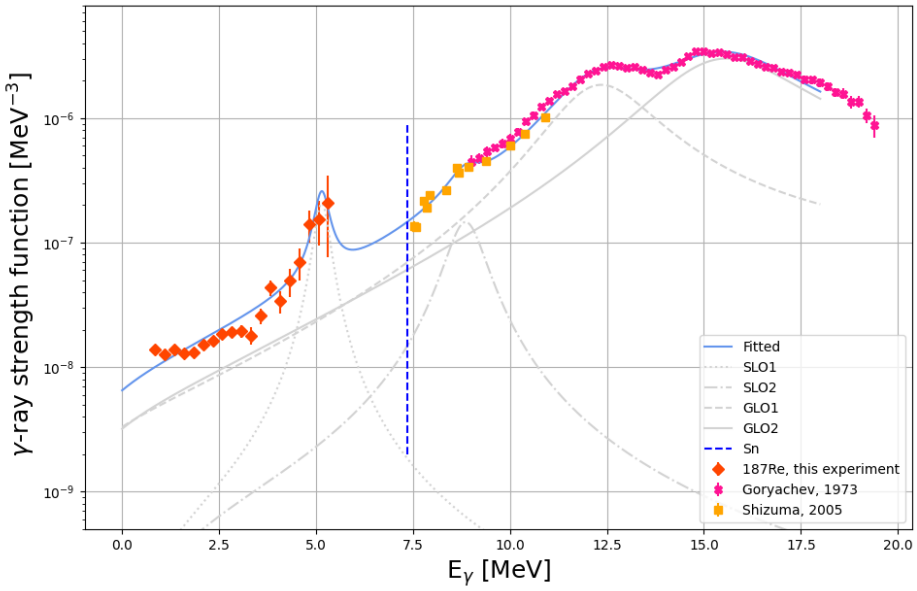

(b) ^{187}Re

Figure 6.3: The nuclear level densities of ^{187}Re and ^{188}Re from this experiment with fitted Lorentzian functions. The parameters of the lowest E_γ special Lorentzian is locked for ^{187}Re with the one fitted for ^{188}Re due to the lack of data closer to the neutron separation energy and poor statistics. The parameters fitted are detailed in table 6.1.

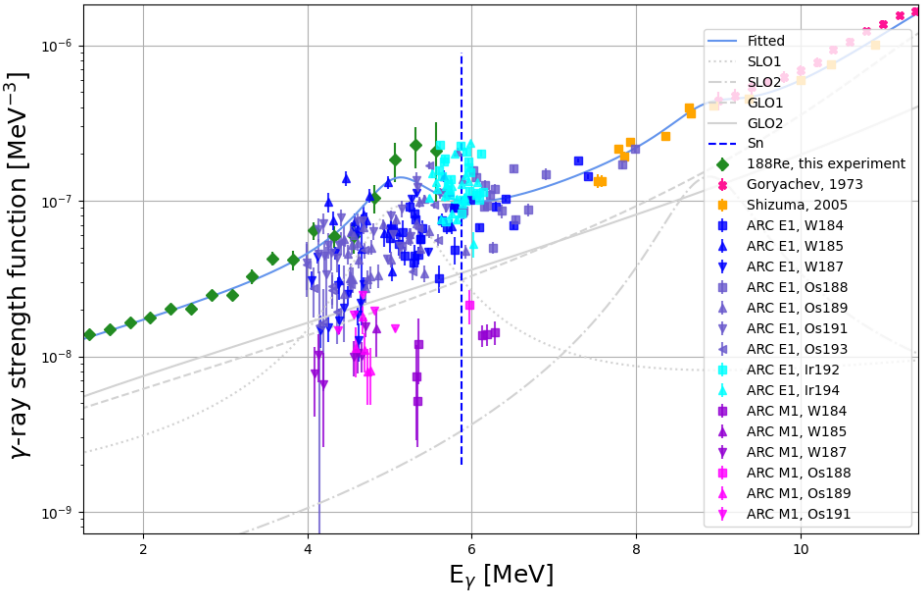

Figure 6.4: The data for ^{188}Re with external data points for similar-mass and neighbouring nuclei from the NDS PSF database[47] as described in the text. A singular high, outlying data point has been omitted as it is not relevant for the main body of data.

187Re			T = 0.992
	E	Γ	σ_0
SLO1	$5.15 \pm *$	$0.43 \pm *$	$12.250 \pm *$
SLO2	8.87 ± 0.10	1.01 ± 0.25	14.939 ± 2.189
GLO1	12.56 ± 0.17	2.34 ± 0.35	323.429 ± 22.602
GLO2	15.97 ± 0.07	3.88 ± 0.33	611.374 ± 22.384

188Re			T = 0.949
	E	Γ	σ_0
SLO1	5.15 ± 0.40	0.43 ± 0.41	12.247 ± 11.079
SLO2	8.94 ± 0.08	0.79 ± 0.17	21.070 ± 2.638
GLO1	12.55 ± 0.15	2.35 ± 0.33	309.718 ± 19.984
GLO2	15.99 ± 0.07	4.09 ± 0.33	598.993 ± 23.176

Table 6.1: The parameters of the GLO and SLO functions, eq. 6.3 and 6.4, in fig. 6.3. The E parameter indicates the approximate centroid of the functions. *The first peak of ^{187}Re with $E \approx 5$ MeV is not varied but set at a constant of the best fitted value of ^{188}Re. The uncertainty is therefore not defined.

minimizes the residue from the fit $\Delta\vec{F}$ which is weighted for statistical errors. For the data points $\vec{D}(\varepsilon_\gamma)$ with statistical error $\delta\vec{D}(\varepsilon_\gamma)$ the least square error weighted for statistical errors may be defined as:

$$\Delta\vec{F} = \frac{\left[\vec{S}(\varepsilon_\gamma, T, \vec{\Gamma}, \vec{E}, \vec{\sigma_0}) - \vec{D}(\varepsilon_\gamma)\right]^2}{(\delta\vec{D})^2}, \tag{6.6}$$

if the sum of the Lorentzian functions, i.e. the total fit, are defined as

$$\begin{aligned}\vec{S}(\varepsilon_\gamma, T, \vec{\Gamma}, \vec{E}, \vec{\sigma_0}) =& f^{SLO}(\varepsilon_\gamma, \Gamma^0, E^0, \sigma_0^0) + f^{SLO}(\varepsilon_\gamma, \Gamma^1, E^1, \sigma_0^1) \\ &+ f^{GLO}(\varepsilon_\gamma, T, \Gamma^2, E^2, \sigma_0^2) + f_{GLO}(\varepsilon_\gamma, T, \Gamma^3, E^3, \sigma_0^3)\end{aligned} \tag{6.7}$$

$\Delta\vec{F}$ is then sent into the fitting algorithm with initial guesses of all parameters, except ε_γ because it represents the x-axis values and is not needed by the algorithm. The algorithm then minimises $\Delta\vec{F}$ with the least squares method by varying the parameters. A minimum and maximum of the parameters is given, but they are set from previous runs and is closely monitored so that the final values are not close to these limits.

The specific algorithm used is the lmfit package[49] which is a framework extending the functionality from other python packages, such as `scipy.optimize.leastsq`. It also provides easy calculations of error estimation, like the χ^2 estimate and covariance matrices.

Final fit parameters are written out in table 6.1, and can be seen in fig. 6.3. The total fitted function has two Lorentzians describing the GDR, and two at lower energies. The peak at $E\gamma \approx 5$ MeV was added to fit the steep increase of the γSF compared to the GDR, and the smaller addition at $E_\gamma \approx 8$ MeV was needed as a last addition to not have a larger discrepancy in this energy area. With these four peaks, the final reduced χ^2 were found to be 24.2 for ^{187}Re and 15.9 for ^{188}Re for the parameters in 6.1.

The covariance matrices are plotted in fig. 6.5 and show clear correlations between the assumed independent variables of the fit. As a general rule-of-thumb, the covariance between two variables show how much their variability is correlated, i.e. the larger the value, the more correlated the parameters are and can no longer be viewed as independent variables. The covariance matrix is a collection of all the covariances of all the parameters used in the calculated fit. Its diagonal of a parameter intersecting with itself, is the variance of a parameter, and the off-diagonal is symmetrical, as the relationship between two parameters are also symmetrical. What we can see is that the σ_0-values are significantly correlated, especially σ_0^2 and σ_0^3 which are the values of the double-humped GDR. This should not be surprising, as the tails of the combined GDR does affect the fit of the other peaks and σ_0 does change this contribution. The variance of σ_0^0 is also very large, as the exact optimal "width" the lowest E_γ peak is hard to estimate due to a lack of data in the E_γ right above. From this, we can conclude that caution must be shown when using this fit to extrapolate physical meaning from these parameters, and that we can not assume them to be independent.

6.2.2 Evaluation of the final γ strength function results

The GDR already present in the Goryachev and Shizuma-data are split into a double humped peak. This might be due to deformation as described in [12]. When only adding these Lorentzians in the fit, there was a distinct lack of strength around 8 MeV, which is why the peak there was added, though we currently have no physical interpretation of what this might be.

There is a possibility of a pygmy resonance at the tail of the GDR, and strength had to be added in the area around $E_\gamma \approx 5$ and above to fit the data properly. More data is needed to make any conclusions, so having data with better statistics for ^{187}Re all the way up to the neutron binding energy would help. For the ^{188}Re data, we found no known measurements of the γ cross sections or γSF, so data is also needed here to conclude on the presence of a potential pygmy resonance.

There are, however, no signs of a significant resonance around 3-4 MeV where the scissors resonance is hypothesised. This is consistent with the theory and predictions about the scissors

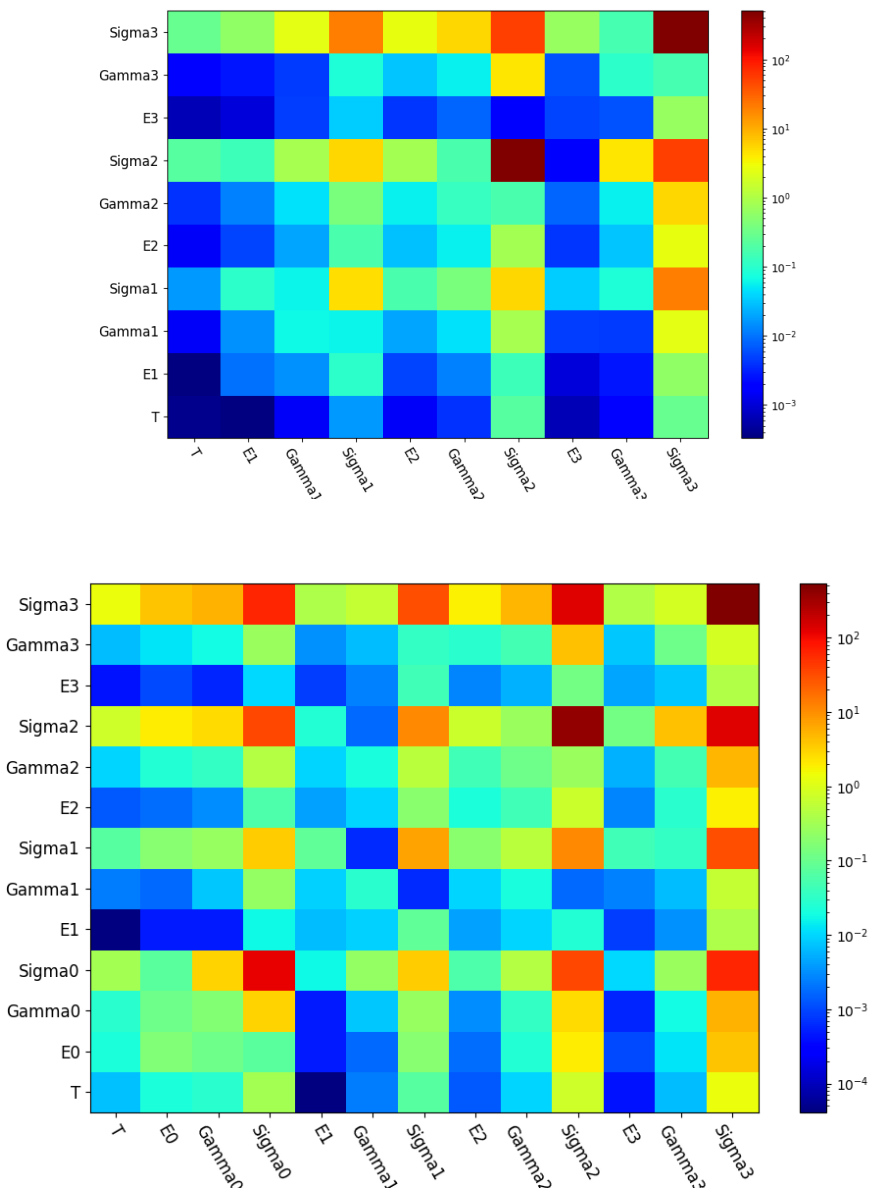

Figure 6.5: The covariance matrices of the parameters to fit the γSF of ^{187}Re (upper) and ^{188}Re (lower) in fig. 6.3 and parameters of table 6.1. The values are logarithmic absolute values, and show strong correlations between the Sigma (σ_0) values of the Lorentzians. Note how the upper matrix has fewer elements as the parameters of the lowest E_γ peak of ^{187}Re are locked and not fitted directly.

resonance in section 2.4.3 where the neighbouring nuclei did not have a strong M1 scissors though the theorised deformation suggested a scissors resonance could be present, which we have not found. Previous measurements of the scissors resonance of actinides ($A \approx 230$) using the Oslo method has also shown stronger resonances relative to some other experiments[18]. Since some previous measurements of the resonance in heavy nuclei have been clearly observed, even at unexpected strengths, there is no reason to believe that if a scissors resonance was present in ^{187,188}Re that it would not have been observed.

No signs of a low energy enhancement was seen above 1 MeV.

6.3 Estimating systematic errors from parameters.

The Oslo method software propagates the statistical errors from the data sets, but the systematical errors introduced by the normalization constants, D_0, $< \Gamma_0 >$ and $\sigma(S_n)$ needs to be estimated separately. $\rho(S_n)$ is also used in the normalization, but as it's correlated to D_0 by the highest D_0 corresponding to the lowest $\rho(S_n)$ and vice versa, only D_0 has been evaluated.

By varying a single value of either parameter at a time within the given errors, we calculate errors for the γSF and for the NLD of both nuclei as previously done in [43]. Separate lower and higher error estimates are made, as the spin cutoff parameter σ doesn't have a traditional error parameter, but is varied from 60% to 100% of the rigid body inertia (RMI).

We denote the NLD as ρ, ρ_{rec} as the recommended NLD, and $\Delta\rho_{rec}$ as the statistical error of ρ_{rec}. The equivalent notation is also used for the γSF, f. Which limit of which parameter that produces high or low estimates of the total functions are given in table 6.2. Squaring and summing the weighted differences for the NLD:

$$STD^2_{\rho,high} = \rho^2_{rec}\left[\left(\frac{\rho_{D_0\downarrow} - \rho_{rec}}{\rho_{rec}}\right)^2 + \left(\frac{\rho_{\sigma\uparrow} - \rho_{rec}}{\rho_{rec}}\right)^2 + \left(\frac{\Delta\rho_{rec}}{\rho_{rec}}\right)^2\right], \tag{6.8}$$

is the higher estimate, and the lower is

$$STD^2_{\rho,low} = \rho^2_{rec}\left[\left(\frac{\rho_{D_0\uparrow} - \rho_{rec}}{\rho_{rec}}\right)^2 + \left(\frac{\rho_{\sigma\downarrow} - \rho_{rec}}{\rho_{rec}}\right)^2 + \left(\frac{\Delta\rho_{rec}}{\rho_{rec}}\right)^2\right]. \tag{6.9}$$

Doing the same for the γSF, f:

$$STD^2_{f,high} = f^2_{rec}\left[\left(\frac{f_{D_0\downarrow} - f_{rec}}{f_{rec}}\right)^2 + \left(\frac{f_{<\Gamma_0>\uparrow} - f_{rec}}{f_{rec}}\right)^2 + \left(\frac{f_{\sigma\uparrow} - f_{rec}}{f_{rec}}\right)^2 + \left(\frac{\Delta f_{rec}}{f_{rec}}\right)^2\right] \tag{6.10}$$

$$STD^2_{f,low} = f^2_{rec}\left[\left(\frac{f_{D_0\uparrow} - f_{rec}}{f_{rec}}\right)^2 + \left(\frac{f_{<\Gamma_0>\downarrow} - f_{rec}}{f_{rec}}\right)^2 + \left(\frac{f_{\sigma\downarrow} - f_{rec}}{f_{rec}}\right)^2 + \left(\frac{\Delta f_{rec}}{f_{rec}}\right)^2\right] \tag{6.11}$$

The higher and lower estimates of ρ and f are then equal to the recommended values with the high or low standard deviation STD, calculated separately for each limit and each dataset as:

$$\rho_{high} = \rho_{rec} + STD_{\rho,high}, \tag{6.12}$$

$$\rho_{low} = \rho_{rec} - STD_{\rho,low}, \tag{6.13}$$

for ρ and for f:

$$f_{high} = f_{rec} + STD_{f,high}, \tag{6.14}$$

$$f_{low} = frec - STD_{f,low}. \tag{6.15}$$

For the different σ values, a band is made for $\sigma = 0.8 \pm 0.1$ and another outer limit for $\sigma = 0.8 \pm 0.2$. The final error estimates of the NLD is in fig. 6.6, and the errors of the γSF in fig. 6.7.

		estimate	D_0	$< \Gamma_0 >$	$\sigma(S_n)$
NLD	ρ	*high*	$\downarrow$	$\times$	$\uparrow$
		low	$\uparrow$	$\times$	$\downarrow$
γSF	f	*high*	$\downarrow$	$\uparrow$	$\uparrow$
		low	$\uparrow$	$\downarrow$	$\downarrow$

Table 6.2: An overview of what limit of which parameters gives the upper and lower estimates of the NLD, σ, and the γSF, f. This is a visual representation of the calculations done in eq. 6.8, 6.9, 6.10 and 6.11.

In section 5.2, the values of the $< \Gamma_0 >$ was discussed and the well supported value of 57 ± 3 meV given for ^{188}Re in Mughabghab[41] was used for both normalizations. The original recommended value for ^{187}Re of $< \Gamma_0 >= 92.5 \pm 10$ is plotted alongside the result in fig. 6.7a (without consideration of it's given error) as a comparison.

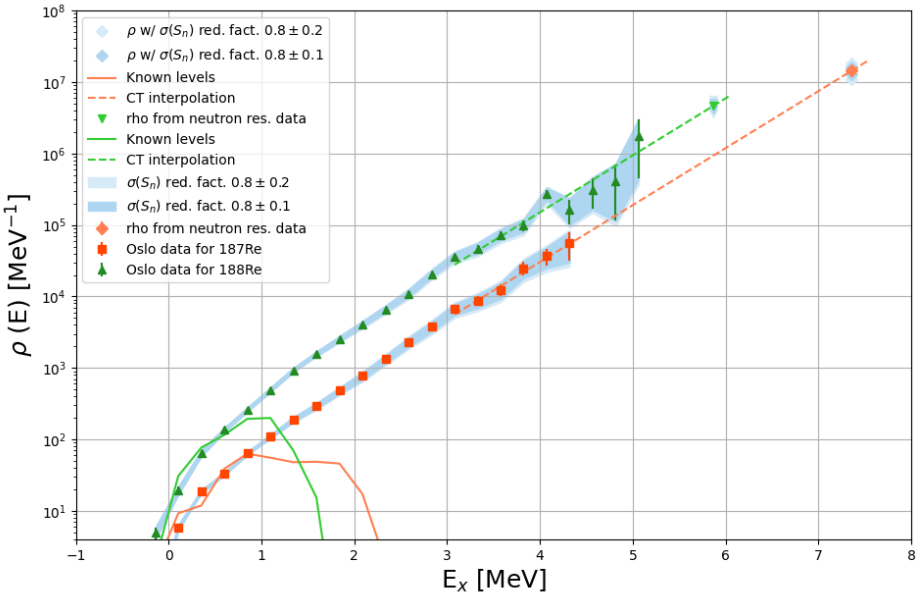

Figure 6.6: The nuclear level densities of ^{187}Re and ^{188}Re from this experiment. Both $\sigma = 0.8 \pm 0.1$ and $\sigma = 0.8 \pm 0.2$ are drawn, but are too narrow to be clearly visible.

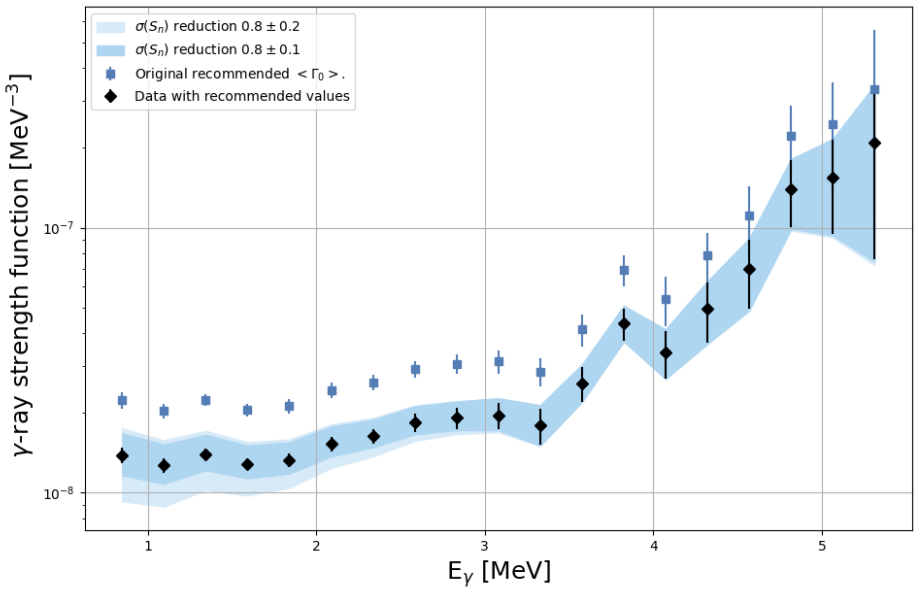

(a) ^{187}Re

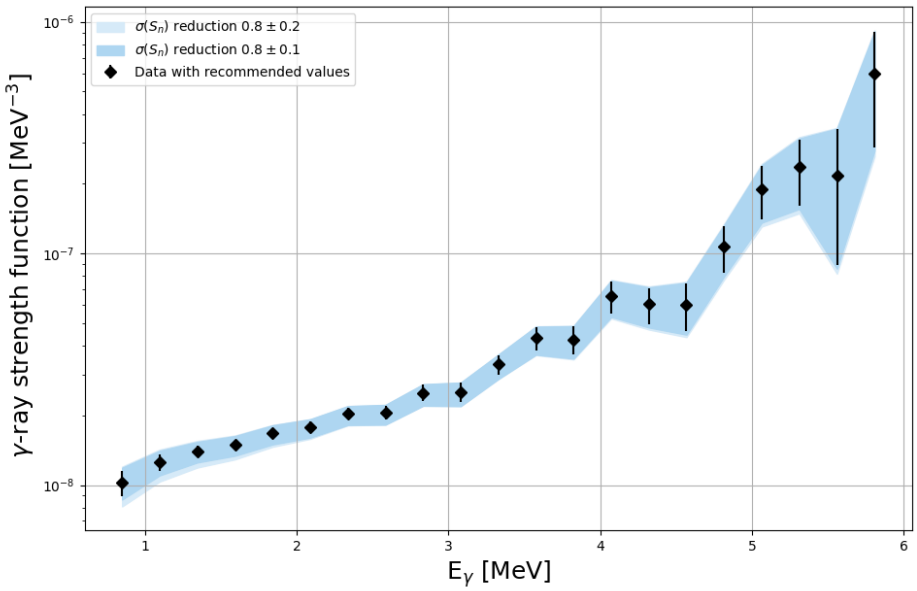

(b) ^{188}Re

Figure 6.7: The γ strength functions of both nuclei with errorbands of estimated systematic errors. ^{187}Re also contains the calculation using the original recommended value of $< \Gamma_0 >$ from table 5.1.

Chapter 7

Summary and outlook

Professor X: What is your superpower?
Me: Hindsight
Professor X: That's not going to help us
Me: Yes, I see that now.

Unknown, Twitter

In this thesis I have used data from the Oslo Cyclotron Laboratory of a 30 MeV α-beam on ^{186}W to study statistical properties of the quasi-continuum in ^{187}Re and ^{188}Re. By using the Oslo method on the (α,t) and (α,d) reaction channels, I was able to extract the γSF and NLD of both ^{187}Re and ^{188}Re. The γSF below the neutron separation energy of either nuclei has never been measured before, and these results together with the NLD will enable the first experimental constraints on the (n, γ) cross section from the unstable ^{186}Re to ^{187}Re.

The measured nuclear level densities behaved very similarly between the two neighbouring nuclei, both being very smooth without significant structures and they had a constant factor of ≈ 5.1 difference, where the odd N, odd Z were the higher one. This is consistent with previous results from similar experiments such as [8], though a more thorough, systematic comparison of other similar-mass nuclei would be interesting.

No low energy enhancement was observed in the γSF above 1 MeV in any of the nuclei, and the γ strength functions did not show a significant scissors resonance around $3 - 4$ MeV. Since the scissors resonance is very dependent on deformation, this points towards there being no significant and well defined deformation of the ground states of the nuclei. By comparing previous measurements from [11] and [46] of the photo cross section of ^{187}Re, there are signs of a possible pygmy resonance around the neutron separation energy, but more data is needed to make a conclusion. A pygmy-type peak had to be added to make a reasonable fit to Lorentzian functions. By also identifying the resonances, or lack thereof, in the γ strength functions, this work may also help understand the systematics of these structural features.

This work was motivated by the need for experimental data in this mass region, with a goal to contribute to the understanding of the ^{186}W s-process branching point and improve upon current theoretical constraints. The next step in this research is to add the measured NLD and γSF in to nuclear reaction networks such as TALYS to calculate its impact on the theorised (n,γ) cross section of ^{187}Re. This can then be evaluated in a larger context and reaction network to see potential further impact on the branching point as a whole. The ^{188}Re (n,γ) calculated from the results of this thesis can also be compared to other external measurements to benchmark this to measured cross sections.

To further refine this work, a further evaluation of the input parameters may improve the confidence of the normalization on these results. The $< \Gamma_0 >$ given for ^{187}Re from the data of ^{186}Re in [41] is very sparse and more systematic evaluations, such as in [43], may show to be beneficial.

As to the double-humped GDR observed in [11], a new experiment to re-examine the specific structural implications predicted by this data would be interesting. As discussed in [46], this

data do carry some challenges, and the given neutron detection has some very challenging aspects to it and uncertainties connected to the uniqueness of all detected neutron signals.

A larger and more systematic evaluation of the nuclear level densities in this mass area would also be very interesting. As the observed level densities of $^{187-188}$Re are very well behaved, a systematic study of the evolution towards shell closures or deformation would be interesting, highlighting the systematic review of the odd/even N and Z.

An experiment targeted at obtaining the γSF of ^{187}Re up to S_n, and for ^{188}Re above S_n would also be important to obtain sufficient data to properly conclude on the presence and characteristics of the pygmy resonance, as it cannot clearly be accounted for by this work alone. As a pygmy resonance would strongly affect the γSF at and around S_n, it might be a large contributor to the (n,γ) cross section and specifically important in astrophysical calculations.

Appendices

Appendix A

Sorting and calibrating

A.1 Running and modifying usersort.cpp

Usersort is locally written software made to sort and calibrate raw data from OCL to do analysis with .root files. There are many local versions, some of which can be found at the OCL github at https://github.com/oslocyclotronlab. The specific version used in this thesis can be found in the github of this thesis at https://github.com/Loopdiloop/master_thesis[27].

It runs on C++ and is also dependent on root https://root.cern/. After building and installing as stated in the README it can be run as "./sorting batchfile.batch".

To add a gate for the analysis on a specific particle peak, an if-test is added to only add values in the γ-t spectra that is corresponding to a certain range of E and dE in Siri. This is done as follows:

Gate for level in 15N:

```
#if defined(MAKE_CACTUS_TIME_ENERGY_PLOTS) && (MAKE_CACTUS_TIME_ENERGY_PLOTS>0)
    if(e_int>6050 && e_int<7200 && de_int>1200 && de_int<1520){
        // gate on the 5/2+ level in 15N at Ex = 5270 keV
        if(ex_int>500){  // Reduce the influence of the elastic peak
            m_nai_e_t[id] ->Fill( na_e_int,  na_t_int );
            m_nai_e_t_all ->Fill( na_e_int,  na_t_int );
            m_nai_e_t_c   ->Fill( na_e_int,  na_t_c );
        }
        m_siri_e_t[ei]->Fill( e_int, na_t_c );
        m_siri_e_t_all->Fill( e_int, na_t_c );
    }
#endif /* MAKE_CACTUS_TIME_ENERGY_PLOTS */
```

/

A.2 The batch file of usersort

The batch file of usersort is the input file of the C++ script sorting the files from the raw output files of the OCL setup and convert it into .root files. The initial sortings are usually done with initial gains, shifts etc., and then using the .root output file, we find calibrations and other adjustments before re-sorting.

The batch-file, together with the gainshift, presented here contains all final adjustments from the last sorting. Hashtag denotes inline comments. I will present all the variables with a brief explanation before showing the full file used for this data analysis in usersort.

- `gain file gainshifts.dat` specifies the gainshift file containing parameters as explained further in appendix A.3.

- `parameter tnai_corr_enai = ...` Corrections walk and leading edge of the NaI cactus detectors. These are the parameters from the fit of XX on m_nai_e_t, leading to the "straightened" version of the same plot m_nai_e_t_c.
- `parameter tnai_corr_esi = ...` Corresponding parameters of tnai_corr_enai for SiRi, corrigating m_siri_e_t, as explained in section 3.7
- `rangefile zrange_d.dat` is a way of simple gating on different particle spectra which, in this thesis, is either deutrons or tritons.
- `parameter ede_rect = ...`
- `parameter thick_range = ...` sets width and size of the rangefile gate.
- `parameter ex_from_ede = ...` is taken directly from kinematic simulations of Qkinz, specifying corrections for ring 0-7 to calculate from particle incident energies on E-dE to excitation energy.
- `parameter ex_corr_exp = ...` not in use.
- `data directory ../master_data/raw` is the directory of the raw input data files.
- `data file sirius-20160420-135618.data ...` After specifying the directory, this is where you add all filenames. All files are added one line at a time, all with the keywords "data file".
- `export mama h_ex_f0 h_ex_f0_MAMA` is used to export to MAMA matrices to do further analysis with the Oslo method software, ompy or MAMA.
- `export root W186_a_d_all_calib.root` exports the now sorted and manipulated data to a .root file.

From this, the full .batch-file looks like this (some comments have been omitted):

```
# a,d

# where to load the gainshifts from; one can also use:
# parameter gain_e = ... and so on
#gain file gainshifts_plain.dat
gain file gainshifts_W186_final.dat

# (constant fraction) cactus energy correction parameters for cactus time
#parameter tnai_corr_enai = 0 1 0 0 // Default
parameter tnai_corr_enai = 0.589716 16054.1 96.2308 -0.000373339 // tcorr for a,
    p

# (constant fraction) siri energy correction parameters for cactus time
#parameter tnai_corr_esi  = 0 1 0 0  // Default
parameter tnai_corr_esi = 8.7091 -66527.8 -491.714 9.78023e-5 // Siricorr, v1 (a
    ,p)

# Parameters for the range curve, 3He or alpha
#rangefile zrange_he3.dat
#rangefile zrange_a.dat
rangefile zrange_d.dat
#rangefile zrange_p.dat

# Cut of low-energy events by making a rectangle which is excluded
# in the down, left corner of the banana.
# Contains E-minimum 1, DE-minimum 1, E-minimum 2, DE-minimum 2.
# Including Z=1 particles:
parameter ede_rect  = 500 250 30 500
# Excluding Z=1 particles:
#parameter ede_rect  = 500 2500 2000 2500

```

```
# Thickness gate for proton banana
parameter thick_range = 125 15 0

# Thickness gate for 3He banana
#parameter thick_range = 48 8 0

# Thickness gate for alpha banana
#parameter thick_range = 165 10 0
#parameter thick_range = 48 5 0

# Fit from Qkinz for converting to energy.
#  186W (alpha, d gamma) 188Re, 30MeV. Strip 0-7 in that order. Deutron-data! [
    keV]
parameter ex_from_ede    = 1.4551283e+4 -1.000915 -8.04e-7 \
1.4556803e+4 -1.000073 -8.18e-7 \
1.4561938e+4 -9.999144e-1 -8.33e-7 \
1.4567338e+4 -9.98259e-1 -8.45e-7 \
1.4572350e+4 -9.97292e-1 -8.60e-7 \
1.4576298e+4 -9.96112e-1 -8.82e-7 \
1.4580493e+4 -9.94982e-1 -9.00e-7 \
1.4584253e+4 -9.93772e-1 -9.21e-7

# empirical excitation energy correction for the above, e.g. from known peaks
parameter ex_corr_exp    =  0 1 \
    0 1 \
    0 1 \
    0 1 \
    0 1 \
    0 1 \
    0 1 \
    0 1


#data directory Datafiles
data directory ../raw_data_186W
#maximum number of buffers to read for each file; for testing
#max_buffers 1

#186W ALL FILES
data file sirius-20160420-135618.data
data file sirius-20160420-171400.data
data file sirius-20160420-182451.data
data file sirius-20160420-233716.data
data file sirius-20160421-091709.data
data file sirius-20160421-100724.data
data file sirius-20160421-224045.data
data file sirius-20160422-081940.data
data file sirius-20160422-093300-big-000.data
data file sirius-20160422-093300-big-001.data
data file sirius-20160422-093300.data
data file sirius-20160422-122054.data
data file sirius-20160422-124416.data
data file sirius-20160422-180843.data
data file sirius-20160423-073059.data
data file sirius-20160423-160731.data
data file sirius-20160423-173835.data
data file sirius-20160423-213756.data
data file sirius-20160424-104217.data
data file sirius-20160424-160703.data
data file sirius-20160424-223103.data
data file sirius-20160425-075414.data
data file sirius-20160425-120131.data
data file sirius-20160425-203224.data
data file sirius-20160425-222023.data
data file sirius-20160426-104456.data
data file sirius-20160426-120853.data
data file sirius-20160426-141446.data
data file sirius-20160426-230123.data
data file sirius-20160427-033555.data
```

```
data file sirius-20160428-091134.data
data file sirius-20160428-122211.data
data file sirius-20160428-173419.data
data file sirius-20160428-230248.data
data file sirius-20160429-070605.data
data file sirius-20160429-094446-big-000.data
data file sirius-20160429-094446-big-001.data
data file sirius-20160429-094446-big-002.data
data file sirius-20160429-094446-big-003.data
data file sirius-20160429-094446.data


# Write to MAMA matrix
#export mama h_ex_f0 h_ex_f0_MAMA
export mama m_alfna alfna
#export mama m_alfna_bg alfna_bg

# at the end, spectra are dumped to the root file
# root output file
export root W186_a_d_all_calib.root
```

A.3 The gainshift file of usersort

The gainshift-file is used by the batchfile and contains a lot of it's namesakes, gains and shifts, but also other correctional parameters. Not all values are used in this project, and are therefore set to 0 or 1 dependent on whether its an additive or multiplicative factor.

- `Line 1 - 8` contains the gain of E of the particle spectra from SiRi.
- `Line 10 - 17` containt the gain of dE , also in the particle spectra from SiRi.
- `Line 19` not used in this project.
- `Line 21 - 25` are the gain of the NaI found in the gamma calibration.
- `Line 27 - 34` are the shift from the E particle spectra.
- `Line 36 - 43` are also the shifts from SiRi, but for dE.
- `Line 45` not used in this project.
- `Line 47 - 51` is the shift of the NaI to line all detectors up. [shift-na]
- `Line 53` not used in this project.
- `Line 55 - 59` Shift in time alignment, t NaI. [shift-t-na]
- `Line 61` not used in this project.
- `Line 63 - 67` gain for NaI time alignment. Not used in this project, as shift was assumed to be sufficient as we are only interested in a single data point area.

The final gainshift file used in this thesis, `gainshifts_W186_final.dat`

```
7.111605 7.192546 7.165704 7.193396 7.206805 7.234765 7.289730 7.324634
7.196596 7.233484 7.263896 7.272741 7.315299 7.328453 7.398356 7.414511
7.167202 7.170212 7.194500 7.246569 7.281545 7.310820 7.404717 7.386424
6.975718 7.024869 7.028252 7.083781 7.097859 7.149961 7.109659 7.200620
6.946819 6.993517 7.026957 7.047295 7.076151 7.125504 7.137700 7.212225
7.077223 7.074586 7.076942 7.114307 7.216790 7.194236 7.274630 7.322052
6.844764 6.917340 6.968574 6.951104 6.978344 7.055593 7.086233 7.071235
7.211216 7.235998 7.203439 7.283856 7.286341 7.409412 7.397140 7.457746

4.174376 4.115991 4.250831 4.033260 4.026550 3.997319 4.011394 4.084808
4.140244 4.111594 4.056781 4.093695 4.015456 4.255210 3.950774 4.006675
```

```
4.129231 4.015426 4.043565 3.838776 3.963493 3.956289 4.024921 3.758659
3.771913 3.919281 3.988218 3.884565 3.932603 3.829781 3.818998 3.726999
4.036192 3.964160 3.976061 3.964429 4.055050 3.911323 3.893128 3.770282
3.929877 3.990988 3.949096 3.956825 3.742416 3.770388 3.780629 4.003623
4.352694 4.177390 4.226649 4.255136 4.049544 3.981681 3.991627 4.063438
3.916964 3.903497 3.876270 4.039508 3.855534 3.954378 3.781481 3.845792

1 1 1 1 1 1

4.22126266 4.19030539 3.8570554  3.7899465  1.          3.65066897 3.66893719
3.72718986 1.          1.          3.74224491 3.70985893 1.          3.58915278
3.73955464 3.69676528 3.66708634 3.17364957 3.51663528 3.41175078 3.59380117
3.47351268 3.57904083 3.57727202 3.34178767 3.4555261  3.50219067 3.55393796
3.52347534 3.51858479 1.          1.

-1066.479620 -1195.256762 -1164.769548 -1224.911270 -1257.231552 -1303.654110
    -1381.537586 -1407.424071
-881.297781 -924.458773 -999.578147 -1050.192690 -1125.757568 -1150.923314
    -1258.121331 -1253.684091
-1336.875680 -1356.590457 -1398.399848 -1474.783926 -1526.231480 -1576.240511
    -1718.244841 -1685.035131
-1270.234277 -1360.722425 -1377.324427 -1474.954013 -1504.357234 -1596.318047
    -1551.434260 -1687.376864
-1107.128125 -1174.929501 -1219.177687 -1253.739359 -1291.318665 -1381.880786
    -1408.777086 -1495.838971
-1367.888002 -1371.035662 -1405.282905 -1474.752397 -1627.979248 -1604.964863
    -1724.996075 -1780.707526
-903.979748 -1011.532404 -1086.660327 -1081.699982 -1129.665508 -1248.341800
    -1301.811781 -1273.422644
-1264.462740 -1287.621907 -1256.127670 -1375.963385 -1378.816815 -1555.193464
    -1547.639706 -1622.252054

-24.089351 -26.947203 -47.955389 -17.417918 -15.092193 -20.721400 -13.302870
    -21.590756
-41.203575 -39.475943 -34.997105 -26.249855 -23.556561 -54.837608 5.908771
    -27.789510
-34.630406 -26.165100 -29.234317 -7.773120 -3.289071 -26.299861 -20.096267
    10.294242
-19.851988 -59.037547 -12.435197 -24.429838 -5.102510 -41.054889 -10.403212
    -7.654215
-322.759255 -264.762862 -210.655368 -187.140298 -213.822227 -298.758164
    -241.905519 -257.623781
-341.748398 -294.517111 -336.559570 -243.625448 -343.251053 -199.761282
    -263.978672 -216.679629
-332.695616 -419.962831 -543.683187 -409.732714 -334.578176 -298.509147
    -352.127334 -277.410445
-329.753375 -274.911043 -383.453733 -343.429968 -355.566525 -330.279274
    -389.287641 -283.017158

0 0 0 0 0 0

-102.63737344 -138.03328103 -46.07145416 -23.61535942 0. 23.91568049 -4.84568032
-4.18237594 0. 0. -34.57227967 -13.8482033 0. 18.31575682
-10.69989689 -57.72636113 -75.16704753 273.46324835 25.21981555 -8.31963752
    27.93786379
29.05291746 37.24903265 26.1341824 -32.1471526 5.63729774 -22.19534441
    -78.85431988
61.23231737 30.36983408 0. 0.

0 0 0 0 0 0

44 39 31 -14  0.    20.5 30
24.5  0.     0. 33 21  0.    24.5
24 21 18.5 27.6 30 22 24.5
22 20 18 18.5 22 17 23
17 17 0.     0.

1 1 1 1 1 1

```

```
1  1  1  1  1  1  1
1  1  1  1  1  1  1
1  1  1  1  1  1  1
1  1  1  1  1  1  1
1  1  1  1
```

Bibliography

[1] E. Margaret Burbidge, G. R. Burbidge, William A. Fowler, and F. Hoyle. Synthesis of the elements in stars. *Rev. Mod. Phys.*, 29:547–650, Oct 1957. doi: 10.1103/RevModPhys.29.547. URL https://link.aps.org/doi/10.1103/RevModPhys.29.547.

[2] A. G. W. Cameron. On the origin of the heavy elements. , 62:9–10, February 1957. doi: 10.1086/107435.

[3] Edward Simpson. The colorful nuclide chart. https://people.physics.anu.edu.au/~ecs103/chart/, 2021. Graphics fetched in March 2021.

[4] F. Käppeler, R. Gallino, S. Bisterzo, and Wako Aoki. The *s* process: Nuclear physics, stellar models, and observations. *Rev. Mod. Phys.*, 83:157–193, Apr 2011. doi: 10.1103/RevModPhys.83.157. URL https://link.aps.org/doi/10.1103/RevModPhys.83.157.

[5] M. R. Drout, A. L. Piro, B. J. Shappee, C. D. Kilpatrick, J. D. Simon, C. Contreras, D. A. Coulter, R. J. Foley, M. R. Siebert, N. Morrell, K. Boutsia, F. Di Mille, T. W.-S. Holoien, D. Kasen, J. A. Kollmeier, B. F. Madore, A. J. Monson, A. Murguia-Berthier, Y.-C. Pan, J. X. Prochaska, E. Ramirez-Ruiz, A. Rest, C. Adams, K. Alatalo, E. Bañados, J. Baughman, T. C. Beers, R. A. Bernstein, T. Bitsakis, A. Campillay, T. T. Hansen, C. R. Higgs, A. P. Ji, G. Maravelias, J. L. Marshall, C. Moni Bidin, J. L. Prieto, K. C. Rasmussen, C. Rojas-Bravo, A. L. Strom, N. Ulloa, J. Vargas-González, Z. Wan, and D. D. Whitten. Light curves of the neutron star merger gw170817/sss17a: Implications for r-process nucleosynthesis. *Science*, 358(6370):1570–1574, 2017. ISSN 0036-8075. doi: 10.1126/science.aaq0049. URL https://science.sciencemag.org/content/358/6370/1570.

[6] GA.J. Koning, S. Hilaire, and M.C. Duijvestijn. "talys-1.0", proceedings of the international conference on nuclear data for science and technology. volume 68, pages 211 – 214. American Physical Society, April 22-27 2003. doi: 10.1103/PhysRevC.68.064306. URL https://tendl.web.psi.ch/tendl_2019/talys.html.

[7] Walter Hauser and Herman Feshbach. The inelastic scattering of neutrons. *Phys. Rev.*, 87:366–373, Jul 1952. doi: 10.1103/PhysRev.87.366. URL https://link.aps.org/doi/10.1103/PhysRev.87.366.

[8] M. Guttormsen, A. Bagheri, R. Chankova, J. Rekstad, S. Siem, A. Schiller, and A. Voinov. Thermal properties and radiative strengths in ^{160,161,162}Dy. *Phys. Rev. C*, 68:064306, Dec 2003. doi: 10.1103/PhysRevC.68.064306. URL https://link.aps.org/doi/10.1103/PhysRevC.68.064306.

[9] G. A. Bartholomew, E. D. Earle, A. J. Ferguson, J. W. Knowles, and M. A. Lone. *Gamma-Ray Strength Functions*. Springer, Berlin, 1973.

[10] Peter Axel. Electric dipole ground-state transition width strength function and 7-mev photon interactions. *Phys. Rev.*, 126:671–683, Apr 1962. doi: 10.1103/PhysRev.126.671. URL https://link.aps.org/doi/10.1103/PhysRev.126.671.

[11] A.M. Goryachev, G.N. Zalesnyj, S.F. Semenko, and B.A. Tulupov. Giant dipole resonance on nuclei of transition region a approximately 190 (gigantskij dipol'nyj rezonans na yadrakh perekhodnoj oblasti a approximately 190). *Yadern Fiz*, 17:463–469, 1973. URL http://inis.iaea.org/search/search.aspx?orig_q=RN:04073028.

[12] A. Bohr, B.R. Mottelson, W.A. Benjamin (Firm), Ray, and Cary Cooper Science Collection. *Nuclear Structure: Volume Ii (nuclear Deformations)*. Nuclear Structure. Basic Books, 1969. ISBN 9780805310160. URL https://books.google.no/books?id=dRhRAAAAMAAJ.

[13] D. Savran, T. Aumann, and A. Zilges. Experimental studies of the pygmy dipole resonance. *Progress in Particle and Nuclear Physics*, 70:210–245, 2013. ISSN 0146-6410. doi: https://doi.org/10.1016/j.ppnp.2013.02.003. URL https://www.sciencedirect.com/science/article/pii/S0146641013000057.

[14] H. K. Toft, A. C. Larsen, A. Bürger, M. Guttormsen, A. Görgen, H. T. Nyhus, T. Renstrøm, S. Siem, G. M. Tveten, and A. Voinov. Evolution of the pygmy dipole resonance in sn isotopes. *Phys. Rev. C*, 83:044320, Apr 2011. doi: 10.1103/PhysRevC.83.044320. URL https://link.aps.org/doi/10.1103/PhysRevC.83.044320.

[15] C. P. Brits, K. L. Malatji, M. Wiedeking, B. V. Kheswa, S. Goriely, F. L. Bello Garrote, D. L. Bleuel, F. Giacoppo, A. Görgen, M. Guttormsen, K. Hadynska-Klek, T. W. Hagen, S. Hilaire, V. W. Ingeberg, H. Jia, M. Klintefjord, A. C. Larsen, S. N. T. Majola, P. Papka, S. Péru, B. Qi, T. Renstrøm, S. J. Rose, E. Sahin, S. Siem, G. M. Tveten, and F. Zeiser. Nuclear level densities and γ-ray strength functions of ^{180,181,182}Ta. *Phys. Rev. C*, 99:054330, May 2019. doi: 10.1103/PhysRevC.99.054330. URL https://link.aps.org/doi/10.1103/PhysRevC.99.054330.

[16] A. Richter. Probing the nuclear magnetic dipole response with electrons, photons and hadrons. *Progress in Particle and Nuclear Physics*, 34:261–284, 1995. ISSN 0146-6410. doi: https://doi.org/10.1016/0146-6410(95)00022-B. URL https://www.sciencedirect.com/science/article/pii/014664109500022B. Electromagnetic Probes and the Structure Hadrons and Nuclei.

[17] J. Enders, P. von Neumann-Cosel, C. Rangacharyulu, and A. Richter. Parameter-free description of orbital magnetic dipole strength. *Phys. Rev. C*, 71:014306, Jan 2005. doi: 10.1103/PhysRevC.71.014306. URL https://link.aps.org/doi/10.1103/PhysRevC.71.014306.

[18] M. Guttormsen, L. A. Bernstein, A. Bürger, A. Görgen, F. Gunsing, T. W. Hagen, A. C. Larsen, T. Renstrøm, S. Siem, M. Wiedeking, and J. N. Wilson. Observation of large scissors resonance strength in actinides. *Phys. Rev. Lett.*, 109:162503, Oct 2012. doi: 10.1103/PhysRevLett.109.162503. URL https://link.aps.org/doi/10.1103/PhysRevLett.109.162503.

[19] A. C. Larsen and S. Goriely. Impact of a low-energy enhancement in the γ-ray strength function on the neutron-capture cross section. *Phys. Rev. C*, 82:014318, Jul 2010. doi: 10.1103/PhysRevC.82.014318. URL https://link.aps.org/doi/10.1103/PhysRevC.82.014318.

[20] A. C. Larsen, N. Blasi, A. Bracco, F. Camera, T. K. Eriksen, A. Görgen, M. Guttormsen, T. W. Hagen, S. Leoni, B. Million, H. T. Nyhus, T. Renstrøm, S. J. Rose, I. E. Ruud, S. Siem, T. Tornyi, G. M. Tveten, A. V. Voinov, and M. Wiedeking. Evidence for the dipole nature of the low-energy γ enhancement in ^{56}Fe. *Phys. Rev. Lett.*, 111:242504, Dec 2013. doi: 10.1103/PhysRevLett.111.242504. URL https://link.aps.org/doi/10.1103/PhysRevLett.111.242504.

[21] M. Wiedeking, L. A. Bernstein, M. Krtička, D. L. Bleuel, J. M. Allmond, M. S. Basunia, J. T. Burke, P. Fallon, R. B. Firestone, B. L. Goldblum, R. Hatarik, P. T. Lake, I-Y. Lee, S. R.

Lesher, S. Paschalis, M. Petri, L. Phair, and N. D. Scielzo. Low-energy enhancement in the photon strength of ^{95}Mo. *Phys. Rev. Lett.*, 108:162503, Apr 2012. doi: 10.1103/PhysRevLett.108.162503. URL https://link.aps.org/doi/10.1103/PhysRevLett.108.162503.

[22] D. M. Brink. Doctoral thesis. *Oxford University*, 1955.

[23] M. Guttormsen, A. Atac, G. Løvhøiden, S. Messelt, T. Ramsøy, J. Rekstad, T. F. Thorsteinsen, T. S. Tveter, and Z. Zelazny. Statistical gamma-decay at low angular momentum. *Physica Scripta*, T32:54–60, 1990. doi: 10.1088/0031-8949/1990/T32/010.

[24] M. Guttormsen, A. Bürger, T.E. Hansen, and N. Lietaer. The siri particle-telescope system. *Nuclear Instruments and Methods in Physics Research Section A: Accelerators, Spectrometers, Detectors and Associated Equipment*, 648(1):168 – 173, 2011. ISSN 0168-9002. doi: https://doi.org/10.1016/j.nima.2011.05.055. URL http://www.sciencedirect.com/science/article/pii/S0168900211010205.

[25] IAEA Nuclear Data Section. The live chart of nucleides, nuclear data section (nds) livechart database. https://nds.iaea.org/relnsd/vcharthtml/VChartHTML.html, 2021. Data fetched march 2021.

[26] M. T. Lu and W. P. Alford. Intrinsic states in odd-a rhenium isotopes. *Phys. Rev. C*, 3: 1243–1265, Mar 1971. doi: 10.1103/PhysRevC.3.1243. URL https://link.aps.org/doi/10.1103/PhysRevC.3.1243.

[27] M. M. Bjørøen. The github associated with this thesis. https://github.com/Loopdiloop/master_thesis, 2021. Final update at the 20th of April 2021.

[28] A. Schiller, L. Bergholt, M. Guttormsen, E. Melby, J. Rekstad, and S. Siem. Extraction of level density and γ strength function from primary γ spectra. *Nuclear Instruments and Methods in Physics Research Section A: Accelerators, Spectrometers, Detectors and Associated Equipment*, 447(3):498–511, 2000. ISSN 0168-9002. doi: https://doi.org/10.1016/S0168-9002(99)01187-0. URL https://www.sciencedirect.com/science/article/pii/S0168900299011870.

[29] J. Rekstad, A. Henriquez, F. Ingebretsen, G. Midttun, B. Skaali, R. Øyan, J. Wikne, T. Engeland, T. F. Thorsteinsen, E. Hammaren, and E. Liukkonen. A study of the nuclear structure at high energy and low spin. *Phys. Scr.*, 1983 - 45.

[30] A. C. Larsen, M. Guttormsen, M. Krtička, E. Běták, A. Bürger, A. Görgen, H. T. Nyhus, J. Rekstad, A. Schiller, S. Siem, H. K. Toft, G. M. Tveten, A. V. Voinov, and K. Wikan. Analysis of possible systematic errors in the oslo method. *Phys. Rev. C*, 83:034315, Mar 2011. doi: 10.1103/PhysRevC.83.034315. URL https://link.aps.org/doi/10.1103/PhysRevC.83.034315.

[31] V.W. Ingeberg, S. Siem, and M. Wiedeking et al. First application of the oslo method in inverse kinematics. *Eur. Phys. J.*, J:68, 2020. URL https://doi.org/10.1140/epja/s10050-020-00070-7.

[32] A. Spyrou, S. N. Liddick, A. C. Larsen, M. Guttormsen, K. Cooper, A. C. Dombos, D. J. Morrissey, F. Naqvi, G. Perdikakis, S. J. Quinn, T. Renstrøm, J. A. Rodriguez, A. Simon, C. S. Sumithrarachchi, and R. G. T. Zegers. Novel technique for constraining r-process (n, γ) reaction rates. *Phys. Rev. Lett.*, 113:232502, Dec 2014. doi: 10.1103/PhysRevLett.113.232502. URL https://link.aps.org/doi/10.1103/PhysRevLett.113.232502.

[33] N. Starfelt and H. W. Koch. Differential cross-section measurements of thin-target bremsstrahlung produced by 2.7- to 9.7-mev electrons. *Phys. Rev.*, 102:1598–1612, Jun 1956. doi: 10.1103/PhysRev.102.1598. URL https://link.aps.org/doi/10.1103/PhysRev.102.1598.

[34] R. Koohi-Fayegh, S. Green, N.M.J. Crout, G.C Taylor, and M.C. Scott. Neural network unfolding of photon and neutron spectra using an ne-213 scintillation detector. *Nuclear Instruments and Methods in Physics Research Section A: Accelerators, Spectrometers, Detectors and Associated Equipment*, 329(1):269–276, 1993. ISSN 0168-9002. doi: https://doi.org/10.1016/0168-9002(93)90946-F. URL https://www.sciencedirect.com/science/article/pii/016890029390946F.

[35] M Guttormsen, T.S Tveter, L Bergholt, F Ingebretsen, and J Rekstad. The unfolding of continuum -ray spectra. *Nuclear Instruments and Methods in Physics Research Section A: Accelerators, Spectrometers, Detectors and Associated Equipment*, 374(3):371–376, 1996. ISSN 0168-9002. doi: https://doi.org/10.1016/0168-9002(96)00197-0. URL https://www.sciencedirect.com/science/article/pii/0168900296001970.

[36] A. Gilbert and A. G. W. Cameron. A composite nuclear-level density formula with shell corrections. *Can. J. Phys.*, 43:1446–1496, 1965. doi: 10.1139/p65-139.

[37] Till von Egidy and Dorel Bucurescu. Erratum: Systematics of nuclear level density parameters [phys. rev. c 72, 044311 (2005)]. *Phys. Rev. C*, 73:049901, Apr 2006. doi: 10.1103/PhysRevC.73.049901. URL https://link.aps.org/doi/10.1103/PhysRevC.73.049901.

[38] A. Voinov, M. Guttormsen, E. Melby, J. Rekstad, A. Schiller, and S. Siem. γ-ray strength function and pygmy resonance in rare earth nuclei. *Phys. Rev. C*, 63:044313, Mar 2001. doi: 10.1103/PhysRevC.63.044313. URL https://link.aps.org/doi/10.1103/PhysRevC.63.044313.

[39] Magne Guttormsen, Fabio Zeiser, Jørgen Eriksson Midtbø, Vetle W. Ingeberg, and Ann-Cecilie Larsen. oslocyclotronlab/oslo-method-software: Oslo Method v1.1.2, August 2018. URL https://doi.org/10.5281/zenodo.2318646.

[40] Jørgen E. Midtbø, Fabio Zeiser, Erlend Lima, Ann-Cecilie Larsen, Gry M. Tveten, Magne Guttormsen, Frank Leonel Bello Garrote, Anders Kvellestad, and Therese Renstrøm. A new software implementation of the oslo method with rigorous statistical uncertainty propagation. *Computer Physics Communications*, 262:107795, 2021. ISSN 0010-4655. doi: https://doi.org/10.1016/j.cpc.2020.107795. URL https://www.sciencedirect.com/science/article/pii/S001046552030401X.

[41] S. F. Mughabghab. Atlas of neutron resonances (6th edition). 2018. doi: https://doi.org/10.1016/B978-0-44-463780-2.00015-3. URL https://www.sciencedirect.com/science/article/pii/B9780444637802000153.

[42] M. Guttormsen, S. Goriely, A. C. Larsen, A. Görgen, T. W. Hagen, T. Renstrøm, S. Siem, N. U. H. Syed, G. Tagliente, H. K. Toft, H. Utsunomiya, A. V. Voinov, and K. Wikan. Quasicontinuum γ decay of ^{91,92}**Zr**: Benchmarking indirect (n,γ) cross section measurements for the *s* process. *Phys. Rev. C*, 96:024313, Aug 2017. doi: 10.1103/PhysRevC.96.024313. URL https://link.aps.org/doi/10.1103/PhysRevC.96.024313.

[43] I. K. B. Kullmann, A. C. Larsen, T. Renstrøm, K. S. Beckmann, F. L. Bello Garrote, L. Crespo Campo, A. Görgen, M. Guttormsen, J. E. Midtbø, E. Sahin, S. Siem, G. M. Tveten, and F. Zeiser. First experimental constraint on the ^{191}Os(n,γ) reaction rate relevant to *s*-process nucleosynthesis. *Phys. Rev. C*, 99:065806, Jun 2019. doi: 10.1103/PhysRevC.99.065806. URL https://link.aps.org/doi/10.1103/PhysRevC.99.065806.

[44] S.F. Mughabghab. Atlas of neutron resonances (5th edition). 2006. URL https://www.elsevier.com/books/atlas-of-neutron-resonances/mughabghab/978-0-444-52035-7. Isbn: 9780080461069.

[45] R. Capote, M. Herman, P. Obložinský, P.G. Young, S. Goriely, T. Belgya, A.V. Ignatyuk, A.J. Koning, S. Hilaire, V.A. Plujko, M. Avrigeanu, O. Bersillon, M.B. Chadwick, T. Fukahori, Zhigang Ge, Yinlu Han, S. Kailas, J. Kopecky, V.M. Maslov, G. Reffo, M. Sin, E.Sh. Soukhovitskii, and P. Talou. Ripl – reference input parameter library for calculation of nuclear reactions and nuclear data evaluations. *Nuclear Data Sheets*, 110(12): 3107–3214, 2009. ISSN 0090-3752. doi: https://doi.org/10.1016/j.nds.2009.10.004. URL https://www.sciencedirect.com/science/article/pii/S0090375209000994. Special Issue on Nuclear Reaction Data.

[46] T. Shizuma, H. Utsunomiya, P. Mohr, T. Hayakawa, S. Goko, A. Makinaga, H. Akimune, T. Yamagata, M. Ohta, H. Ohgaki, Y.-W. Lui, H. Toyokawa, A. Uritani, and S. Goriely. Photodisintegration cross section measurements on ^{186}W, ^{187}Re, and ^{188}Os: Implications for the re-os cosmochronology. *Phys. Rev. C*, 72:025808, Aug 2005. doi: 10.1103/PhysRevC.72.025808. URL https://link.aps.org/doi/10.1103/PhysRevC.72.025808.

[47] International Atomic Energy Agency Nuclear Data Services. Photon strength function database. https://www-nds.iaea.org/PSFdatabase/, 2018-2019. Dataset: "ARC/DRC measurements for 88 nuclei with Z=9-94". Data downloaded December of 2020.

[48] J. Kopecky and M. Uhl. Test of gamma-ray strength functions in nuclear reaction model calculations. *Phys. Rev. C*, 41:1941–1955, May 1990. doi: 10.1103/PhysRevC.41.1941. URL https://link.aps.org/doi/10.1103/PhysRevC.41.1941.

[49] Matt Newville, Renee Otten, Andrew Nelson, Antonino Ingargiola, Till Stensitzki, Dan Allan, Austin Fox, Faustin Carter, Michał, Dima Pustakhod, lneuhaus, Sebastian Weigand, Ray Osborn, Glenn, Christoph Deil, Mark, Allan L. R. Hansen, Gustavo Pasquevich, Leon Foks, Nicholas Zobrist, Oliver Frost, Alexandre Beelen, Stuermer, kwertyops, Anthony Polloreno, Shane Caldwell, Anthony Almarza, Arun Persaud, Ben Gamari, and Benjamin F. Maier. lmfit/lmfit-py 1.0.2. February 2021. doi: 10.5281/zenodo.4516651. URL https://doi.org/10.5281/zenodo.4516651.